

New York Science Journal

纽约科学杂志

ISSN 1554-0200

Volume 2 - Number 3 (Cumulated No. 7), March 1, 2009



Marsland Press

Brooklyn, New York, the United States

<http://www.sciencepub.net>

sciencepub@gmail.com

New York Science Journal

纽约科学杂志

ISSN 1554-0200

New York Science Journal is published bi-linguistically with Chinese and English for the scientists and Engineers. The journal aims to present experimental and theoretical findings of science and engineering and to report on advances in technologies of multidisciplinary subjects. The journal was founded in 2008 by Marsland Press. The Editor-in-Chief, Deputy Editor and editors have backgrounds in Philosophy, Science, Technology and Engineering, etc. This interdisciplinary team is ultimately suited for facilitating the publication of the best of your research work. The journal welcomes manuscripts from all fields in science and engineering research. Papers submitted could be reviews, objective descriptions, research reports, opinions/debates, news, letters, and other types of writings that are nature and science related. Manuscripts submitted will be peer reviewed and the valuable papers will be considered for the publication after the peer review. Authors are responsible to the contents of their articles.

Editor-in-Chief:Ma Hongbao, Brooklyn, New York, USA, editor@sciencepub.net**Associate Editors-in-Chief:**Cherng Shen, Niaocong, Taiwan, China, cherngs@csu.edu.twJingjing Z Edmondson, Hangzhou, Zhejiang, China, jjze@zju.edu.cnMark Hansen, Lansing, Michigan, USA, mark20082009@gmail.com**Editors:**Ajimotokan HA, Ilorin, Nigeria, hajims@unilorin.edu.ngAvinash Mundhra, Kolkata, India, mundhra.avi@gmail.comCasmir IC, Ekpoma, Edo State, Nigeria, elyonlab@yahoo.comDjamel Boubetra, Berlin, Germany, boubetra@gmail.comGeeta Kharkwal, Uttaranchal, India, geetakh@gmail.comGeorge Chen, East Lansing, Michigan, USA, chengu@msu.eduHamza HD, Zaria, Nigeria, Usmandhamza@yahoo.comJenny Young, New York, USA, jennyyoung123@gmail.comKlarizze Anne M. Puzon, Toulouse, France, klarizze@gmail.com, kmpuzon@gmail.comMargaret Ma, Boston, Massachusetts, USA, margaretgreat@gmail.comMark Lindley, Boston, Massachusetts, USA, mirabene@yahoo.comMary Smith, Washington DC, USA, smithsmith1234567@gmail.comMike Ma, Lansing, Michigan, USA, mikemausa@yahoo.comMohammad Shafie, Kuala Terengganu, Malaysia, msshafie@yahoo.com.myOnyema IC, Lagos, Akoka, Nigeria, iconyema@gmail.comOuyang Da, Okemos, Michigan, USA, ouyangda@msu.eduTracy X Qiao, Ann Arbor, Michigan, USA, xiaotan@umich.eduUsman MA, Ago-Iwoye, Nigeria, usmanma@yahoo.comWillie J McDonald, Houston, Texas, USA, Williemcdonald2007@yahoo.comZhang Meimei, Beijing, China, meimei20082008@gmail.comZhu Yi, Shanghai, China, zhuyi@msu.edu**Web Design:**Jenny Young, New York, jennyyoung123@gmail.com

Information for Authors**Manuscripts Submission**

- (1) **Submission Methods:** Electronic submission through email, on line submission and regular mail with formatted computer diskette would be accepted.
- (2) **Software:** The Microsoft Word file is preferred.
- (3) **Font:** Normal, Times New Roman, 10 pt, single space.
- (4) **Indent:** Type 4 spaces in the beginning of each new paragraph.
- (5) **Manuscript:** Don't use "Footnote" or "Header and Footer".
- (6) **Cover Page:** Put detail information of authors and a short running title in the cover page.
- (7) **Title:** Use Title Case in the title and subtitles, e.g. "**Debt and Agency Costs**".
- (8) **Figures and Tables:** Use full word of figure and table, e.g. "**Figure 1. Annual Income of Different Groups**", "**Table 1. List Data**".
- (9) **References:** Cite references by "last name, year", e.g. "(Smith, 2003)". References should include all the authors' last names and initials, title, journal, year, volume, issue, and pages etc. **Reference Examples: Journal Article:** Hacker J, Hentschel U, Dobrindt U. Prokaryotic chromosomes and disease. *Science* 2003;301(34):790-3; **Book:** Berkowitz BA, Katzung BG. Basic and clinical evaluation of new drugs. In: Katzung BG, ed. *Basic and clinical pharmacology*. Appleton & Lance Publisher. Norwalk, Connecticut, USA. 1995:60-9.
- (10) **Submission Address:** Marsland Press, 525 Rockaway PKWY, #B44, Brooklyn, New York 11212, USA; Telephone: (347) 321-7172; Emails: sciencepub@gmail.com; editor@sciencepub.net.
- (11) **Reviewers:** Authors should suggest 2-8 competent reviewers with their name and email.

2. Manuscript Preparation

Each manuscript should be formatted to include the following components:

- (1) **Title page:** including the complete article title; each author's full name; institution(s) with which each author is affiliated, with city, state/province, zip code, and country; and the name, complete mailing address, telephone number, facsimile number (if available), and e-mail address for all correspondence.
- (2) **Abstract:** including Background, Materials and Methods, Results, and Discussions.
- (3) **Key Words.**
- (4) **Introduction.**
- (5) **Materials and Methods.**
- (6) **Results.**
- (7) **Discussions.**
- (8) **References.**
- (9) **Acknowledgments.**

Journal Address:

Marsland Press
525 Rockaway PKWY, #B44
Brooklyn, New York 11212
The United States
Telephone: (347) 321-7172
E-mail: editor@sciencepub.net; sciencepub@gmail.com;
Websites: <http://www.sciencepub.net>

New York Science Journal

纽约科学杂志

Volume 2 - Number 3 (Cumulated No. 7), March 1, 2009; ISSN 1554-0200

[Cover Page](#), [Introduction](#), [Contents](#), [Call for Papers](#), [All papers in one file](#)

CONTENTS

No. / Titles / Authors

	page
1. Best-fit Probability distribution model for peak daily rainfall of selected Cities in Nigeria Olofintoye, O.O, Sule, B.F and Salami, A.W	1-12
2. Electrical Resistivity Method in Engineering and Environmental Studies: A Case Study of Gbagada Area, Lagos State, Nigeria Oyedele, K.F and Ojo, A.O	13-20
3. Total Dissolved Solids (TDS) Mapping In Groundwater Using Geophysical Method Oyedele, K. F.	21-31
4. Evaluation of Sea water Intrusion in Freshwater Aquifers in a Lagoon Coast: A Case Study of the University of Lagos Lagoon, Akoka, Nigeria K.F.Oyedele, E.I. Momoh	32-42
5. Model for Predicting the Initial Solution pH at Assumed Final pH and Leaching Time during Leaching of Iron Oxide Ore in Hydrogen Peroxide Solution Chukwuka Ikechukwu Nwoye, Paulinus Chukwudi Agu, Okechukwu Daniel Onukwuli, Joshua Oke Borode, Christian Nwosu Mbah	43-48
6. Model for Calculating the Concentration of Leached Iron Relative to the Final Solution Temperature during Sulphuric Acid Leaching of Iron Oxide Ore Chukwuka Ikechukwu Nwoye, Gideon Chima Obasi, Udochukwu Mark, Stanley Inyama, Chinedu Chris Nwakwuo	49-54
7. Model for Quantifying the Extent and Magnitude of Water Evaporated during Time Dependent Drying of Clay Chukwuka Ikechukwu Nwoye, Chinedu Chris Nwakwuo, Martins Chidi Obi, Gideon Chima Obasi, Okechukwu Onyebuchi Onyemaobi	55-58
8. Scale Analysis of Fluid Flow and Forced Convective Heat Transfer in the Entrance Region of Elliptic Conduits I. K. Adegun and O. A. Oladosu	59-71

[9. Enhancement Of Thermal Capabilities Of A Solar Concentrator](#)

I. O. Ohijeagbon¹, A. S. Adekunle², and O.D. Awolaran

72-78

[10. Our Universe Was Originated From The Big Bang Caused By The Amalgamations of a Great Amount of the Original Minimum Schwarzcuild Black Holes, But Not From Singularity or Not From The Big Bang of Singularity](#)

[对宇宙起源的新观念和新的完整论证:宇宙不可能诞生于奇点](#)

Dongsheng Zhang

79-100

Marsland Press, 525 Rockaway PKWY, Brooklyn, New York 11212, The United States; (347) 321-7172; editor@sciencepub.net

<http://www.sciencepub.net>

editor@sciencepub.net

For back issues of the New York Science Journal, [click here](#).

Emails: editor@sciencepub.net; sciencepub@gmail.com

Website: <http://www.sciencepub.net/newyork>

Best-fit Probability distribution model for peak daily rainfall of selected Cities in Nigeria

Olofintoye, O.O, Sule, B.F and Salami, A.W
Department of Civil Engineering, University of Ilorin, P.M.B 1515, Ilorin, Nigeria
geotoseen@yahoo.co.uk

Abstract

This study aims at studying the peak daily rainfall distribution characteristics in Nigeria, by using different statistical analyses such as Gumbel, Log-Gumbel, Normal, Log-Normal, Pearson and Log-Pearson distributions. 20 stations having annual rainfall data of fifty-four (54) years were selected to perform frequency analysis. Mathematical equation for the probability distribution functions were established for each station and used to predict peak rainfall, the predicted values were subjected to goodness of fit tests such as chi-square, Fisher's test, correlation coefficient and coefficient of determination to determine how best the fits are. The model that satisfies the tests adequately was selected as the best fit model. Results showed that the log-Pearson type III distribution performed the best by occupying 50% of the total station number, while Pearson type III performed second best by occupying 40% of the total stations and lastly by log-Gumbel occupying 10% of the total stations. [New York Science Journal. 2009;2(3):1-12]. (ISSN: 1554-0200).

Key words: Rainfall, peak rainfall, probability distribution models and goodness of fit tests

Introduction

The design and construction of certain projects, such as dams and urban drainage systems, the management of water resources, and the prevention of flood damage require an adequate knowledge of extreme events of high return periods (Tao et al, 2002). In most cases, the return periods of interest exceed usually the periods of available records and could not be extracted directly from the recorded data. Therefore, in current engineering practice, the estimation of extreme rainfalls is accomplished based on statistical frequency analysis of maximum precipitation records where available sample data could be used to calculate the parameters of a selected frequency distribution. The fitted distribution is then used to estimate event magnitudes corresponding to return periods greater than or less than those of the recorded events, hence accurate estimation of extreme rainfall could help to alleviate the damage caused by storms and can help to achieve more efficient design of hydraulic structures.

Tao et al (2002) reported that several probability models have been developed to describe the distribution of annual extreme rainfalls at a single site. However, the choice of a suitable model is still one of the major problems in engineering practice since there is no general agreement as to which distribution, or distributions, that should be used for the frequency analysis of extreme rainfalls. The selection of an appropriate model depends mainly on the characteristics of available rainfall data at the particular site. Hence, it is necessary to evaluate many available distributions in order to find a suitable model that could provide accurate extreme rainfall estimates. This study aimed to determine the best fit probability distribution for the prediction of peak daily rainfall data in selected cities in Nigeria.

Literature review

Phien and Ajirajah (1984) evaluated the applicability of the LP3 distribution to flood and maximum rainfall data, and its general use in fitting annual rainfall and stream flow sequences. The evaluation was carried out by selecting four types of data, which consist of annual flood, annual maximum rainfall of different durations, annual stream flow, and annual rainfall. Three methods of parameter estimation were used, these include; method of maximum likelihood (MML), method using the first two moments of x and first moment of y (MM1) and method using the first two moments of x and second moment of y (MM2). It was pointed out that the estimates of a parameter obtained from the methods MM1 and MM2 are relatively close to each other, while that obtained by maximum likelihood (MML) shows a larger difference. The applicability of the LP3 distribution to the four data types evaluated by the Chi-square (χ^2) and Kolmogorov – Smirnov (Δ) tests was said to be highly suitable. Chapman (1994) tested 5 daily rainfall generating models with several methods of evaluating the model parameters, and reported that the Srikanthan-McMahon (TPM) model performed particularly well when calibrated with long rainfall records.

Boughton (1999) reported that daily rainfall records form a major hydrological data base in Australia, but the common 50 – 100 years of available record at a station do not give adequate information about long term risks of droughts or floods. Transaction probability matrix (TPM) models have been used in prior studies to generate long

sequences of daily rainfalls, but the model most commonly used in Australia seriously under estimates the variance of annual totals of rainfall. There has been a steadily increasing interest in the stochastic generation of long sequences of daily rainfalls for periods ranging from 100 to 1,000,000 years in order to give a better definition of extreme droughts and floods. Ogunlela (2001) studied the stochastic analysis of rainfall event in Ilorin using probability distribution functions. He concluded that the log-Pearson type III distribution best described the peak daily rainfall data for Ilorin.

Tao et al (2002) proposes a systematic assessment procedure to compare the performance of different probability distributions in order to identify an appropriate model that could provide the most accurate extreme rainfall estimates at a particular site. Nine probability models such as Beta-K (BEK), Beta-P (BEP), Generalized Extreme Value (GEV), Generalized Normal (GNO), Generalized Pareto (GPA), Gumbel (GUM), Log-Pearson Type III (LP3), Pearson Type III (PE3), and Wakeby (WAK) distributions were compared for their descriptive and predictive abilities to represent the distribution of annual maximum rainfalls. The suggested methodology was applied to 5-minute and 1-hour annual maximum rainfall series from a network of 20 raingages in Southern Quebec region. On the basis of graphical and numerical comparisons, it was found that the WAK, GNO, and GEV models could provide the most accurate extreme rainfall estimates. However, the GEV was recommended as the most suitable distribution due to its theoretical basis for representing extreme – value process and its relatively simple parameter estimation.

Topaloglu (2002) reported that the frequency analysis of the largest, or the smallest, of a sequence of hydrologic events has long been an essential part of the design of hydraulic structures. Therefore, the question of better fit among countless probability models used in frequency analysis is always a fresh one. In his study, he made a statistical comparison of currently popular probability models such as Gumbel, log-logistic, Pearson-3, log-Pearson-3 and log-Normal-3 distributions were applied to the series of annual instantaneous flood peaks and annual peak daily precipitation for 13 flow gauging and 55 precipitation gauging stations in the Seyhan basin, respectively. The parameters of the distributions were estimated by the methods of moments (MOM) and probability weighted moments (PWM). A detailed Chi-square and Kolmogorov-Smirnov (k-s) goodness -of-fit tests were also applied. According to the evaluations of Chi-squared tests, Gumbel (MOM) for both flow and precipitation stations in the Seyhan river basin were found to be the best models. As a result of the k-s test, log-Normal-3 (MOM) and log-Pearson-3 (MOM) models were determined to be the best for flow and precipitation stations, respectively.

Guevara (2003) carried out hydrologic analysis to estimate engineering design parameters of storms in Venezuela, which help hydrologists to improve their environmental designs. The analysis focused on storm advancement coefficient r (SAC) to establish storm Pluviographs; intensity Duration Frequency (IDF) ; and Area – Depth – Duration relationships (ADD). Based on the analysis of 275 storm events, values of r were calculated obtaining a mean value of 0.41 and a standard deviation of 0.075, and being 61, 30, and 9 % storms from the advanced, retarded and symmetric type respectively.

Salami (2004) indicated that Gary and Robert in 1971 studied the normal, log-normal, square-root-normal and cube-root-normal frequency distributions of meteorological data for Texas. The results of this research shows that precipitation data conform to the square-root-normal distribution, while evaporation and temperature data conform to all of the frequency distributions tested. The evaporation, temperature and precipitation data were further fitted to the Gumbel extreme-value and log-Pearson type III distributions. The precipitation data fit the log-Pearson type III (LP3) distribution more adequately than the Gumbel distribution, while both the evaporation and temperature data conform very well to Gumbel distribution.

Lee (2005) studies the rainfall distribution characteristics of Chia-Nan plain area, by using different statistical analyses such as normal distribution, log-normal distribution, extreme value type I distribution, Pearson type III distribution, and log-Pearson type III distribution. Results showed that the log-Pearson type III distribution performed the best in probability distribution, occupying 50% of the total station number, followed by the log-Normal distribution and Pearson type III distribution, which accounts for 19% and 18% of the total station numbers respectively.

Bhakar et al (2006) studied the frequency analysis of consecutive day's maximum rainfall at Banswara, Rajasthan, India. Various probability distributions and transformations were applied to estimate one day and two to five consecutive days annual maximum rainfall of various return periods. Three commonly used probability distributions, Normal, Log Normal and Gamma distribution were tested by comparing the Chi-square value. Gamma distribution was found to be best fit for the region. The magnitudes of 1 day as well as 2 to 5 consecutive days annual maximum rainfall corresponding to 2 to 100 years return period were estimated using Gamma function. A maximum of 154.31 mm in 1 day, 250.88 mm in 2 days, 270.15 mm in 3 days, 284.18 mm in 4 days and 295.54 mm in 5 days is expected to occur at Udaipur, Rajasthan every 2 years. For a recurrence interval of 100 years, the

maximum rainfall expected in 1 day, 2, 3, 4 and 5 days is 773.6 mm, 849.34 mm, 874.19 mm, 931.78 mm and 957.89 mm, respectively. Annual one day maximum rainfall and two to five days consecutive days maximum rainfall corresponding to return period varying from 2 to 100 years are used by design engineers and hydrologists for the economic planning, design of small and medium hydrologic structures and determination of drainage coefficient for agricultural fields.

Data and Analysis

The daily rainfall data for the selected cities were obtained from the Nigerian Meteorological Agency (NIMET), Oshodi Lagos, Nigeria. NIMET is the agency responsible for the measurement, control, and storage of rainfall data of the areas in Nigeria. The nature of data is rainfall depth (mm) recorded for everyday of the year. The rainfall data spanned between 1952 and 2005 and the peak daily values were extracted for the purpose of analysis. Twenty cities were selected for this study and include Bauchi, Gusau, Ilorin, Jos, Kaduna, Kano, Maiduguri, Makurdi, Minna, Potiskum, Sokoto, Yola, Benin City, Calabar, Enugu, Ibadan, Ikeja, Ondo, Owerri, and P. Harcourt. The summary of statistics for peak daily rainfall is presented in table 1.

The data are ranked according to Welbull's plotting position and the corresponding return period was estimated. The ranked data were evaluated with six methods of probability distribution functions to determine the best – fit functions. The methods include; Gumbel (EVI type1), Log-Gumbel (LG), Normal (N), Log-Normal (LN), Log-Pearson type III (LP₃) and Pearson type III (P) probability distribution models. Four statistical goodness of fit test were used for the selection of the best fit models.

Table 1 Summary of statistics for peak daily rainfall (1952 – 2005)

Selected Cities	Parameters					Maximum (mm)	Minimum (mm)
	Mean value, \bar{x} (mm)	Standard deviation, σ (mm)	Skewness coefficient (G)	Coefficient of variation (Cv)			
Bauchi	73.42	11.71	1.43	0.16	108.60	61.70	
Gusau	74.56	15.79	1.74	0.21	136.30	57.60	
Ilorin	91.10	19.08	1.44	0.21	160.50	70.90	
Jos	72.12	11.28	1.50	0.16	107.19	60.71	
Kaduna	76.81	15.65	1.47	0.20	132.10	59.60	
Kano	91.49	30.94	3.46	0.34	253.10	70.70	
Maiduguri	74.46	17.91	1.30	0.24	128.00	56.40	
Makurdi	101.97	24.68	2.32	0.24	206.25	80.70	
Minna	88.92	18.12	1.15	0.20	144.00	69.30	
Potiskum	73.35	16.35	1.85	0.22	129.30	57.80	
Sokoto	72.87	16.00	1.96	0.22	139.40	56.10	
Yola	78.17	16.16	1.45	0.21	126.24	61.72	
Benin City	118.15	20.91	1.21	0.18	181.40	96.00	
Calabar	139.65	24.74	1.14	0.18	216.00	112.20	
Enugu	106.93	21.18	1.41	0.20	174.40	83.80	
Ibadan	117.16	28.95	1.32	0.25	225.90	86.90	
Ikeja	121.73	27.93	1.91	0.23	237.30	95.50	
Ondo	100.24	29.93	2.73	0.30	246.30	73.90	
Owerri	113.12	22.35	1.61	0.20	181.90	90.50	
P. Harcourt	111.01	23.64	1.71	0.21	185.30	88.40	

Probability distribution analysis was carried out in accordance with standard procedure [Warren et al, (1972); Viessman et al, (1989); Mustapha and Yusuf, (1999), and Topaloglu (2002)]. The mathematical expressions obtained for various probability distributions functions are presented in Table 2. The mathematical expressions obtained for each function were used to predict the peak rainfall data based on the estimated returned periods and were also used in performing the statistical tests (goodness of fit tests) for the selection of the best fit models.

Table 2 Mathematical expression for probability distributions models

Station	Distributions					
	Normal	Log-Normal	Pearson III	Log-Pearson III	Gumbel	Log-Gumbel
Bauchi	$R_p = 73.42 + 11.71K$	$\text{Log } R_p = 1.86 + 0.06K$	$R_p = 73.42 + 11.71K'$	$\text{Log } R_p = 1.86 + 0.06K'$	$R_p = 68.16 + 9.13Y_T$	$\text{Log } R_p = 1.83 + 0.05Y_T$
Gusau	$R_p = 74.56 + 15.79K$	$\text{Log } R_p = 1.86 + 0.08K$	$R_p = 74.56 + 15.79K'$	$\text{Log } R_p = 1.86 + 0.08K'$	$R_p = 67.46 + 12.31Y_T$	$\text{Log } R_p = 1.83 + 0.06Y_T$
Ilorin	$R_p = 91.10 + 19.08K$	$\text{Log } R_p = 1.95 + 0.08K$	$R_p = 91.10 + 19.08K'$	$\text{Log } R_p = 1.95 + 0.08K'$	$R_p = 82.51 + 14.88Y_T$	$\text{Log } R_p = 1.91 + 0.06Y_T$
Jos	$R_p = 72.12 + 11.28K$	$\text{Log } R_p = 1.85 + 0.06K$	$R_p = 72.12 + 11.28K'$	$\text{Log } R_p = 1.85 + 0.06K'$	$R_p = 67.04 + 8.80Y_T$	$\text{Log } R_p = 1.83 + 0.05Y_T$
Kaduna	$R_p = 76.81 + 15.65K$	$\text{Log } R_p = 1.88 + 0.08K$	$R_p = 76.81 + 15.65K'$	$\text{Log } R_p = 1.88 + 0.08K'$	$R_p = 69.76 + 12.21Y_T$	$\text{Log } R_p = 1.84 + 0.06Y_T$
Kano	$R_p = 91.49 + 30.94K$	$\text{Log } R_p = 1.95 + 0.11K$	$R_p = 91.49 + 30.94K'$	$\text{Log } R_p = 1.95 + 0.11K'$	$R_p = 77.56 + 24.13Y_T$	$\text{Log } R_p = 1.90 + 0.08Y_T$
Maiduguri	$R_p = 74.46 + 17.91K$	$\text{Log } R_p = 1.86 + 0.10K$	$R_p = 74.46 + 17.91K'$	$\text{Log } R_p = 1.86 + 0.10K'$	$R_p = 66.40 + 13.97Y_T$	$\text{Log } R_p = 1.82 + 0.07Y_T$
Makurdi	$R_p = 101.97 + 24.68K$	$\text{Log } R_p = 2.00 + 0.09K$	$R_p = 101.97 + 24.68K'$	$\text{Log } R_p = 2.00 + 0.09K'$	$R_p = 90.86 + 19.25Y_T$	$\text{Log } R_p = 1.96 + 0.07Y_T$
Minna	$R_p = 88.92 + 18.12K$	$\text{Log } R_p = 1.94 + 0.08K$	$R_p = 88.92 + 18.12K'$	$\text{Log } R_p = 1.94 + 0.08K'$	$R_p = 80.77 + 14.13Y_T$	$\text{Log } R_p = 1.90 + 0.06Y_T$
Potiskum	$R_p = 78.17 + 16.16K$	$\text{Log } R_p = 1.89 + 0.08K$	$R_p = 78.17 + 16.16K'$	$\text{Log } R_p = 1.89 + 0.08K'$	$R_p = 70.90 + 12.61Y_T$	$\text{Log } R_p = 1.85 + 0.06Y_T$
Sokoto	$R_p = 72.87 + 16.00K$	$\text{Log } R_p = 1.85 + 0.08K$	$R_p = 72.87 + 16.00K'$	$\text{Log } R_p = 1.85 + 0.08K'$	$R_p = 65.67 + 12.48Y_T$	$\text{Log } R_p = 1.82 + 0.07Y_T$
Yola	$R_p = 78.17 + 16.16K$	$\text{Log } R_p = 1.89 + 0.08K$	$R_p = 78.17 + 16.16K'$	$\text{Log } R_p = 1.89 + 0.08K'$	$R_p = 70.90 + 12.61Y_T$	$\text{Log } R_p = 1.85 + 0.06Y_T$
Benin-City	$R_p = 118.15 + 20.91K$	$\text{Log } R_p = 2.07 + 0.07K$	$R_p = 118.15 + 20.91K'$	$\text{Log } R_p = 2.07 + 0.07K'$	$R_p = 108.74 + 16.31Y_T$	$\text{Log } R_p = 2.03 + 0.06Y_T$
Calabar	$R_p = 139.65 + 24.72K$	$\text{Log } R_p = 2.14 + 0.07K$	$R_p = 139.65 + 24.72K'$	$\text{Log } R_p = 2.14 + 0.07K'$	$R_p = 128.52 + 19.29Y_T$	$\text{Log } R_p = 2.11 + 0.06Y_T$
Enugu	$R_p = 106.93 + 21.18K$	$\text{Log } R_p = 2.02 + 0.08K$	$R_p = 106.93 + 21.18K'$	$\text{Log } R_p = 2.02 + 0.08K'$	$R_p = 97.40 + 16.52Y_T$	$\text{Log } R_p = 1.99 + 0.06Y_T$
Ibadan	$R_p = 117.16 + 28.95K$	$\text{Log } R_p = 2.06 + 0.10K$	$R_p = 117.16 + 28.95K'$	$\text{Log } R_p = 2.06 + 0.10K'$	$R_p = 104.13 + 22.58Y_T$	$\text{Log } R_p = 2.01 + 0.08Y_T$
Ikeja	$R_p = 121.73 + 27.93K$	$\text{Log } R_p = 2.08 + 0.09K$	$R_p = 121.73 + 27.93K'$	$\text{Log } R_p = 2.08 + 0.09K'$	$R_p = 109.17 + 21.78Y_T$	$\text{Log } R_p = 2.04 + 0.07Y_T$
Ondo	$R_p = 100.24 + 29.93K$	$\text{Log } R_p = 1.99 + 0.10K$	$R_p = 100.24 + 29.93K'$	$\text{Log } R_p = 1.99 + 0.10K'$	$R_p = 86.78 + 23.35Y_T$	$\text{Log } R_p = 1.94 + 0.08Y_T$
Owerri	$R_p = 113.12 + 22.35K$	$\text{Log } R_p = 2.05 + 0.08K$	$R_p = 113.12 + 22.35K'$	$\text{Log } R_p = 2.05 + 0.08K'$	$R_p = 103.06 + 17.43Y_T$	$\text{Log } R_p = 2.01 + 0.06Y_T$
PortHarcourt	$R_p = 111.01 + 23.64K$	$\text{Log } R_p = 2.04 + 0.08K$	$R_p = 111.01 + 23.64K'$	$\text{Log } R_p = 2.04 + 0.08K'$	$R_p = 100.37 + 18.44Y_T$	$\text{Log } R_p = 2.00 + 0.06Y_T$

In order to determine the best-fit model(s) at each station, probability distribution models were subjected to four (4) statistical tests (goodness of fit tests). The statistical tests include chi-square (χ^2), Fisher's (F) test, probability plot coefficient of correlation (r) and coefficient of determination (R^2). The statistical tests were carried out in accordance with standard procedure (Chowdhury and Stedinger (1991); Adegboye and Ipinoyomi (1995); Dibike and Solomatine (1999); Murray and Larry (2000)). The assessment of the probability distribution models was based on the total test score obtained from all the tests. Test scores ranging from zero to six (0-6) is awarded to each distribution model based on the criteria that the distribution (s) with the highest total score is or are chosen as the best distribution model(s) for the data of a particular city. In general, the distribution best supported by a test is awarded a score of six (6), the next best is awarded five (5), and so on in descending order. A distribution is awarded a zero (0) score for a test if the test indicates that there is a significant difference between the rainfall values estimated by the distribution model and the observed rainfall data. For every test category, overall ranks of each distribution were obtained by summing the individual point rank at each of the 20 stations. The overall ranking results are presented in Table 3 while the best fit probability distribution models are presented in Table 4.

Table 3 Summary of the statistical test score results at each station

Stations	Best fit distribution model	Chi-square test	Fisher's test	PPCC (r)	R^2	Total
Bauchi	Normal	1	1	1	1	4
	Log-Normal	2	2	2	2	8
	Pearson	5	6	5	5	21
	Log-Pearson	6	5	6	6	23
	Gumbel (EVI)	3	3	3	3	12
	Log-Gumbel	4	4	4	4	16
Gusau	Normal	1	1	1	1	4
	Log-Normal	2	2	2	2	8
	Pearson	6	6	4	6	22
	Log-Pearson	5	5	5	5	20
	Gumbel (EVI)	3	3	3	3	12
	Log-Gumbel	4	4	6	4	18
Ilorin	Normal	1	1	1	1	4
	Log-Normal	2	2	2	2	8
	Pearson	6	6	4	5	21
	Log-Pearson	5	5	5	6	21
	Gumbel (EVI)	3	3	3	3	12
	Log-Gumbel	4	4	6	4	18
Jos	Normal	1	1	1	1	4
	Log-Normal	2	2	2	2	8
	Pearson	5	6	5	5	21
	Log-Pearson	6	5	6	6	23
	Gumbel (EVI)	3	3	3	3	12
	Log-Gumbel	4	4	4	4	16
Kaduna	Normal	1	1	1	1	4
	Log-Normal	2	2	2	2	8
	Pearson	5	5	4	4	18
	Log-Pearson	4	4	5	5	18
	Gumbel (EVI)	3	3	3	3	12
	Log-Gumbel	6	6	6	6	24
Kano	Normal	0	2	1	1	4
	Log-Normal	0	1	2	2	5
	Pearson	6	6	5	6	23
	Log-Pearson	5	5	6	5	21
	Gumbel (EVI)	0	4	3	3	10
	Log-Gumbel	0	3	4	4	11
Maiduguri	Normal	1	1	1	1	4
	Log-Normal	2	2	2	2	8
	Pearson	4	6	4	5	19

Log-Pearson	6	5	6	6	23
Gumbel (EVI)	3	3	3	3	12
Log-Gumbel	5	4	5	4	18

Table 3 continue

Stations	Best fit distribution model	Chi-square test	Fisher's test	PPCC (r)	R ²	Total
Makurdi	Normal	0	1	1	1	3
	Log-Normal	2	2	2	2	8
	Pearson	6	6	5	6	23
	Log-Pearson	5	5	6	5	21
	Gumbel (EVI)	3	3	3	3	12
	Log-Gumbel	4	4	4	4	16
Minna	Normal	1	1	1	1	4
	Log-Normal	2	2	2	2	8
	Pearson	4	5	4	4	17
	Log-Pearson	6	6	6	6	24
	Gumbel (EVI)	3	3	3	3	12
	Log-Gumbel	5	4	5	5	19
Potiskum	Normal	1	1	1	1	4
	Log-Normal	2	2	2	2	8
	Pearson	6	6	5	6	23
	Log-Pearson	5	5	6	5	21
	Gumbel (EVI)	3	3	3	3	12
	Log-Gumbel	4	4	4	4	16
Sokoto	Normal	1	1	1	1	4
	Log-Normal	2	2	2	2	8
	Pearson	5	6	4	5	20
	Log-Pearson	6	5	6	6	23
	Gumbel (EVI)	3	3	3	3	12
	Log-Gumbel	4	4	5	4	17
Yola	Normal	1	1	1	1	4
	Log-Normal	2	2	2	2	8
	Pearson	5	6	4	5	20
	Log-Pearson	6	5	6	6	23
	Gumbel (EVI)	3	3	3	3	12
	Log-Gumbel	4	4	5	4	17
Benin City	Normal	1	1	1	1	4
	Log-Normal	2	2	2	2	8
	Pearson	4	5	4	5	18
	Log-Pearson	6	6	6	6	24
	Gumbel (EVI)	3	3	3	3	12
	Log-Gumbel	5	4	5	4	18
Calabar	Normal	1	1	1	1	4
	Log-Normal	2	2	2	2	8
	Pearson	4	5	4	5	18
	Log-Pearson	6	6	6	6	24
	Gumbel (EVI)	3	3	3	3	12
	Log-Gumbel	5	4	5	4	18

Table 3 continue

Stations	Best fit distribution model	Chi-square test	Fisher's test	PPCC (r)	R ²	Total
Enugu	Normal	1	1	1	1	4

Ibadan	Log-Normal	2	2	2	2	8
	Pearson	6	6	4	5	21
	Log-Pearson	5	5	5	6	21
	Gumbel (EVI)	3	3	3	3	12
	Log-Gumbel	4	4	6	4	18
	Normal	1	1	1	1	4
Ikeja	Log-Normal	2	2	2	2	8
	Pearson	6	5	4	5	20
	Log-Pearson	5	4	5	4	18
	Gumbel (EVI)	3	3	3	3	12
	Log-Gumbel	4	6	6	6	22
	Normal	0	1	1	1	3
Ondo	Log-Normal	2	2	2	2	8
	Pearson	6	6	5	6	23
	Log-Pearson	5	5	6	5	21
	Gumbel (EVI)	3	3	3	3	12
	Log-Gumbel	4	4	4	4	16
	Normal	0	2	1	1	4
Owerri	Log-Normal	0	1	2	2	5
	Pearson	5	6	5	6	22
	Log-Pearson	6	5	6	5	22
	Gumbel (EVI)	3	3	3	3	12
	Log-Gumbel	4	4	4	4	16
	Normal	1	1	1	1	4
P. Harcourt	Log-Normal	2	2	2	2	8
	Pearson	6	6	4	6	22
	Log-Pearson	5	5	6	5	21
	Gumbel (EVI)	3	3	3	3	12
	Log-Gumbel	4	4	5	4	17
	Normal	1	1	1	1	4
P. Harcourt	Log-Normal	2	2	2	2	8
	Pearson	6	6	5	6	23
	Log-Pearson	5	5	6	5	21
	Gumbel (EVI)	3	3	3	3	12
	Log-Gumbel	4	4	4	4	16
	Normal	1	1	1	1	4

Table 4 Goodness of fit tests and the selected model for the peak rainfall

	Best-Fit Model	Second Best-Fit Model	Best-Fit Model Equation
Bauchi	Log-Pearson III	Pearson III	$\text{Log } R_p = 1.86 + 0.06K'$
Gusau	Pearson III	Log-Pearson III	$R_p = 74.56 + 15.79K'$
Ilorin	Log-Pearson III	Pearson III	$\text{Log } R_p = 1.95 + 0.08K'$
Jos	Log-Pearson III	Pearson III	$\text{Log } R_p = 1.85 + 0.06K'$
Kaduna	Log-Gumbel	Pearson III	$\text{Log } R_p = 1.84 + 0.06Y_T$
Kano	Pearson III	Log-Pearson III	$R_p = 91.49 + 30.94K'$
Maiduguri	Log-Pearson III	Pearson III	$\text{Log } R_p = 1.86 + 0.10K'$
Makurdi	Pearson III	Log-Pearson III	$R_p = 101.97 + 24.68K'$
Minna	Log-Pearson III	Log-Gumbel	$\text{Log } R_p = 1.94 + 0.08K'$

Potiskum	Pearson III	Log-Pearson III	$R_p = 73.35 + 16.35K'$
Sokoto	Log-Pearson III	Pearson III	$\text{Log } R_p = 1.85 + 0.08K'$
Yola	Log-Pearson III	Pearson III	$\text{Log } R_p = 1.89 + 0.08K'$
Benin-City	Log-Pearson III	Log-Gumbel	$\text{Log } R_p = 2.07 + 0.07K'$
Calabar	Log-Pearson III	Log-Gumbel	$\text{Log } R_p = 2.14 + 0.07K'$
Enugu	Log-Pearson III	Pearson III	$\text{Log } R_p = 2.02 + 0.08K'$
Ibadan	Log-Gumbel	Pearson III	$\text{Log } R_p = 2.01 + 0.08Y_T$
Ikeja	Pearson III	Log-Pearson III	$R_p = 121.73 + 27.93K'$
Ondo	Pearson III	Log-Pearson III	$R_p = 100.24 + 29.93K'$
Owerri	Pearson III	Log-Pearson III	$R_p = 113.12 + 22.35K'$
Port-Harcourt	Pearson III	Log-Pearson III	$R_p = 111.01 + 23.64K'$

Application of results

The results obtained from the analysis may be useful for engineering planning and designs in that future year maximum daily rainfall events can be predicted. However the selected best distribution model were used to predict maximum daily rainfall depths for the twenty stations for return periods of 5, 10, 20, 50, 100, 200, and 500 years. The quantile estimates are presented in table 5.

Table 5 Quantile estimates for various return periods

Station	Best-Fit Model	Reccurence interval in years						
		5	10	20	50	100	200	500
Bauchi	Log-Pearson III	80.90	88.32	95.90	106.41	114.84	123.78	136.46
Gusau	Pearson III	84.74	95.15	105.45	119.07	129.42	139.84	153.74
Ilorin	Log-Pearson III	103.24	115.30	127.68	144.99	159.02	174.00	195.49
Jos	Log-Pearson III	79.19	86.39	93.78	104.08	112.39	121.22	133.81
Kaduna	Log-Gumbel	86.25	96.16	106.74	122.18	135.19	149.54	170.82
Kano	Pearson III	101.03	123.39	149.10	187.17	218.60	252.01	298.92
Maiduguri	Log-Pearson III	85.92	97.27	108.94	125.30	138.61	152.87	173.38
Makurdi	Pearson III	115.27	132.57	150.58	175.37	194.78	214.73	241.86
Minna	Log-Pearson III	101.06	112.34	123.68	139.21	151.56	164.55	182.86
Potiskum	Pearson III	83.59	94.52	105.45	120.01	131.14	142.39	157.45
Sokoto	Log-Pearson III	82.29	92.48	103.22	118.63	131.42	145.35	165.77
Yola	Log-Pearson III	88.26	98.57	109.24	124.29	136.57	149.76	168.81
Benin	Log-Pearson III	132.13	145.13	158.17	175.96	190.05	204.82	225.56
Calabar	Log-Pearson III	156.53	171.74	186.85	207.25	223.27	239.95	263.19
Enugu	Log-Pearson III	120.55	133.88	147.50	166.41	181.66	197.86	220.97
Ibadan	Log-Gumbel	134.31	153.36	174.17	205.36	232.33	262.73	309.01
Ikeja	Pearson III	138.92	157.72	176.62	201.90	221.30	240.94	267.30
Ondo	Pearson III	113.99	135.47	158.62	191.34	217.46	244.64	282.05

Owerri	Pearson III	128.02	142.48	156.63	175.15	189.13	203.12	221.70
PortHarcourt	Pearson III	126.36	141.89	157.24	177.48	192.84	208.30	228.89

Development of Isohyet maps of 100 and 200 year return period

Analysis of rainfall data requires handling of large volumes of data and repeated computation of a number of statistical parameters for distribution fitting and estimation of expected rainfall at different return periods. The use of rainfall frequency atlases may considerably reduce the computational tedium involved in the frequency analysis of rainfall to a greater extent. Maps have been prepared for some regions, particularly East Africa, showing the annual rainfall likely to be equaled or exceeded in 80% of years. These are extremely useful for planning purposes (Edwards et al, 1983). In this study isohyet maps were constructed using software (Surfer 8). Surfer is a contouring and 3D surface mapping program that runs under Microsoft Windows. Surfer version 8 is a product of Golden Software, Inc (www.goldensoftware.com). The quantile estimates for 100 and 200 years return periods presented in table 5 were used to construct isohyetal maps for the maximum daily rainfall for selected cities in Nigeria. The isohyetal map for 100 and 200 years return period are presented in Figure 1 and 2 respectively. With the established maps, the rainfall depth for 100 and 200 years return period for any location (longitude and latitude) in Nigeria may be estimated more easily and faster without having to go through the rigor of fitting probability distribution models all over again. These are very useful for design and planning purposes.

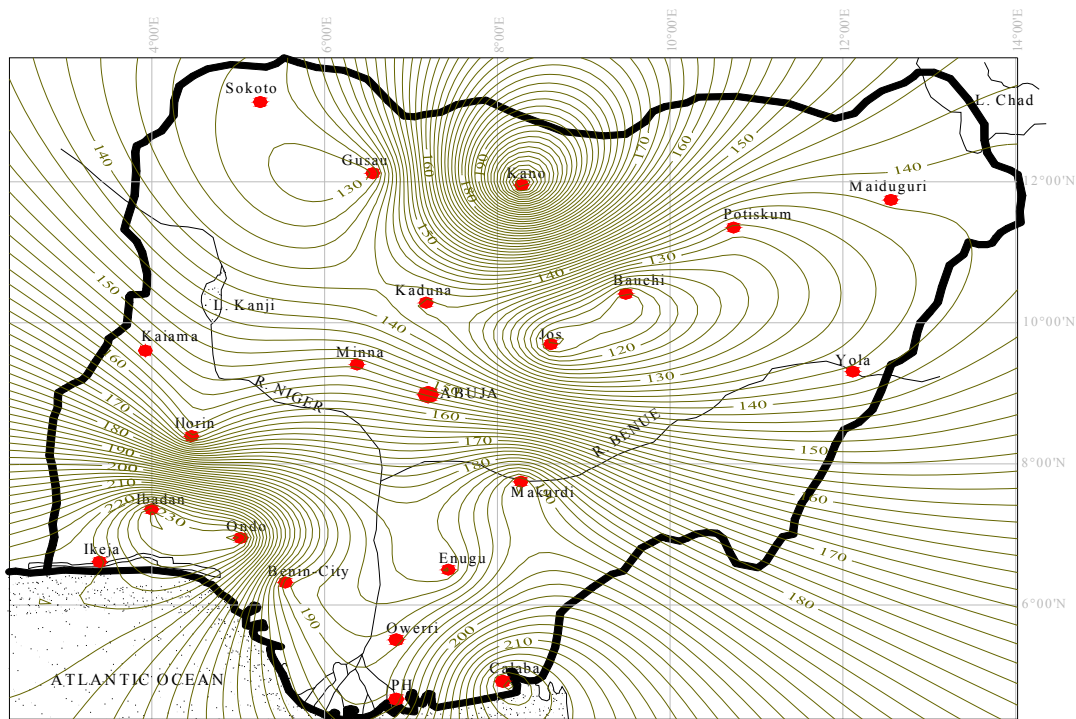


Figure 1 Peak daily rainfall (mm) Isohyet Map of 100 year return period

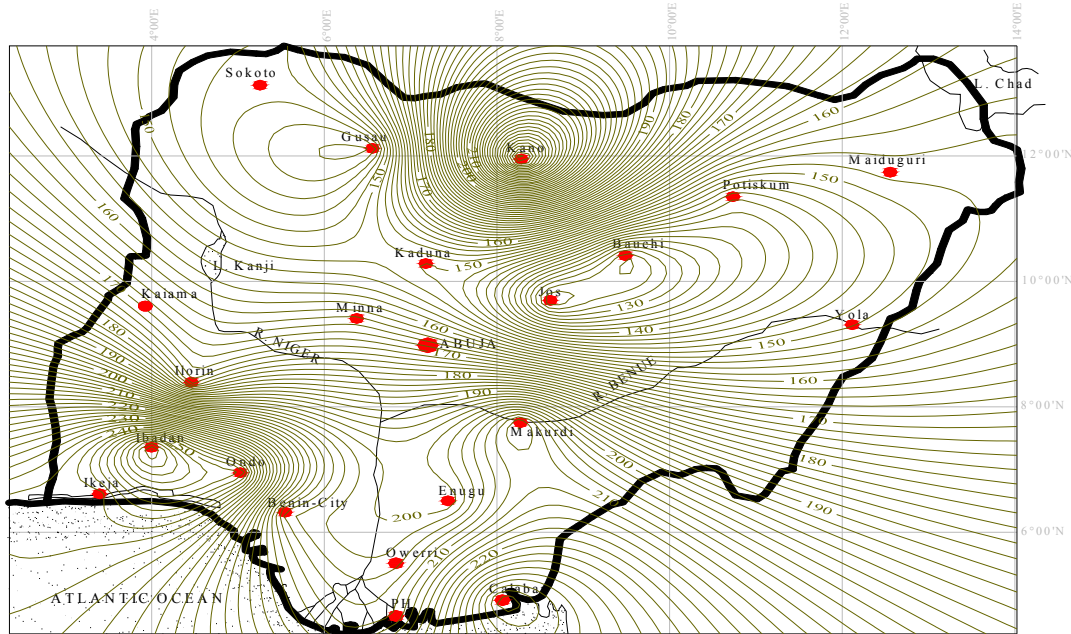


Figure 2 Peak daily rainfall (mm) Isohyet map of 200 year return period

Results and Discussion

The rainfall data was obtained for a period of fifty four years (1952 - 2005) for the selected Cities in Nigeria and the peak daily values were selected. The data were evaluated with various probability distribution functions to determine the best fitting model, the summary statistic is presented in Table 1 and the mathematical representations of the evaluated probability functions are presented in Table 2. For the purpose of theoretical determination of best fit probability function, statistical tools (goodness of fit tests) were adopted. The results of the statistical test score (the goodness of fit tests) and the best fit models are presented in Table 3 and 4 respectively. However, the quantile estimates for the selected Cities based on various return periods are presented in Table 5. The isohyet maps of 100 and 200 year return period were established and presented in Figure 1 and 2 respectively for the estimation of rainfall depth for any location with known longitude and latitude in Nigeria.

The statistical test score results at each station presented in Table 3 was used to decide which of the probability model (s) best fit the peak daily rainfall at each station. Examination of the goodness-of-fit test results reveals that in many cases there was very little difference between the various distributions for each station. Furthermore, the good fit assessment for all 20 stations also indicated that no one distribution ranked consistently best at all locations. However, the overall ranks for the 10 stations combined show that Log-Pearson type III was best to describe the peak rainfall. While, the overall ranks for the 8 stations combined show that Pearson type III was best to describe the peak rainfall. The overall ranks for 2 stations indicate that Log-Gumbel distribution is the best. The computed skew coefficients from the observed data in this study (Table 1) revealed that the peak daily rainfall distributions at all the stations were positively skewed. Also, the 3-parameter Pearsonian distributions, which take into cognizance the use of the skew coefficient in the estimation of future rainfalls, were found to be the best-fit models at most stations. In view of this, it can be said that the peak daily rainfall distribution in Nigeria are positively skewed and the Pearson III and Log-Pearson III distributions may be conveniently used for the prediction of future peak daily rainfall events anywhere in Nigeria.

Conclusions

From the results of six frequency distributions applied in this study, it suggests that the best frequency distribution obtained for the peak daily rainfall in Nigeria is the log-Pearson type III distribution, which occupies 50% of the total station number, followed by the Pearson type III distribution and log-Gumbel distribution, which accounts for 40% and 10% of the total station number, respectively. The outcome was relied on the results of four goodness-of-fit tests, Chi-square, Fisher's test, correlation coefficient and coefficient of determination. The proposed assessment procedure has been successfully used to identify the best probability distributions that could provide accurate peak daily rainfall estimates for Nigeria. The results of the frequency analysis suggest log-Pearson

type III and Pearson type III distributions has the primary distribution pattern for this study site and should be used as a universal distribution model for the prediction of peak daily rainfalls in Nigeria.

References

1. Adegboye, O.S and Ipinyomi, R.A (1995) “Statistical tables for class work and Examination. Tertiary publications Nigeria Limited, Ilorin, Nigeria, pp. 5 - 11
2. Bhakar, S.R., Bansal, A.K, Chhajed, N, and Purohit, R.C (2006). Frequency analysis of consecutive days maximum rainfall at Banswara, Rajasthan, India. ARPN Journal of Engineering and Applied Sciences.
3. Boughton, W.C (1999). A daily rainfall generating model for water yield and flood studies. Cooperative Research Centre for Catchment Hydrology, Australia.
4. Chapman, T (1994). Stochastic models for daily rainfall. The institution of Engineers, Australia, National Conference Publication 94 (15), 7-12.
5. Chowdhury, J.U. and Stedinger, J.R. (1991) “Goodness of fit tests for regional generalized extreme value flood distributions.” *Water Resource. Res.*, 27(7) : 1765 – 1776.
6. Dibike, B.Y and Solomatine, D.P (1999) “River flow forecasting using Artificial Neural Networks”. Paper Presented at European Geophysical Society (EGS) XXIV General Assembly. The Hague, The Netherlands, 1 – 11.
7. Edwards, K.A, Classen, G.A, and Schroten, E.H.J (1983). The water resource in tropical Africa and its exploitation. International Livestock Centre for Africa (ILCA) Research Report No. 6. Chapter 2: Climate and rainfall in the tropics.
8. Guevara, E (2003). Engineering Design Parameters of storms in Venezuela. *Hydrology Days*, 80-91.
9. Lee, C (2005). Application of rainfall frequency analysis on studying rainfall distribution characteristics of Chia-Nan plain area in Southern Taiwan. *Journal of Crop, Environment & Bioinformatics* (2). 31-38. 189 Chung-Cheng Rd, Wufeng.
10. Mustapha, S. and Yusuf, M.I. (1999) “A Textbook of Hydrology and Water Resources”, Jenas Prints & Publishing Co., Abuja, Nigeria, pp. 164 – 184, First edition.
11. Murray, R.S and Larry, J.S (2000) “Theory and problems of statistics” Tata Mc Graw – Hill Publishing Company Limited, New Delhi, pp. 314 – 316, Third edition.
12. Ogunlela, A.O (2001) “ Stochastic Analysis of Rainfall Events in Ilorin, Nigeria” *Journal of Agricultural Research and Development*. Volume 1: 39 -50.
13. Phien, H.N and Ajirajah, T, J (1984). Applications of the log-Pearson Type-3 distribution in hydrology. *Journal of hydrology*, 73; 359-372.
14. Salami, A.W (2004). Prediction of the annual flow regime along Asa River using probability distribution models. *AMSE periodical*, Lyon, France. *Modelling C-2004*, 65 (2), 41-56. (http://www.amse-modeling.org/content_amse2004.htm)

15. Tao, D.Q, Nguyen, V.T and Bourque, A (2002). On selection of probability distributions for representing extreme precipitations in Southern Quebec. Annual Conference of the Canadian Society for Civil Engineering. 5th -8th June 2002. pp 1-8.
16. Topaloglu, F. (2002) “Determining Suitable Probability Distribution Models for Flow and Precipitation Series of the Seyhan River Basin”. Turk Journal of Agric.26: 189 – 194.
17. Viessman, .W, Krapp, J.W and Harbough, T. E (1989) “Introduction to Hydrology”. Harper and Row Publishers Inc., New York. pp. 675 – 695, Third edition.
18. Warren, .V, Terence, E.H and. John, W.K (1972) “Introduction to hydrology” Educational Publishers, New York, pp. 106 – 141, Second edition.

1/24/2009

Electrical Resistivity Method in Engineering and Environmental Studies: A Case Study of Gbagada Area, Lagos State, Nigeria.

Oyedele, K.F and Ojo, A.O
Dept of physics (Geophysics Programme)
University of Lagos, Lagos Nigeria.
kayodeunilag@yahoo.com

Abstract

Foundation problems are caused by a combination of soil conditions, the weather and inadequate foundation maintenance. This paper presents the results of electrical resistivity method in delineating subsurface soil conditions at Gbagada area, Lagos state Nigeria. Three main soil types were mapped: namely sand, clayey sand and clay. The depth to sand bodies range from 1.18 to 18.09 m while the depth to clay bodies range from 3.43 to over 25.14m. On the other hand the depth to clayey sand bodies range from 1.88 to over 23.64m. It is concluded that the depth to clay layers in most parts of the study area is near the surface. [New York Science Journal. 2009;2(3):13-20]. (ISSN: 1554-0200).

Keywords: Electrical resistivity, sediment, lithology and stratigraphy.

1 Introduction

Since soil condition is one of the sources of foundation problems the need to know the strength, the fitness and the overall subsurface stratigraphy in an area prior to construction works cannot be overemphasized. Other sources of foundation problems include the weather and inadequate foundation maintenance.

Symptoms of foundation problems include cracks in bricks and sheetrock, windows that won't open, doors that won't close, cracks in the foundation, cracks in tile floors and many more. Sometimes some of these symptoms can simply be cosmetically repaired. Complete underpinning of the foundation may not be necessary. It takes an expert to properly diagnose true foundation problems. Just because you have some or all of these symptoms, does not mean that you need foundation repair. However, if adequate precautionary measures are taken into consideration before the commencement of construction exercise some of these problems if not total would have been taken care of.

In many coastal areas of the world, the near surface soil is of expansive clay. Expansive clay behaves differently than sandy soil. Sandy soil does not expand when it gets wet. The water fills the air spaces between the grains of sand. Because of this, the soil volume does not change and there is little movement of structures supported by the soil when the soil moisture conditions alternate between wet and dry. Meanwhile expansive clay soil expands when it absorbs water. Water becomes bound to the clay particles. As the soil goes through wet and dry periods, the soil expands and contracts. Structures sitting on top of the soil rise and fall with the soil. If this happened uniformly across the structure, damage to the foundation and finishes from soil movement would be limited. Unfortunately, uniform shrinking and swelling doesn't usually happen. The result is "differential" foundation movement, which causes cracking and distress in the foundation and finishes.

Although there may be a number of layers and types of expansive clay or other soil under a particular structure, the shrinkage and swelling process is usually limited to soil that is near enough to the ground surface to be affected by climatic conditions. Many Engineers refer to these upper soil layers as the "active zone". While the depth of the 'active zone' depends on both site and soil conditions. This depth ranges between 2 and 5 meters below ground surface.

To this end, electrical resistivity survey method was employed to classify the soil conditions at Gbagada area of Lagos State, Nigeria with a view to provide information on the subsurface stratigraphic variations with respect to depths. This method is the most widely used geophysical techniques, very efficient and cost effective (Neil and Ahmed, 2006, Susan, 2004, Hinze, 1990, Fitterman et al, 2001, Kontar and ozorovich, 2006 and Oyedele, 2008).

2 Geologic setting

The study area is situated in Lagos (fig1). The surface geology is made up of the Benin formation (Miocene to Recent) and the recent littoral alluvial deposits. The Benin formation consists of thick bodies of yellowish (ferruginous) and white sands (Jones and Hockey, 1964). Multi-layer lithology have been classified by Longe et al, 1987, into three types namely admixtures of sand and clay, coarse sand and clay. The thickness varies from 8 to 35m.

3 Data acquisition and processing

The field data were acquired using Terrameter SAS1000 system. About twenty-four vertical electrical sounding (VES) using Schlumberger electrode array system were conducted. Only results for fourteen VES stations were presented. As a control measure to geographical data, one borehole was drilled to aid lithological delineation.

The acquired data is processed using WinGlink software programme. This is a powerful software package that was designed to read and store data acquired by different geographical surveys carried out in an area of interest, as well as other auxiliary information. By this technique, erroneous interpretations arising from manual techniques are eliminated. The processed data were presented in the form of 1-D resistivity models, inferred sediments and contoured maps.

4 Results and discussion

Resistivity Curves

Figure 2 shows representative samples of 1-D models resistivity field curves obtained from the study area. Visual inspection of the field model curves shows a typical 3 to 5-layered case. The detailed stratigraphic sequence of the area is presented in Table1.

Inferred sediments

The geoelectric section alongside with the drilled borehole was used to delineate the stratigraphic succession in the study area (table1).

Beneath VES 1, the lithology consists of topsoil, medium sand, clay and coarse sand. Here the depths to sand layers range from 1.18 to over 5.57m while the average depth to clay layer is 5.57m. Beneath VES, 2 the lithology consists of topsoil, medium sand and coarse sand. The average depth to sand layer is greater than 18.09m. There is no clay layer in this zone as the current terminated in the third layer.

Beneath VES 3, the stratigraphy is made up of top soil, medium sand, clayey sand and coarse sand. The depths to sand layers range from 1.61 to over 17.04m while the depth to clayey sand is 17.604m. Beneath VES 4, the sediment is made up of topsoil, medium sand clayey sand and coarse sand. The depths to sand bodies range from 3.05 to over 21.95m. On the other hand, the depth to clayey sand layer is about 21.95m.

Beneath VES 5, the sediments consist of topsoil, medium sand, clay and coarse sand. The depths to sand bodies range from 3.74m to over 10.55m, while the depth to clay layer is 10.55m. The sediments beneath VES 6 consist of topsoil, medium sand, clay and coarse sand. The depths to sand bodies range from 1.62 to over 6.15m while the depth to clay layer is 6.15m. The stratigraphy beneath VES 7 is made up of the topsoil, medium sand, clay and coarse sand. Here the depth to sand layers varies from 2.8m to over 11.03m while the depth to clay layer is 11.03. The lithology beneath VES 8 consists of topsoil, clayey sand, medium sand, clay and coarse sand. The depths to clay bodies range from 11.0m to 39.09m while the depths to sand layers vary from 3.77 to 39.09m.

The stratigraphy beneath VES 9 is made up of topsoil, clay, medium sand, clay and coarse sand. The depths to clay layers vary from 7.05 to over 25.14m. The sediments beneath VES 10 consist of topsoil, clay, medium sand and clay. The depth to clay layers range from 4.69 to over 10.26m.

Beneath VES11, the sediments consist of topsoil, medium sand, clay and coarse sand and clayey sand. The depths to sand layers vary from 1.33 to 11.97m while the depth to clay layer is 3.43m. The lithology

beneath VES12 consists of topsoil, medium sand, clayey sand, and coarse sand. The depths to sand body ranges from 1.87m to over 18.49m while the depth to clayey sand layer is 18.49m.

The sediments Beneath VES13, consist of topsoil, medium sand, clayey sand and clay .The depth to clay layer is over 23.64m while the depth to sand body is 2.1m. On the other hand, the lithology beneath VES14 is made up of topsoil, medium sand, clay coarse sand, and clay. The depths to clay layer range from 3.91 to over 16.22m while the depths to sand body vary form 1.54 to 16.22. On the whole the thicknesses of the sand layers vary from 0.80 to 28.09m while the thicknesses of the clay layers vary from 3.43 to 25.14m.

Contoured maps

The data in table 1 were used as input into the WinGLink software Programme to produce series of maps (Figs 3 and 4).

Figures 4a and 4b show the isopach maps of sand bodies between 0 to 15m and 0 to 20m respectively. In figure 3a, the thicknesses of the sand bodies beneath VES 3,4,6,7,8,11,12,13 and 14 range from 1.18 to 3m. The thickness of the sand layers beneath VES 1,5, 9 and 10 vary from 3 to 6m, while the thickness of the sand body beneath VES 2 vary from 9 to 12. Figure 3c shows the isopach map of depths to freshwater layer which vary from 2 to over 22m. On the other hand, figures 4a to 4d show the isoresistivity depth-slice maps at 5m, 10m, 20m and 30m respectively. On the whole, the resistivity values at these depths vary from 50 to 1000 ohm-m.

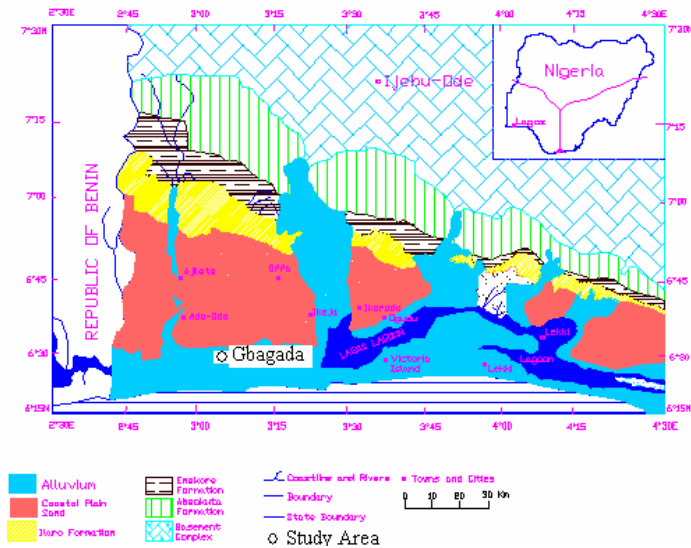


Fig 1: Geological map of Lagos showing the study area

Ves 1

ves2

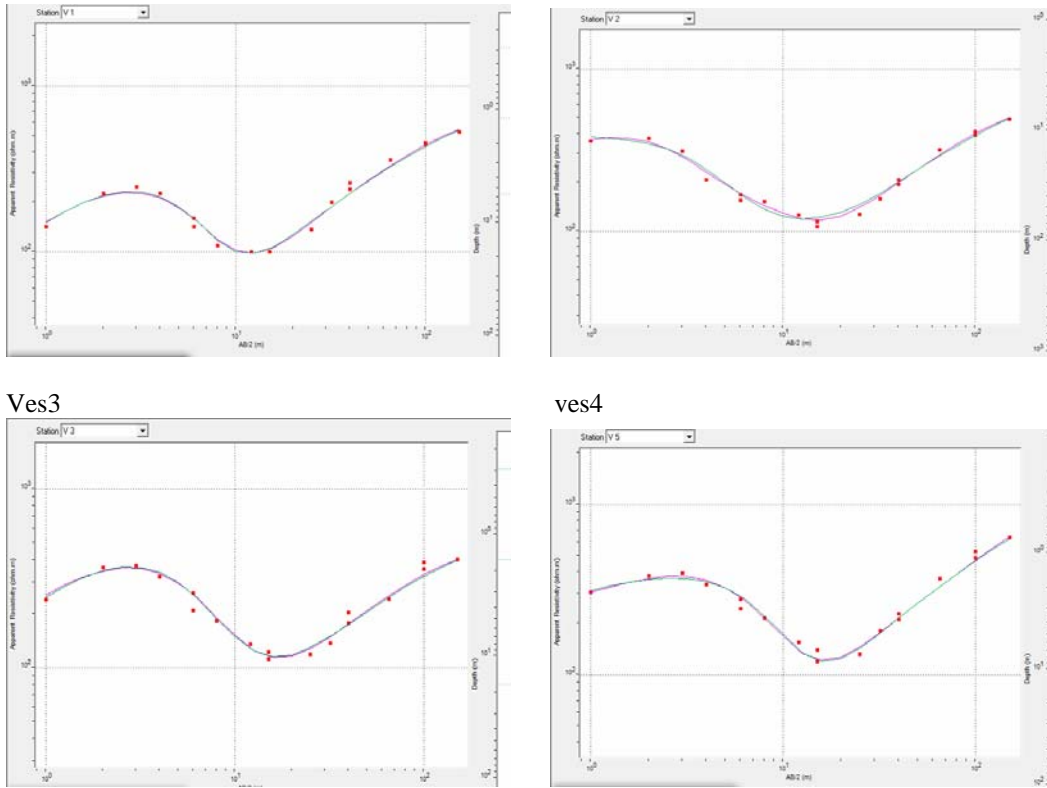
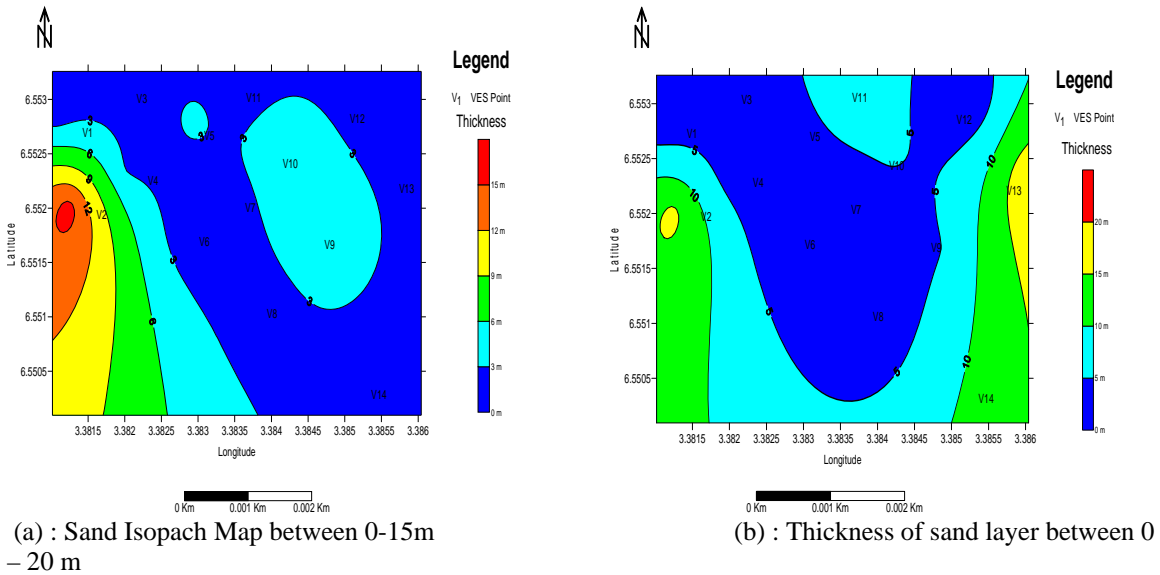


Fig 2: Representative of 1-D model resistivity curves



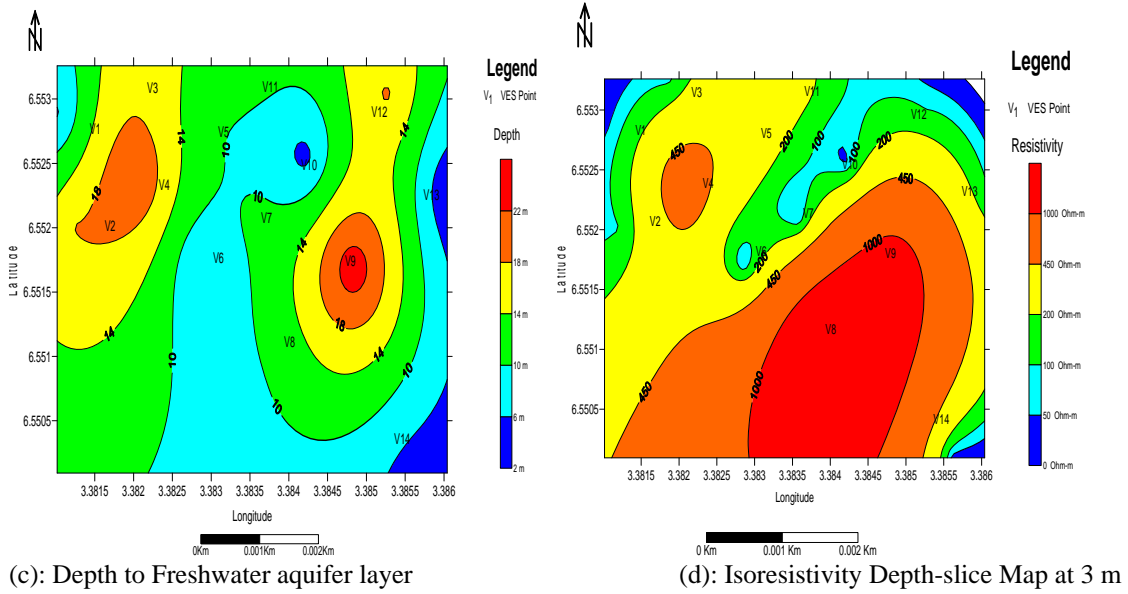
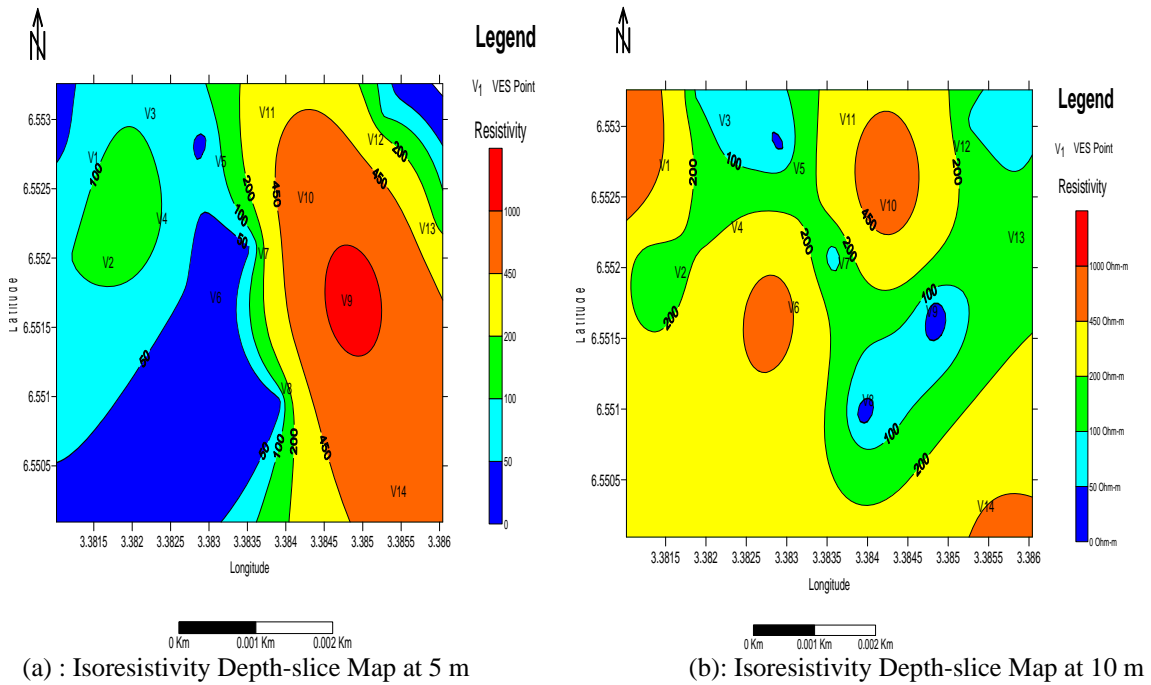
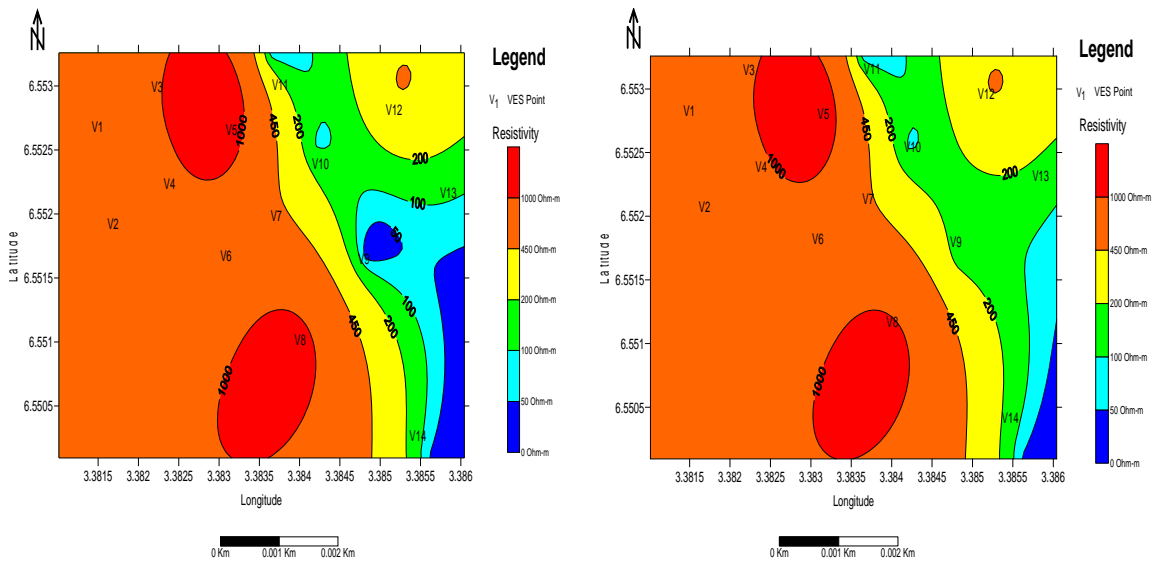


Fig 3: Contoured maps for sand bodies and depth to freshwater layers.





(c): Isoresistivity Depth-slice Map at 20 m
30 m

(d): Isoresistivity Depth-slice Map at 30 m

Fig 4: Isoresistivity Depth-slice Map at 5m, 10m, 20m and 30m respectively.

Table 1: Measured parameters/Inferred sediments

VES Station	Layer	Resistivity (Ohm-m)	Thickness (m)	Depth (m)	Lithology
1	1	55.39	0.28	0.28	Topsoil
	2	742.85	0.9	1.18	Medium Sand
	3	32.98	4.39	5.57	Clay
	4	934.95	-	-	Coarse Sand
2	1	388.14	1.94	1.94	Topsoil
	2	102.08	16.15	18.09	Medium Sand
	3	911.54	-	-	Coarse Sand
3	1	101.52	0.29	0.29	Topsoil
	2	763.42	1.32	1.61	Medium Sand
	3	87.65	15.43	17.04	clayey sand
	4	653.12	-	-	Coarse Sand
4	1	386.35	0.48	0.48	Topsoil
	2	666.95	2.57	3.05	Medium Sand
	3	155.25	18.9	21.95	clayey sand
	4	586.5	-	-	Coarse Sand
5	1	158.46	0.2	0.2	Topsoil
	2	420.55	3.54	3.74	Medium Sand

	3	43.73	6.81	10.55	Clay
	4	1812.75	-	-	Coarse Sand
6	1	105.39	0.27	0.27	Topsoil
	2	471.89	1.35	1.62	Medium Sand
	3	42.56	4.53	6.15	clay
	4	625.98	-	-	Coarse Sand
7	1	138.93	0.66	0.66	Topsoil
	2	464.08	2.17	2.83	Medium Sand
	3	54.8	8.2	11.03	clay
	4	534.96	-	-	Coarse Sand
8	1	313.92	1.33	1.33	Topsoil
	2	57.88	0.55	1.88	clayey sand
	3	1975.68	1.89	3.77	Medium Sand
	4	34.44	7.23	11	clay
	5	1294.98	28.09	39.09	Coarse Sand
	6	16.71	-	-	clay
9	1	121.34	1.19	1.19	Topsoil
	2	27.4	1.16	2.35	clay
	3	1368.12	4.7	7.05	Medium Sand
	4	22.93	18.09	25.14	clay
	5	143.38	-	-	Coarse Sand
10	1	116.64	2.19	2.19	Topsoil
	2	42.81	2.5	4.69	clay
	3	757.34	5.57	10.26	Medium Sand
	4	89.66	-	-	Clay
11	1	89.08	0.53	0.53	Topsoil
	2	140.3	0.8	1.33	Medium Sand
	3	43.22	2.1	3.43	clay
	4	269.74	8.54	11.97	Coarse Sand
	5	67.62	-	-	clayey sand
12	1	206.37	0.9	0.9	Topsoil
	2	862.39	0.97	1.87	Medium Sand
	3	89.61	16.62	18.49	clayey sand
	4	485.41	-	-	Coarse Sand
13	1	44.01	0.41	0.41	Topsoil
	2	391.8	1.69	2.1	Medium Sand
	3	121.26	21.54	23.64	clayey sand
	4	73.52	-	-	clay

14	1	90.81	0.62	0.62	Topsoil
	2	183.78	0.92	1.54	Medium Sand
	3	30.24	2.37	3.91	clay
	4	549.79	12.31	16.22	Coarse Sand
	5	47	-	-	clay

5 Conclusion

The soil conditions at Gbagada area, Lagos State , Nigeria using Electrical resistivity survey technique revealed that the sediments consists of topsoil, medium sand, clay, clayey sand and coarse sand. Based on the results of the investigations, it is concluded that major parts of the area consist of clay and clayey sands at shallow depths and these might pose a serious threat to the survival of engineering structures in this type of environment if adequate care is not considered.

Correspondence:

Oyedele, K.F and Ojo, A.O
 Dept of physics (Geophysics Programme)
 University of Lagos, Lagos Nigeria
kayodeunilag@yahoo.com

References

- Fitterman, D.V and Deszez-Pan, M.(2001).Geophysical mapping of saltwater intrusion in everglades national park. First international conference on saltwater intrusion and coastal aquifers monitoring, modeling and management, morocco.
- Hinze, W.J, (1990). The role of gravity and magnetic methods in engineering and environmental studies, in ward, S.H, editor, Geotechnical and environmental Geophysics, Vol.1: Review and tutorial: Society of Exploration Geophysics, 389p.
- Jones, A.A and Hockey, R.A (1964). The geology of part of southern Nigeria. Geology survey. Nigeria. Bull. 31.10p.
- Kontar, E.A and Ozorovich, Y.R. (2006).Geo-electromagnetic survey of the fresh/saltwater interface in the coastal southeastern Sicily, cont shelf Res. 26: 343-551p.
- Longe, E.O Malomo, S. and Olorunniwo P. (1987). Hydrogeology of the Lagos metropolis journ. of Afr. Earth Sc. 6(2): 163-174p.
- Neil, A. and Ahmed, I. (2006). A generalized protocol for selecting appropriate geophysical techniques. Dept of Geol. and Geophys. University of Missouri-Rolla. Rolla, Missouri. 19p.
- Oyodele, K.F (2008). Effectiveness of the Electrical Resistivity Methods in Coastal Hydro geophysical studies. Journ. Env. Hydr. Vol. 16, paper 16.

1/27/2009

Total Dissolved Solids (TDS) Mapping In Groundwater Using Geophysical Method

Oyedele, K. F.
Department of Physics,
University of Lagos,
Lagos, Nigeria.
e-mail: kayodeunilag@yahoo.com

Abstract

The reliability of electrical resistivity measurements to delineate subsurface total dissolved solid (TDS) in groundwater in Lagos, Nigeria, has been examined. Data from parametric resistivity soundings were correlated with laboratory measurements to provide information on the degree of total salinity of each aquiferous unit, depths to iso-conductivity surfaces and the various usage to which the groundwater from the studied area can be put to. The study revealed that TDS contrasts inferred from resistivity data can be used for effective monitoring and economic evaluation of groundwater salination. [New York Science Journal. 2009;2(3):21-31]. (ISSN: 1554-0200).

Keywords: Dissolved Solids (TDS); Groundwater; Geophysical Method

Introduction

Exploration for groundwater is becoming more attractive in the coastal area of Lagos, Nigeria, due to the ever increasing demand for water supply, especially in areas with insufficient surface water supplies for daily activities. Most boreholes in Lagos State obtain water from aquifers within the coastal plain sands (Kampsax and Sshwed, 1987). The water in this formation is, however, not always potable due to urban waste disposal and seawater intrusion (Fatoba and Olorunfemi, 2004; Oyedele, 2006). Other possible sources of total salinity in surface water and groundwater include atmospheric inputs in the form of wet and dry deposition and also weathering of minerals in soils which can either dominate the water chemistry (Adamson and Hornung, 1990). Total salinity is often referred to as total dissolved solid (TDS) while soil particles in the water are referred to as total suspended solids (TSS).

The threat posed by pollution in the surface water and groundwater on the economic survival and sustainable development of the inhabitants of Lagos has required cost-effective approach to mapping and monitoring the impact of TDS on soil water chemistry. Soluble salts in the soil solution exert additional soil moisture tension, which can exceed the crops salt tolerance (salinity threshold), thus causing potential yield reduction (Brian et al., 2002). The potential energy of soil water is also reduced by the presence of solutes.

Neglecting to understand the quality of source water for either domestic, agricultural or industrial usage is one of the most common reasons for failure in optimal performance in most human organs, healthy plant growths and quality pharmaceutical products. Basically, two distinct methods exist for the determination of TDS in soil water. These methods can be described as destructive and non-destructive. The former involves taking repeat samples using a soil auger/core sampler, hence the geology is continually disturbed. Alternatively, standpipe piezometers can be installed or the groundwater level obtained from existing wells. Geophysical methods are non-destructive and combine speed, accuracy and cost-effectiveness in mapping subsurface soil and rock stratigraphy. The present study utilised the electrical resistivity method to characterise the TDS level of each aquiferous layer as a means of predicting and monitoring their occurrence in soil water. Moreover, in order to give better support to the geological and hydrogeological interpretation of geophysical data, three wells were drilled in the study area. Also parametric soundings were carried out beside six abandoned boreholes and water samples were taken from the wells for laboratory analysis.

Geology and Hydrogeology

The areas investigated (Fig. 1) are made up of sediments from coastal plain sands and Alluvium deposits (Rofe and Lapworth, 1987; Jones and Hockey, 1964). The coastal plain sands consist of soft, very porous sorted clayey sands, pebbly sands, sandy clays and rare thin lignites. Their thicknesses increase from north to south and can be up to 2000 m. The alluvial deposits of the major rivers consist of unconsolidated sands,

clay and muds observable in boreholes drilled at Lekki, Ikoyi, Ajah and Victoria Island (Oyedele and Meshida, 2006). The geoelectric sounding conducted penetrated this formation. Two principal climatic seasons can be recognised: a dry one from November to March, and a wet one from which starts from April and ends in October, with a short dry spell in mid-August. Average annual precipitation is put at 1700 mm and serves as a major source of groundwater recharge (Jeje, 1983).

Electrical Resistivity Surveys

For this investigation, the Schlumberger depth sounding method were employed (Roberto et al., 2003). The method is capable of depicting subsurface structure distinctly, delineate contaminated zones of groundwater, adequate depth penetration and it requires less labour. This method involves the introduction of electric current into the ground via two current electrodes and the measurement of the distribution of the resulting potential on the ground surface via two potential electrodes (Fig. 2).

Terrameter SAS 4000 was employed to take the measurement, having greater depth of penetration and high signal to noise ratio. The current and potential electrode spacing were measured in metres and varied from 1 to 500 m for the current electrodes and from 0.25 to 40 m for the potential electrodes. About 120 vertical electrical soundings (VES) were obtained within the study area. The location and distribution of the VES stations were based on the available space as well as the accessibility within the study locations.

Hydrogeochemical Data Surveys

In addition to the geoelectric data used for these studies, three shallow wells were drilled to the depth of 40 m using manual rotary drilling rigs (Fig. 3) for the purpose of giving better control/support to the geological and hydrogeological interpretation of geophysical data. Water samples were then taken from the borehole drilled for laboratory analysis at the Lagos State Water Corporation, Iju, Lagos, Nigeria.

Resistivity Data Processing

The VES data were initially subjected to interpretation using manual curve matching technique. This entails the use of two-layer model curve alongside auxiliary curves. The resulting number of layers alongside their resistivity values were used as input model for the computer simulation using RESIX-IP (1988). This exercise was aimed at reducing the influence of human error in respect of the manual curve matching interpretation. After adequate interpretative iterations, the resulting weighted root mean square error average for the VES stations was 2.3%.

The second stage of data processing involved using the resistivity values of the computer modelling for all the VES stations to calculate the conductivity of all the aquifer units in the study area since conductivity is the inverse of resistivity (Table 1). However, the TDS of a water sample may be obtained by multiplying its conductivity in micromhos per centimetre ($\mu\text{mhos/cm}$) by an empirical factor which may have a range of 0.55 to 0.9, depending on its soluble components (Greenberg et al., 1980). The values obtained from the laboratory analysis of TDS values was correlated with the one inferred from resistivity method. Based on this correlation, 0.725 empirical factor was used.

Results and Discussion

The processed resistivity data were used to produce tables and maps showing the morphology of the subsurface layers.

Lithologic Deduction / Aquifer Characterisation

The data on Table 1 were used to produce all the geoelectric sections of the area. Visual evaluation of the plotted field data revealed a smooth geometry of typical 4-layer or combined minimum type characteristics of a sedimentary terrain (Fig. 4). The prevailing hydrostratigraphic units within the study area consists of sand and clay, intercalated in most cases with clayey sand and sandy clay. The aquifer type ranges from semi-confined to confined. The shallow aquifer seems to be unconfined, thus making them to be vulnerable to surface contamination. On the other hand, the deeper aquifers are mostly semi-confined.

Conductivity Levels in Soil Water and Rock Stratigraphy

Maps of iso-conductivity surfaces (Fig. 5) were produced using the data in Table 1 with the help of SURFER program. This prevents the error associated with manual contouring techniques. Using

conductivity contrasts, total salinity may be found between 0.5 and 0.022 ds/m iso-conductivity surfaces. The average depth ranges from 5 to 125 m. This map serves as a means of predicting/monitoring the subsurface soil water conductivity levels.

Evaluation of Total Dissolved Solids (TDS) from Resistivity Data

By inputting the data in Table 1 into SURFER program, maps of TDS values for each stratigraphic layer were produced (Figs. 6-9). Information on these maps resemble that of depths to iso-conductivity surfaces contour maps. TDS values are measured in parts per million (ppm). One ppm is equivalent to 1 mg of solute per kg of solution. Therefore, 1% is equal to 10,000 ppm.

In both Layers 1 and 2, over 95% of the surveyed areas have TDS values to be less than 465 mg/l , an indication of very good quality water. In Layer 2, over 60% of the area have TDS values that range from 604-465 mg/l , an indication of good quality water. In this layer also, about 15% of the area have TDS values that range from 23237-1010 mg/l , an indication of saline region. In Layer 4, over 70% of the area have TDS values that range from 23237 to 1010 mg/l , an indication of intermediate quality water.

Evaluation of TDS from Laboratory Measurements

Water samples from where the parametric soundings was conducted around the abandoned six wells were taken for laboratory analysis. Analyses performed on the samples include TDS, colour, turbidity, iron and nitrates (Table 2). The TDS values inferred from resistivity measurements were correlated with those obtained from the laboratory (Table 3). Using the data in this table, Fig. 10 was produced.

Evaluation of Groundwater Suitability

For potable drinking water, WHO proposes 600-1000 mg/l of TDS as the lower and upper limits of general acceptability. For industrial and agricultural produces, different range of TDS values exist. The results of the investigation (i.e., TDS) were compared with the WHO recommended standards suitable for industrial and agricultural purposes (Tables 4 and 5).

Based on resistivity and total dissolved solids contrasts inferred from geoelectric data, Tables 6 and 7 were proposed for soil water and sediments within the study area.

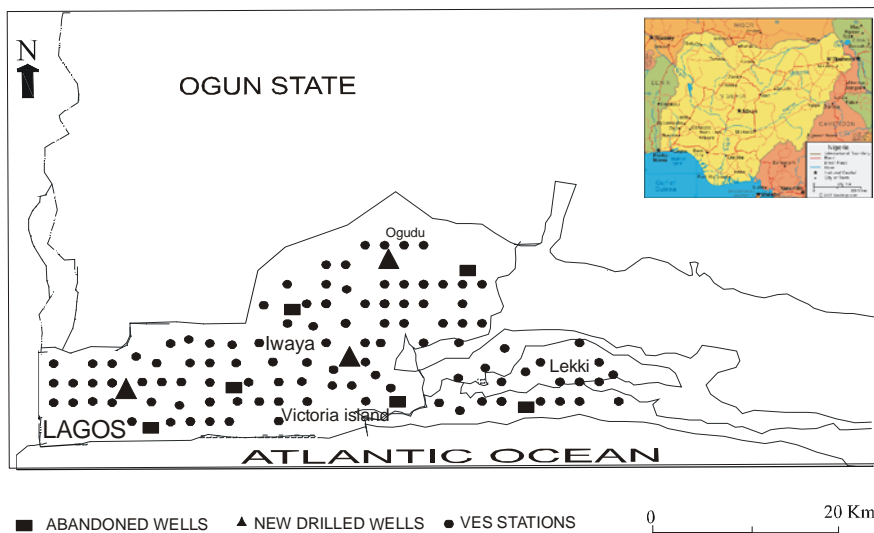


Fig 1: Geological map of Lagos showing the study area (Kamsax and Sshwed, 1997)

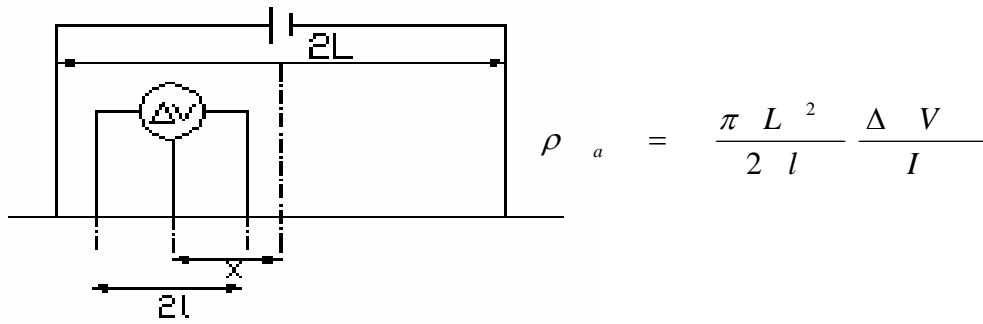


Fig 2: Schlumberger electrode array configuration

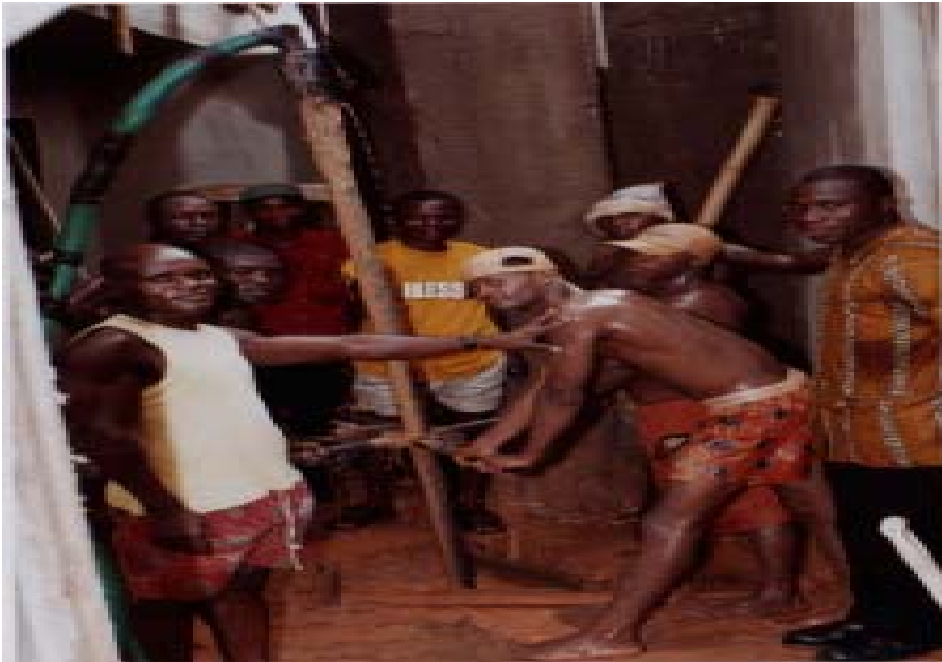


Fig 3a: Drilled borehole 2 in the type locality.



Fig 3b: Drilled borehole 3 in the type locality

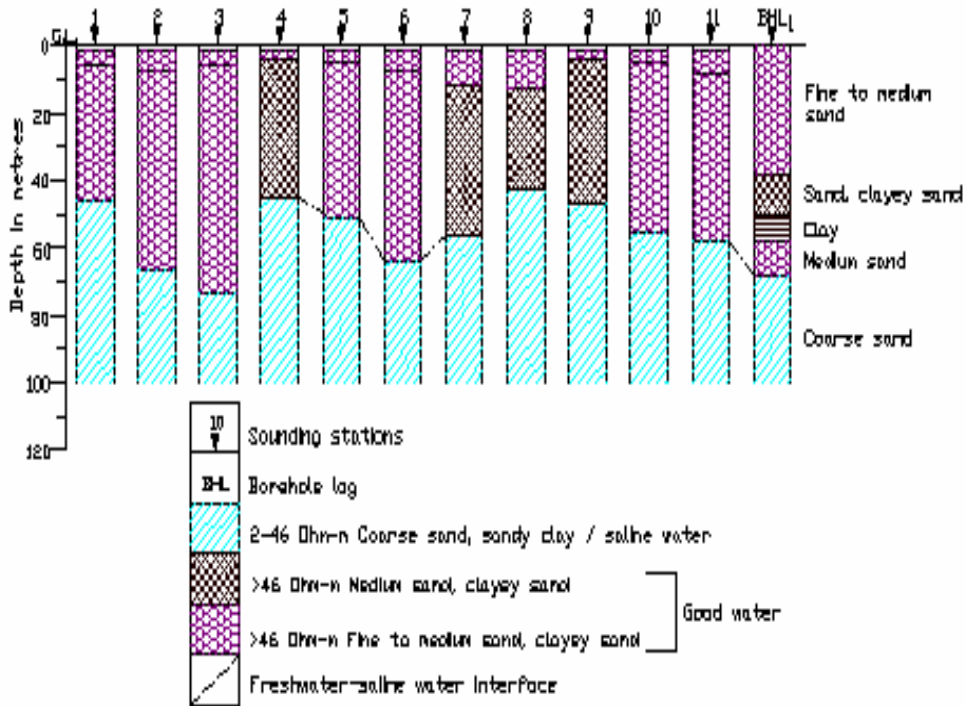


Fig 4: Representative sample of geoelectric sections correlated with borehole log 1

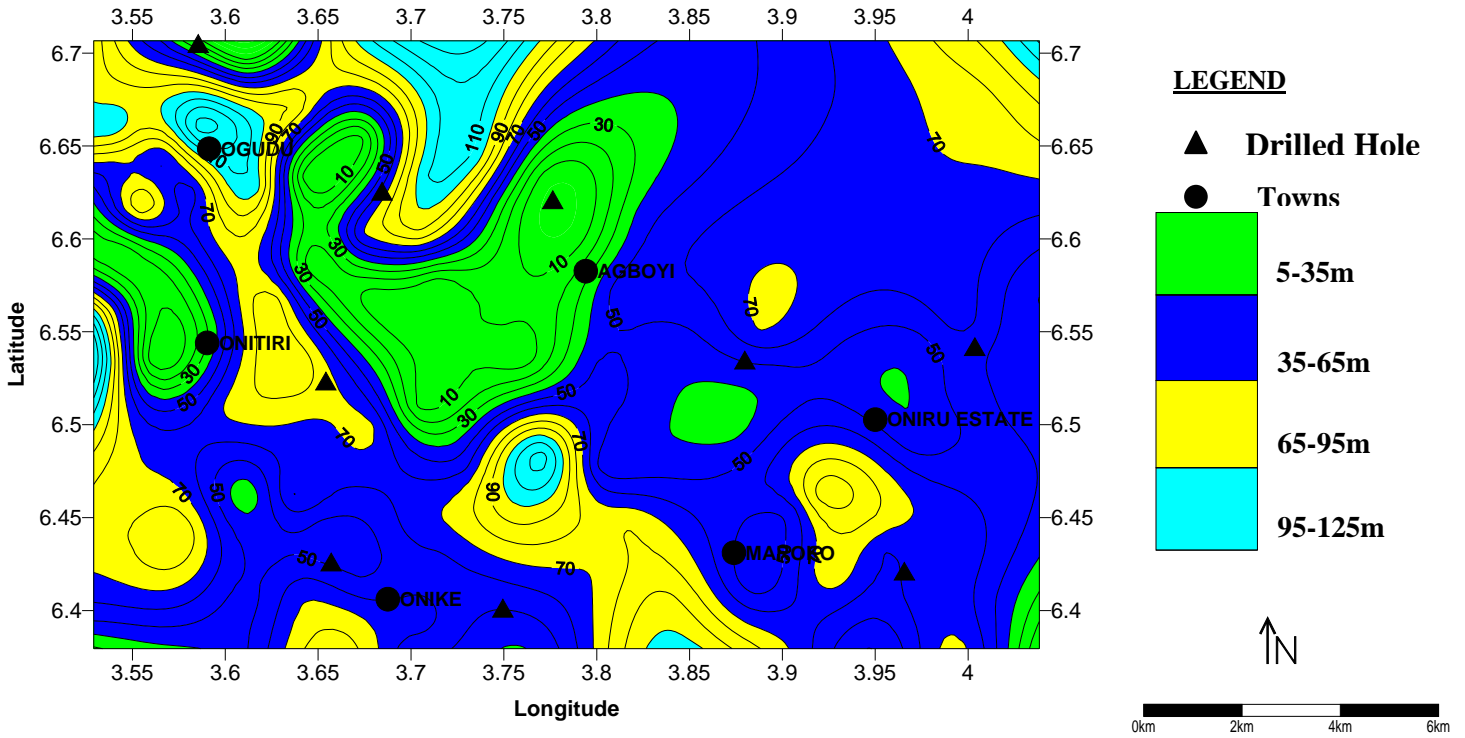


Fig 5: Depth to 0.5-0.022ds/m iso- conductivity surfaces. Contour interval is 10m. Average depth is 69m.

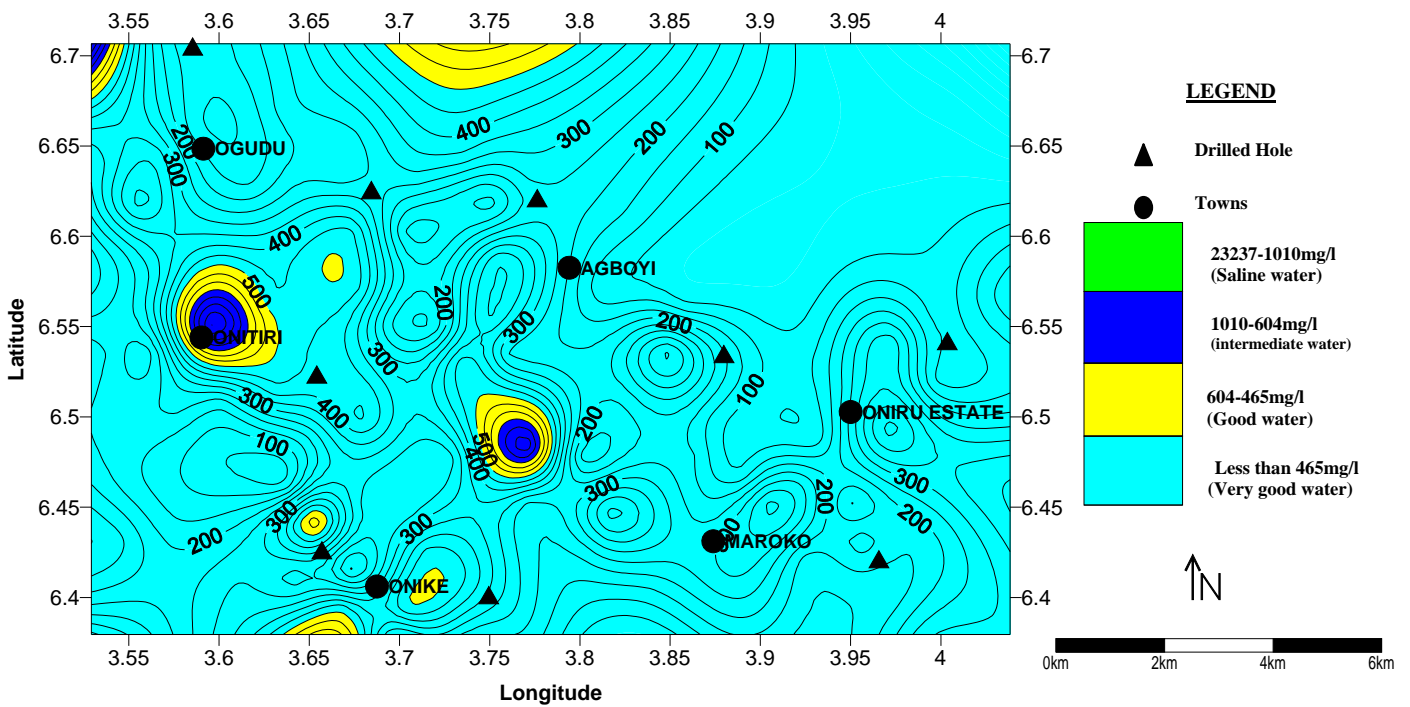


Fig 6: Morphology of subsurface TDS for layer I. Contour interval is 50mg/l.

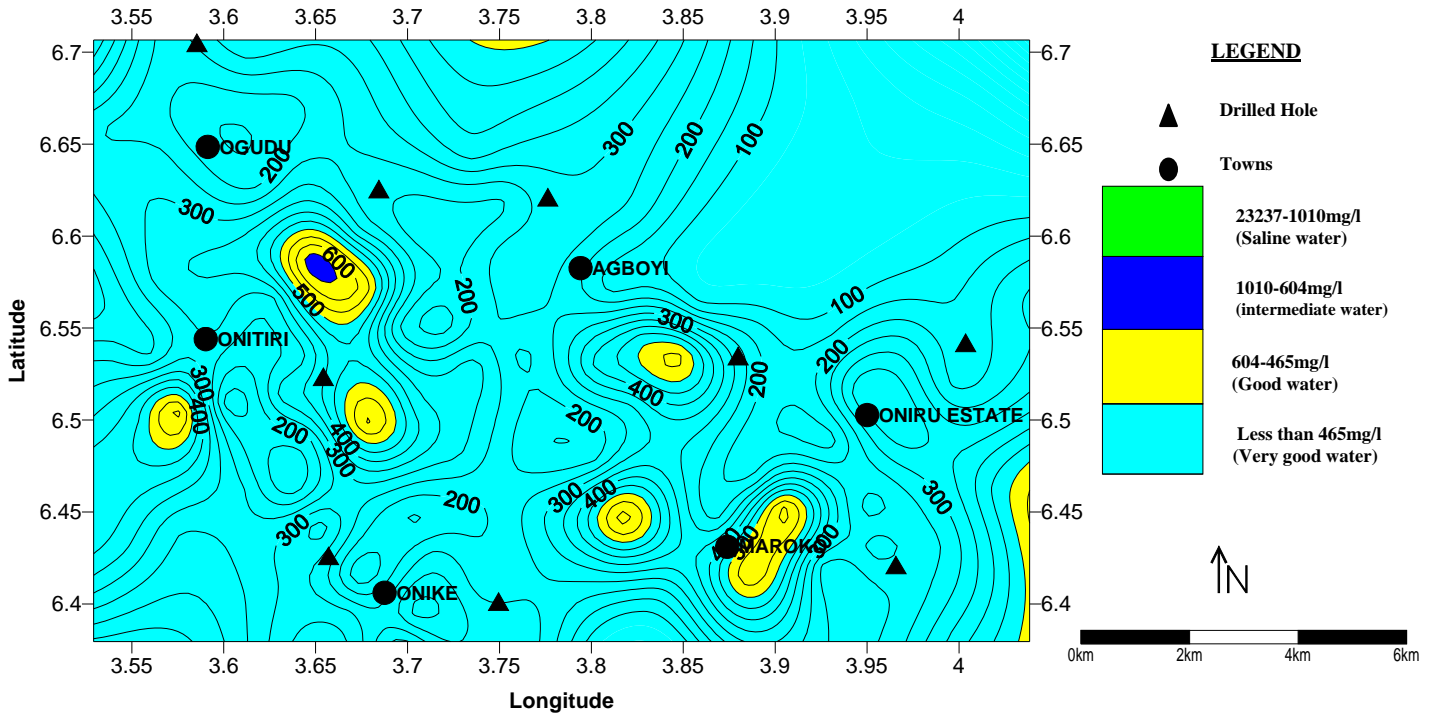


Fig 7: Morphology of subsurface TDS for layer II. Contour interval is 50mg/l

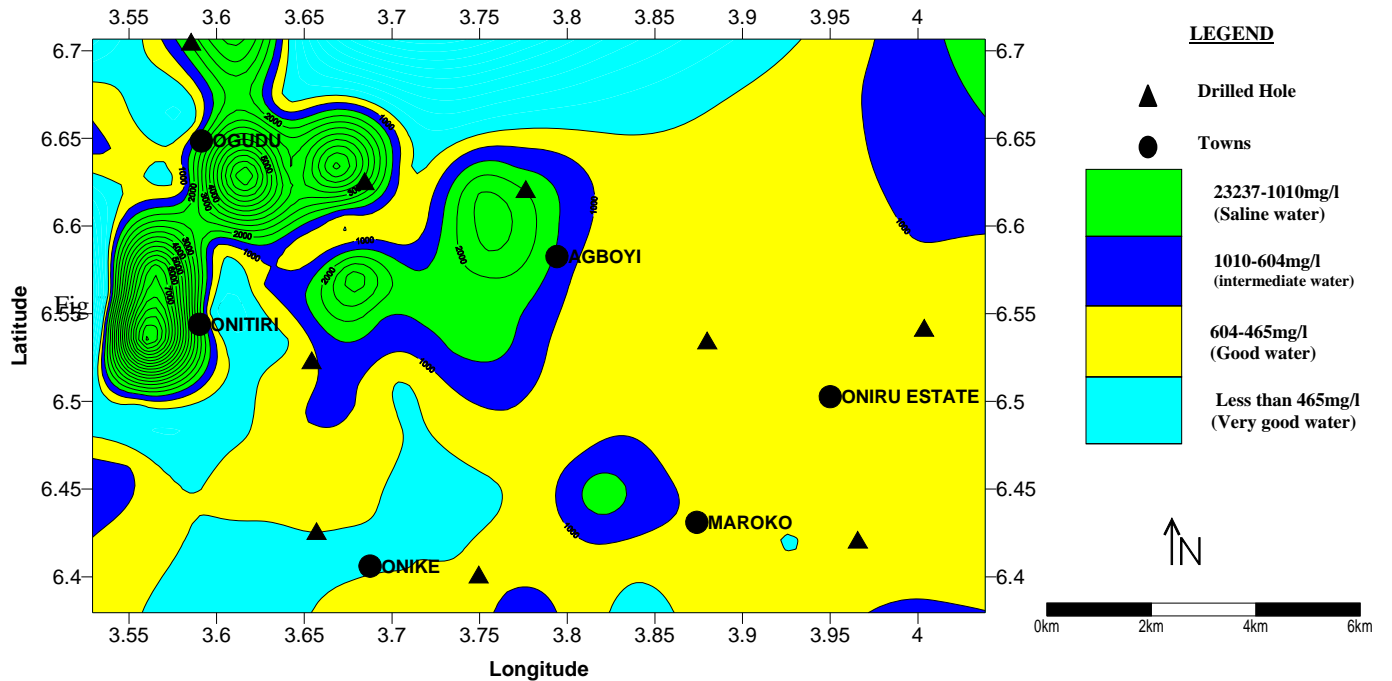


Fig 8: Morphology of subsurface TDS for layer III. Contour interval is 50 mg/l

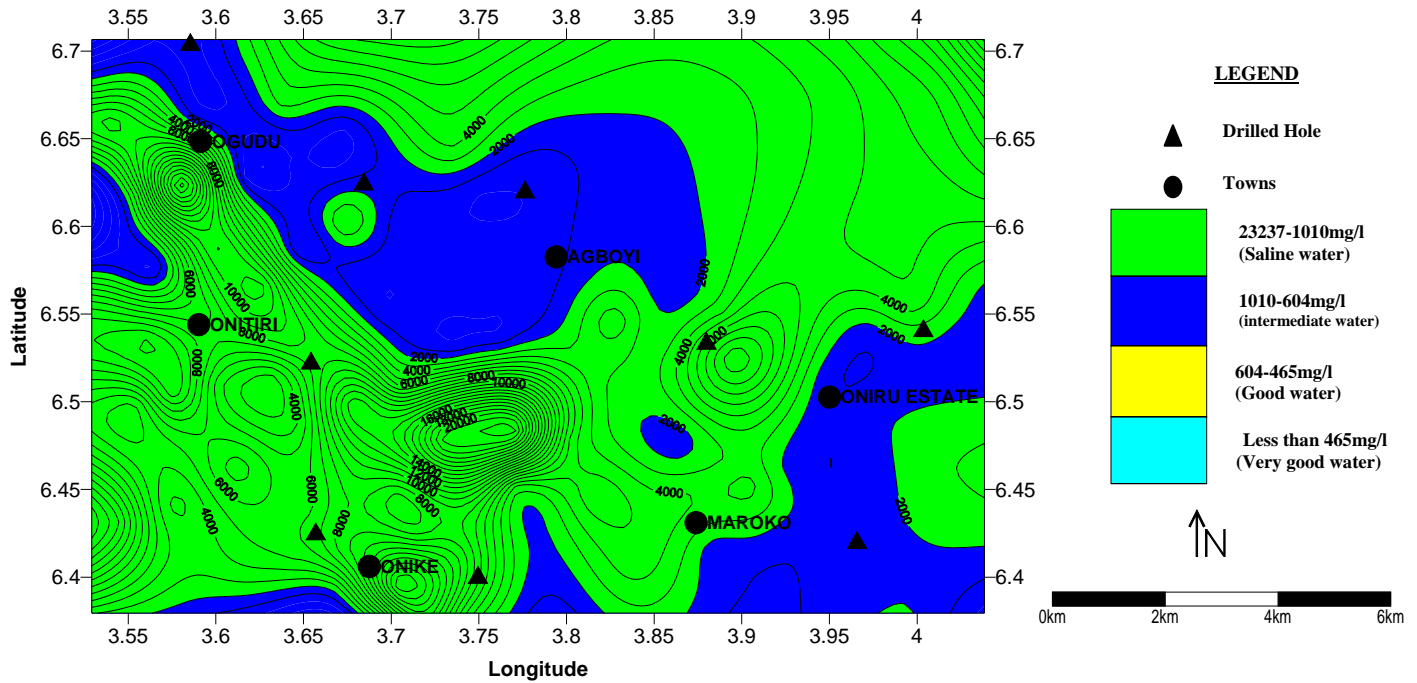


Fig 9: Morphology of subsurface TDS for layer III. Contour interval is 50mg/l

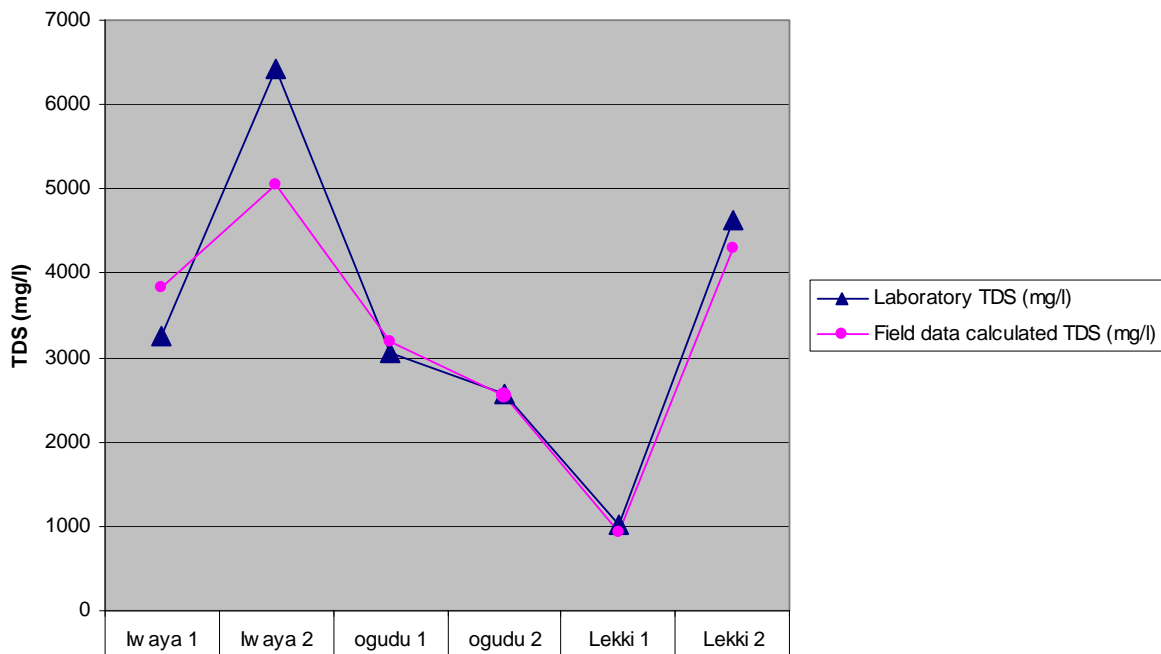


Fig 10: Comparison of Laboratory analysis of total dissolved solids (TDS) and TDS values inferred from resistivity data

Table 1: Aquifer properties and calculated total dissolved solids (TDS)

VES Station No.	No. of Layers	Resistivity of Layers (Ohm-m)				Conductivity of layers (Ohm ⁻¹ .m ⁻¹)				Thickness of layers (m)			Calculated TDS content of layers (mg/l)			
		P ₁	P ₂	P ₃	P ₄	σ ₁	σ ₂	σ ₃	σ ₄	T ₁	T ₂	T ₃	Cl ₁	Cl ₂	Cl ₃	Cl ₄
01	4	151.1	184.7	130.7	12.1	0.00662	0.00541	0.00768	0.08265	1.1	4.5	40.4	307	251	355	3837
02	4	201.4	150.1	131.8	9.2	0.00497	0.00666	0.00759	0.10870	1.0	6.5	59.0	230	309	352	5046
03	4	100.1	150.3	94.2	16.1	0.00999	0.00665	0.01062	0.06211	1.2	4.8	67.8	464	309	493	2883
04	4	80.4	126.2	70.5	8.2	0.00244	0.00792	0.01418	0.12195	1.4	2.6	41.4	577	368	658	5661
05	4	480.6	393.2	112.7	5.4	0.00208	0.00254	0.00887	0.18519	1.1	3.8	46.2	97	118	412	8597
06	4	94.1	128.6	86.6	2.8	0.01063	0.00778	0.01155	0.35714	1.0	6.4	56.2	493	361	536	16579
07	4	180.4	240.2	65.8	5.6	0.00554	0.00416	0.01520	0.17857	1.2	10.6	44.1	257	193	705	8290
08	4	201.7	162.6	70.4	6.8	0.00496	0.00615	0.01421	0.14706	1.1	11.6	30.2	230	285	659	6827
09	4	198.4	172.4	45.2	15.4	0.00504	0.00580	0.02212	0.06494	1.0	2.8	42.6	234	269	1027	3014
10	4	108.2	206.4	89.2	4.8	0.00924	0.00485	0.01121	0.20833	1.1	3.6	50.4	429	225	520	9671
11	4	102.4	174.6	94.8	6.2	0.00977	0.00573	0.01055	0.16129	1.2	6.8	49.6	453	266	490	7487
12	4	184.3	196.3	66.4	5.4	0.00543	0.00509	0.01506	0.18519	1.1	10.1	40.4	252	236	699	8597
13	4	204.6	321.4	114.6	6.8	0.00489	0.00311	0.00873	0.14706	1.0	8.9	56.4	227	144	405	6827
14	4	184.2	160.1	86.4	2.2	0.00543	0.00625	0.01157	0.45455	1.0	6.8	50.4	252	290	537	21101
15	4	601.4	286.4	54.6	2.1	0.00166	0.00349	0.01832	0.47619	1.1	17.8	104.6	77	162	850	22106
16	4	186.6	164.4	84.2	11.4	0.00540	0.00608	0.01188	0.08772	1.2	6.8	64.5	249	282	551	4072
17	4	340.2	234.2	65.4	7.8	0.00294	0.00427	0.01529	0.12821	1.1	6.2	40.6	136	198	710	5952
18	4	100.0	74.6	26.4	8.1	0.0010	0.01341	0.03788	0.12346	1.0	8.4	69.4	464	622	1758	5731
19	4	204.7	128.6	46.8	15.1	0.00488	0.00778	0.02137	0.06623	1.1	6.8	64.8	227	361	992	3074
20	4	305.6	264.5	78.6	10.4	0.00327	0.00378	0.01272	0.09615	1.2	10.8	80.4	152	176	591	4464

Cl₁ = Total dissolved solids for layer 1

ρ₁ = Resistivity of layer 1

T₁ = Thickness of layer 1

VES = Vertical Electrical Sounding

σ₁ = Conductivity of layer 1

Table2: Geochemical analysis of water samples from selected abandoned boreholes within the study area

Location	Appearance	Colour	Turbidity	Acidity	TDS (mg/l)	Iron (mg/l)	Nitrate (mg/l)	Phosphate (mg/l)
Iwaya (2)	Clear	10	4	1.5	3050	0.6	-	-
Iwaya (1)	Clear	8	3	1.2	2560	0.4	-	-
Ogudu (1)	Clear	5	6	0.8	1020	0.3	-	-
Ogudu (2)	Clear	6	5	2.4	4628	0.12	-	-
Lekki (1)	Clear	5	4	1.4	6426	0.4	-	-
Lekki (2)	Clear	8	3	0.6	3248	0.3	-	-

Table 3: Comparison of laboratory analysed Total Dissolved Solids (TDS) and Field data calculated TDS values

VES No.	Location	Laboratory TDS (mg/l)	Field data calculated TDS (mg/l)
01	Iwaya (2)	3248	3837
02	Iwaya (1)	6426	5046
53	Ogudu (1)	3050	3180
67	Ogudu (2)	2560	2551
80	Lekki (1)	1020	921
97	Lekki (2)	4628	4298

Table 4: Upper limits of TDS values for agricultural uses

Animal	Upper limit of TDS (mg/l)
Poultry	2860
Pigs	4290
Horses	6435
Cattle (dairy)	7150
Cattle (beef)	10000
Adult sheep	12900

Source: WHO, 1993

Table5: Upper limits of TDS values for industry

Industry	Upper limit of TDS (mg/l)
Boiler feed	3000-500
Brewing and distilling	1000-500
Carbonated beverages	850
Plastics (clear)	200
Textiles	200
Confectionery	100
High grade light paper	200

Source: WHO,1993

Table 6 Corresponding resistivity of upper limits of TDS values for agricultural and industrial purposes

Items	Upper limit of TDS (mg/l)	Corresponding resistivity (Ωm)
Animals		
Poultry	2860	16.2
Pigs	4290	10.8
Horses	6435	7.2
Cattle (dairy)	7150	6.5
Cattle (beef)	10000	4.6
Adult sheep	12900	3.6

Items	Upper limit of TDS (mg/l)	Corresponding resistivity (Ωm)
Industry		
Boiler feed	3000-500	15.5-92
Brewing and distilling	1000-500	46.5-92
Carbonated beverages	850	54.7
Plastics (clear)	200	232.3
Textiles	200	232.3
Confectionery	100	464.6
High grade light paper	200	232.3

Table7: Proposed Resistivity Model for water and sediment within the surveyed area.

Resistivity (Ohm-m)	TDS content (mg/l)	Inferred sediments	Interpretation
2-46	23237-1010	Saturated fine to medium sand or saturated clayey sand	Saline water
46-77	1010-604	Saturated sand or sandy clay	Intermediate quality freshwater
77-100	604-465	Medium to coarse sand, or sandy clay	Good quality freshwater
Over 100	Less than 465	Coarse sand	Very good quality water.

Conclusion

The relevance of this work is in the ability to calculate the total dissolved solid (TDS) from electrical resistivity data of each saturated layer and using same alongside conductivity contrast to predict and monitor the degree of total salinity in groundwater within the study area. Good prospects exist for freshwater development in the study area where the TDS values range from 604-465 *mg/l*. The interpretation of TDS values from resistivity measurements is in good agreement with the TDS values obtained from the laboratory measurements.

The TDS values inferred from resistivity data therefore gives reasonable and reliable information that can be used to understand the subsurface total salinity in groundwater exploration.

References

- Adamson, J. K. and Hornung, M. (1990). The effect of clear felling a sitka spruce (*pica stitchensis*) plantation on solute concentration in drainage waters. *J. Hydrology*, 116, 297-298.
- Brian, J. Boman, P., Chris, W. and Esa, A. (2002). Understanding water quality parameter for citrus irrigation and drainage system. Circular 1406, Florida Cooperative Extension Services, Institute of Food and Agricultural Science, University of Florida.
- Greenberg, A. E., Connors, J. J. and Jenkins, D. (1980). Standard methods for the examination of water and waste water. American Public Health Association, Washington, DC 20006, 1134 pp.
- Jeje, L. K. (1983). Aspects of geomorphology in Nigeria. In: A Geography of Nigeria. (eds. Oguntoyinbo, J. S., Areola, O. O. and Filani, M.) Heinemann Educational Books, Nigeria, 17-44pp.
- Jones, H. A. and Hockey, R. D. (1964). The geology of part of Southwestern Nigeria. *Geol. Surv. Nig. Bull.* 31.
- Kampsax and Sshwed (1997). Hydrogeology of Lagos Metropolis, a report submitted to the Ministry of Works and Planning (unpublished).
- Fatoba, J. O. and Olorunfemi, M. O. (2004). Subsurface sequence delineation and salinewater mapping of Lagos State, Southwestern Nigeria. *Global J. Geol. Scs.*, 111-123.
- Oyedele, K. F. and Meshida, E. A. (2006). Groundwater pollution studies in a coastal environment using surface resistivity method. A case study of Lekki, Lagos, Nigeria. *Global J. Pure & Appl. Scs*, 4(1), 1-6.
- RESIX-IP (1988). User's Manual. Interpex. Golden Co., USA.
- Roberto, B., Enrico, G., Federica, A. and Giorgio, G. (2003). Geophysical approach to the environmental study of a coastal plain. *Geophys.*, 68(5), 1446-1458.
- Rofe, K. and Lapworth, S. (1987). Hydrogeological investigation of Lagos State. Report submitted to Lagos State Water Corporation, Vol. 2, 86 pp.

1/27/2009

Evaluation of Sea water Intrusion in Freshwater Aquifers in a Lagoon Coast: A Case Study of the University of Lagos Lagoon, Akoka, Nigeria

K.F.Oyedele, E.I. Momoh

Department of Physics, (Geophysics Option), University of Lagos, Akoka, Lagos, Nigeria

Correspondence: kayodeunilag@yahoo.com

ABSTRACT: A geophysical technique has been employed to investigate seawater intrusion into freshwater aquifers in the coastal environment of the Lagos lagoon at the University of Lagos campus, Akoka, south-western Nigeria. Electrical resistivity method employing the Schlumberger array was used to acquire data for six vertical electrical soundings to investigate the vertical extent of seawater intrusion. The study revealed that the subsurface in contact with the lagoon was invaded by saline oceanic seawater. The Schlumberger electrode array which utilized current electrode half spacing from 1m to 500m was used to acquire both resistivity and induced polarization data in the proximity of the Lagos lagoon. Typical curve types reported for coastal areas such as the KQ, KQQ, and HKQ were observed in the investigated area and 4-6 geoelectric layers were delineated at an average depth of 71m. The subsurface lithology comprised of fine through medium grained sand to coarse sand intercalated in most cases with sandy clay and clayey sand. The resistivity of the intruded saline water was found to range between 1.8-37.2 Ωm at a depth interval of 0.7-79 m and the thickness of saline layers was found to be greater in the proximity of the coastline. The result of the investigation revealed that even under non-pumping conditions, the study area suffers from acute saline water intrusion and could be aggravated if there is groundwater abstraction. Ways to check the seawater intrusion problem through artificial recharge have been proposed in the study. [New York Science Journal. 2009;2(3):32-42] (ISSN: 1554-0200).

Keywords: Geoelectric sections, resistivity, seawater intrusion.

1. Introduction

Over time, there has been heavy reliance on groundwater resources to supplement surface freshwater supplies for use in domestic, industrial and agricultural requirements. Most times, however, groundwater resources are preferable to surface water resources on the basis of easier protection from pollution and better dependability during drought periods. It has also been found that groundwater supplies are more economic in purification aspects than alternative water supplies, specifically surface water resources.

Coastal sedimentary basins the world over have been inundated by saline oceanic seawater intrusion which leads to the invasion of wells drilled to the subsurface to yield freshwater by saline water, and Nigeria has not been an exception. Saltwater intrusion in coastal aquifers in Nigeria have been a source of public grievance as several wells drilled to the groundwater table were abandoned only a few months after due to saline water intrusion. Even in some areas, freshwater supplies from groundwater sources have been impossible due to saline water dominating aquifers. Saltwater intrusion is a natural process that occurs in virtually all coastal aquifers, it is not only a national phenomenon, but a global crisis.

In characterizing the extent of this occurrence, attempted studies have been directed particularly to coastal areas in contact with seas, but rather few studies have been conducted to evaluate the possibility of the occurrence via a lagoon. Even most studies in this regard attribute the seawater as being relict and neglect the obvious impact of the saline water bodies. With a maritime area of about 46,500 km² and a coastline of 853km parallel to the Atlantic ocean, Lagos, is essentially a maritime state backed up by numerous rivers, lakes, creeks, swamps and lagoons; in an attempt to evaluate the possibility of seawater intrusion to the subsurface via the lagoon, this study was conducted.

The investigation of seawater intrusion in freshwater aquifers has been based on geophysical techniques especially the electrical resistivity and electromagnetic methods which relies on resistivity contrasts as the seawater intruded zone is approached, (Goldman *et al.*, 1989; Fitterman and Deszcz-Pan, 2001; Kontar and Ozorovich, 2006; Khalil, 2006; Al-sayed and El-Qady, 2007); their studies were carried out in the proximity of seas. The presence of seawater causes groundwater to be considerably saline, hence the aquifer resistivity is reduced considerably, and the resistivity method can delineate the boundaries of the body of saline water. The fact that a resistivity contrast exists at the interface between fresh and saline water is sharp, the resistivity method has proved useful.

A geochemical study can also be used to determine the possibility of seawater intrusion and this has been used by Lee and Song, 2007. However, for enhanced results, a combination of geophysical and geochemical analysis have proved useful, (Hwang *et al.*, 2004).

Oyedele (2001) combined a geophysical and geochemical analyses to show the presence of seawater intrusion in Victoria Island and Iwaya in Lagos state, south-western Nigeria. He suggested that the freshwater/saltwater interface (FWSWI) is relatively shallow and water withdrawals are from depths close to the FWSWI. And he contends that excessive groundwater withdrawals can increase the incidence of seawater intrusion.

Adepelumi *et al.* (2008) in an attempt to demarcate possible areas for groundwater development in the Lekki area of Lagos state, obtained resistivity results which revealed a dominant trend of decreasing resistivity with depth, indicating an increase in salinity with depth. They however traced the presence of the salinity to excessive groundwater pumping and the reduction of groundwater gradients. They established the inherent presence of saline water in the subsurface of their area of investigation as being trapped during the transgressive, and the regressive movement of the ancient sea during the quaternary times when some sediments were contemporaneously deposited under marine condition. They inferred that the saline water found at a shallow depth (10-30 m) was probably trapped during marine transgression and/or it migrated from depth by differential pressure-gradient. One can infer the source of saline water in the subsurface as connate according to the referenced report. They, however, did not particularly cite the influence of the lagoon which surrounded their study area. Their analysis is based on Kingston *et al* (1983) who suggested that prior to the fluctuation of the sea level in Lagos area, series of miogeoclinal depressions were formed at the edge of the rifting Atlantic Ocean. These depression zones were later filled with seawater where the sediments were deposited. It can be inferred that the saltwater was trapped during the period of marine deposition. The possibility of seawater intrusion by the tidal movement of saline seawater presently was not examined. And this study attempts to bridge that gap.

The Lagos lagoon coast bordering the University of Lagos to the east on the lagoon front overlooking the university guest houses, senate building, University library, human resources development board offices and the faculty of engineering are the focus of the study. It lies on latitude 6°30'40" N and 3°24'52" E longitude. It lies on marshland of vast mangrove and freshwater swamps, surrounding a small and much dissected table land consisting of freshwater swamp forest, mangrove swamp forest, sandy plain vegetation and rainforest vegetation (Ayolabi, 2004). The Lagos lagoon borders the university campus to the east and south. Bariga borders it to the north while Yaba lies towards the west. A canal runs along almost the whole of the western stretch of the university, while a marsh which has an open connection to the lagoon encompasses the whole of the northern stretch of the University, linking up with the canal in the west.

2. Hydrogeologic Setting of the Study Area

The study area is situated in Lagos State (figure 1) which is found within the Benin basin. The geology has no basement outcrop. It lies on the longitude 3°E and latitude 7°N with alternate wet and dry seasons. The Benin basin extends almost from Accra in Ghana, through the Republics of Togo and Benin to Nigeria where it separated from the Niger- Delta basin by Okitipupa ridge

(Ondo state) at the hinge of the Benin flank. The bottom of the sedimentary basin in the Benin basin consists of unfossiliferous sandstones and gravels weathered from the underlying Precambrian basement. On top of these are marine shales, sandstones and limestones of Albian to santonian ages.

The area of investigation is low-lying with some depressions observed which are prone to flooding, as they are apparently below the surface of the lagoon.

The surface geology is made up of the Benin formation (Miocene to Recent) and the recent littoral alluvial deposits. The Benin formation consists of thick bodies of yellowish (ferruginous) and white sands (Jones and Hockey, 1964). It is friable, poorly sorted with intercalation of shale, clay lenses and sandy clay with lignite. The formation is overlain in many places by considerable thickness of red earth composed of iron-stained regolith formed by weathering and ferruginization of the rock (Onyeagocha, 1980). Multi-layer aquifers have been classified by Longe *et al.* (1987) into three types-the first encountered at a depth of 38m of average thickness of 8m and is not a major source of water supply and stands the risk of pollution because of its nearness to the surface. The aquifer probably belongs to the recent littoral/alluvial depth of 30m to 120m below sea level near the coast, it consists of an alternating sequence of sands and clay. The aquifer probably belongs to the continental Ilaro formation which is described as a sequence of predominantly coarse sandy estuarine deltaic and continental beds. The third aquifer is made up of alternating sequences in shape. This aquifer is the most productive and exploited region. It occurs between depths of 30-100 m below sea level in inland areas and 120-270 m near the coast. The thickness varies between 10 and 35 m. The aquifer most likely forms part of the Ilaro formation.

In the Benin basin, salt water intrusion into recent sediments aquifers occurs beneath a freshwater lens in a belt stretching from the coastline to a distance of 5km in some places. Saltwater intrusion has also been found to occur in the confined aquifers of the coastal plain sands in a zone stretching from Apapa to Lekki within Lagos metropolis (Oteri and Atolagbe, 2003).

Lagoons are common features on the Guinea coast of West Africa. The Lagos lagoon with a surface area of 6354.798km² is open, tidal and brackish, and is the largest of the eight lagoons in southwestern Nigeria. The Lagos lagoon, a water body in the heart of the metropolis, cuts across the southern part of the metropolis, linking the Atlantic Ocean (in the west and south) and the Lekki lagoon (in the east). The Lagos lagoon consists of three main segments, Lagos harbour, the metropolitan and Epe division segment.

The bottom water of the lagoon has high temperatures which were relatively constant throughout the year. The temperatures varied between 32.7°C in December 2002 at the entrance of the Ogun river near Ikorodu and 27°C in 2003. During the rains (April to November) the influx of river water and heavy cloud cover in the sky resulted in a gradual fall of the temperatures to a minimum of 26°C.

There is differential salinity in the lagoon due to the effect of the Atlantic Ocean. The bottom deposits ranged from coarse shelly sand around the mouth of Lagos harbour through various grades of muddy sand to mud. Sandy mud or muddy deposits occurred in the central areas with muddy sand or sand being attributed to the fast water currents in the area. The seabed in the metropolitan areas is relatively higher and increases towards the Epe segment of the lagoon. The seabed has been distorted by semi and large scale mining especially towards the Ikorodu area of the lagoon.

All the water bodies dominating Lagos State, the Lagos lagoon inclusive, others have a common connection to the Atlantic Ocean via the commadore channel (see figure 1). Thus some of the hydrologic conditions prevailing in the Gulf of Guinea are reflected to some extent in the Lagos lagoon, going by the definition put forward earlier.

The entire Gulf of Guinea is highly stratified with a thin surface layer of fresh tropical water overlying high salinity subtropical water (because of density difference). An additional contribution of saline water comes from subducted subtropical water from the Atlantic Ocean.

This saline water communicates with the Lagos lagoon via the Commodore channel largely dependent on the direction of the tides.

3. Data Acquisition and Processing

In this work, a total of six VES points were occupied along selected traverses namely AA', BB' and CC'. The traverses AA' and CC' were taken parallel to the shoreline of the lagoon stretching westward, while the traverse BB' was taken perpendicular to the shoreline. The Schlumberger electrode array was utilized for the data acquisition which was done with the ABEM terrameter SAS 1000. The current electrode half spacing for the survey ranged from 1 to 500m in successive steps.

The field data were curve matched using the conventional curve matching technique and the layer parameters obtained were used as an input model for a fast computer iteration and modelling software known as RESIST[®]. The application of this software is a standard procedure for obtaining a fairly accurate estimate of the subsurface resistivity distribution.

The addition of Induced Polarization (IP) data to a resistivity investigation improves the analysis of resistivity data in three ways: (1).Some of the ambiguities encountered in resolving thin stratigraphic layers while modeling electrical resistivity data can be reduced by the analysis of IP data, (2).IP data can be used to distinguish geologic layers which do not respond well to an electrical resistivity survey; and (3).The measurement of another physical parameter (electrical chargeability) can be used to enhance a hydrogeologic interpretation such as discriminating equally electrically conductive targets such as saline, electrolytic or metallic-ion contaminant plumes from clay layers.

The interpreted data were contoured in order to observe the resistivity, thickness, and depth of saline layers and the freshwater/saltwater interface (FWSWI). The SURFER[®] 8 software was used in producing the maps.

4. Discussion of Results

The analysis of resistivity data revealed the presence of four to five geoelectric layers along profiles AA' and BB' while six geoelectric layers characterized profile CC'. Typical curve types characteristic of saline water intruded zones were observed such as AKQ, KQH, KQ and KQQ. The curves were found to descend gently indicating a conductivity decrease which can be explained in terms of the seawater intrusion into subsurface formations. The descending segment of the VES curves are characterized by a steeply low resistivity zone (figure 2). The IP curves were interpreted thus: the electrode-depth ratio was used to estimate the depths at various electrode spacings. Chargeabilities of < 50msec were interpreted as sand, while those >50msec or negative were interpreted as clay; fluctuations in the IP profile was not unconnected with the clay and sand mixture. These were interpreted as sandy clay or clayey sand depending on the degree of fluctuation.

The correlation of the resistivity, IP (figure 3) and available borehole log in the study area revealed that the topsoil along traverse AA' is made up of fine to medium sand with characteristically low resistivity attributed to the overflow of saline oceanic seawater via the lagoon. The resistivity ranges between 11.5 Ω m to 43.7 Ω m with a thickness ranging from 0.7 m to 1.7 m. This layer is underlain by a medium sand bed which is the second geoelectric layer of resistivity 3.4 Ω m to 74.9 Ω m, and thickness of 2.2 m to 9.9 m. The third geoelectric layer beneath this traverse is a continuous sandy clay formation which grades into the fourth geoelectric layer beneath VES 1, 2, 3 and 4; and into the fifth geoelectric layer beneath VES 2. These layers are considered to suffer from acute seawater ingress, with formation resistivity of 7 Ω m to 42.10 Ω m. The thickness of this layer ranges from 12 m to 70 m. (See figure 4). The fifth layer beneath VES 4 is a high resistivity coarse sand or clayey sand formation.

The geoelectric section along traverse BB' consists of VES 5. The topsoil is the first geoelectric layer with formation resistivity >100 Ω m and is made up of coarse sand. The second

geolectric layer, even though it is a relatively good freshwater aquifer; apart from its proximity to the surface and consequently, exposure to pollution, its thickness of 0.9 m does not favour exploitation. The third geoelectric layer can be considered as the zone of rapidly mixing fresh and saline water. With a formation resistivity of 64.1 Ωm and thickness of 5.8m, it is comprised of medium sand/ sandy clay. The fourth geoelectric layer suffers from acute saline water intrusion due to the presence of seawater. With a resistivity of 1.8 Ωm and thickness of 12.8 m, it is composed of sandy clay. It is underlain by a coarse sand/clayey sand freshwater aquifer zone of unknown thickness and resistivity of 210.7 Ωm .

The geoelectric section along traverse CC' consists of VES 6. The topsoil is sand formation with a resistivity of 47.9 Ωm and 0.8 m thick. The second and third geoelectric layers which are coarse sand beds are freshwater bearing aquifers saturated by very good quality freshwater. The formation resistivities are 260.7 Ωm and 309.9 Ωm , and 1.2 m and 6 m thick respectively. The fourth geoelectric layer is composed clayey sand, saturated with good quality water. The resistivity of this layer is 89.7 Ωm and it is 29.9m thick. The fifth geoelectric layer has a resistivity of 8 Ωm , and 34 m thick. The lithology which is composed of saline-water saturated clayey formation is underlain by coarse sand bed which bears very good quality water. This layer has a resistivity of 532.5 Ωm .

The interpreted data were subjected to processing using the SURFER 8 Golden software to produce the various contour maps. These show the lateral and horizontal extent of saline oceanic seawater intrusion. The study area shows evidence of subsurface formations by saline water intrusion. The depth of penetration of saline water intrusion increased from the lagoon coastline inwards.

Maps of isoresistivity surfaces for estimating depth to saline and freshwater zones at the locations occupied are shown in the figures below (figure 5a-f). The observed trend is that the thickness of the saline water formation is increasing towards the coast. In addition, the depth to the saline water zone is found to be relatively shallow near the coast compared to inland areas. The depth to the FWSWI varies from about 72 m near the coast to about 20m in inland areas. The resistivity of the freshwater aquifer is found to decrease as distance from the coast increases.

The isoresistivity contour map for saline water surfaces indicates that the resistivity of saline water tends to decrease towards the coast. Higher resistivity values are observed further away from the coast, i.e. at Tafawa Balewa way. It is expected however that this resistivity grades gradually through intermediate water to good quality water as distance from the coast keeps increasing. And the isoresistivity map for freshwater shows that reasonably good aquifers containing very good quality water can be found far away from the coastline. This is attributable to the high resistivity values which are observed as the distance from the coastline increases.

The depth to saline water surfaces is shallower in the proximity of the lagoon. With an increase in the distance from the coastline, the depth to saline water surfaces increases to about > 22 m. The traverse taken at Tafawa Balewa way was at a higher elevation than those occupied at the Lagoon Front and Oduduwa Drive in which the water and ground level were approximately the same. The explanation then was that the salts are transported when there is overflow, moved further by wind action, settle gravitationally and are pushed down the subsurface by meteoric water. In the case of Tafawa Balewa way, the saline water hits the wall of the adjoining ground carrying some sediments, salts inclusive. Further lagoon water hitting the walls transports the salts further until they meet an impermeable layer which traps the salts.

The thicknesses of saline water zones are greater in the proximity of the lagoon. Less thick beds are found away from the lagoon. The thickness of saline water intrusion is lowest at Oduduwa Drive because it is dominated by freshwater aquifers and the most we can find is intermediate water of rapidly mixing fresh and saline water.

The salinity problem may exist due to upward movement of water and salts from groundwater. For coastal aquifers, the influence of seas, oceans, and lagoons are predominant. Since it is a saline problem, the validity of including lagoons in the picture have been emphasized.

The salt enrichment process of the subsurface is spread over to thousands of millions years, during which the determining parameters of rainfall, hydrology and other climatic factors have not remained constant. Much as we do not want to envisage relict seawater, whether or not it occurs, or the salinity can be attributed to saline surface water intrusion shall become apparent at the end of this treatise.

One of the potential causes of subsurface salinity which does not require too geologically long a time, has been reported by Achari *et al.* (2005) was the inundation of an entire barrier by the surface influx of seawater where the tsunami impact on groundwater quality was assessed. They proffered an explanation for the process that led to groundwater salinization thus: when seawater ingressed over the surface, by waves with heights ranging from 4 to 7 m, it carried along some dissolved salts, which were lodged in the soil. The salts brought by the mighty waves sink into the soil and with the first rains of the year, the absorbed salts leach down to the groundwater aquifer and contaminated it. When the dry summer months advance, evaporation causes the salt to accumulate in the subsurface, pending recharge (by the sea, which brings in more salts anyway). Rainfall recharge pushes the saltwater, further down in an attempt to establish hydrodynamic equilibrium capillary rise in rainless months push the salts up. In all, the soil salinity is significant for a considerably long time and is a continuous process.

Table 1: Summary of Interpretation

VES No	Geoelectric Layers	Resistivity (Ω m)	Thickness (m)	Depth (m)	Curve Type	Probable Lithology	Inferred Interpretation
1	1	37.50	1.2	1.2	KQ -	Fine to medium sand	Topsoil
	2	58.30	9.9	11.1		Medium sand	Intermediate quality water
	3	33.33	101.0	112.2		Sandy clay	Saline water
	4	9.00	-	-		Sandy clay	Saline water
2	1	41.50	1.7	1.7	KQQ -	Fine to medium sand	Topsoil
	2	74.90	6.5	8.2		Medium sand	Intermediate quality water
	3	37.20	12.5	20.8		Sandy clay	Saline water
	4	34.50	58.4	79.2		Sandy clay	Saline water
	5	7.60	-	-		Sandy clay	Saline water
3	1	43.7	1.6	1.6	KQ -	Fine to medium sand	Topsoil
	2	56.9	9.1	10.7		Medium sand	Intermediate quality water
	3	42.1	59.2	69.9		Sandy clay	Saline water
	4	12.70	-	-		Sandy clay	Saline water
4	1	11.5	0.7	0.7	HKH -	Fine to medium sand	Topsoil
	2	3.6	2.2	2.8		Sandy clay	Saline water
	3	61.6	16.6	18.8		Medium sand/Sandy clay	Intermediate quality water
	4	7.0	52.4	71.2		Sandy clay	Saline water
	5	514.1	-	-		Coarse sand/ Clayey sand	Very good quality water
	1	101.00	0.7	0.7		Coarse sand	Topsoil
	2	131.60	0.9	1.6		Coarse sand	Very good quality water

5	3	64.1	5.8	7.4	KQH	Sandy clay	Intermediate quality water	
	4	1.8	12.8	20.2		-	Sandy clay	Seawater/ very saline water
	5	210.7	-	-			Coarse sand/ Clayey sand	Very good quality water
6	1	47.9	0.8	0.8	AKQH	Fine to medium sand	Topsoil	
	2	260.7	1.2	2.0		Coarse sand/ Clayey sand	Very good quality water	
	3	309.9	6.0	8.0		Coarse sand/ Clayey sand	Very good quality water	
	4	89.7	29.9	37.9		Clayey sand	Good quality water	
	5	8.0	34.0	71.9		Clay	Saline water	
	6	532.5	-	-		Coarse sand/ Clayey sand	Very good quality water	

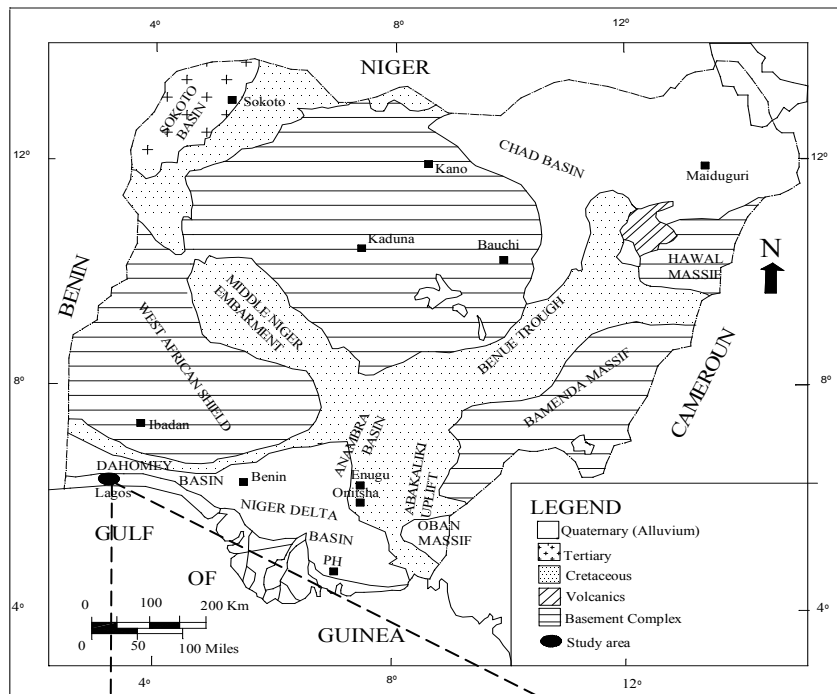
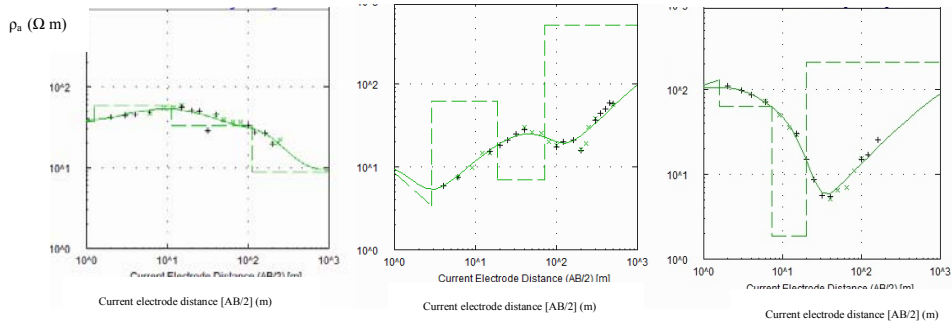


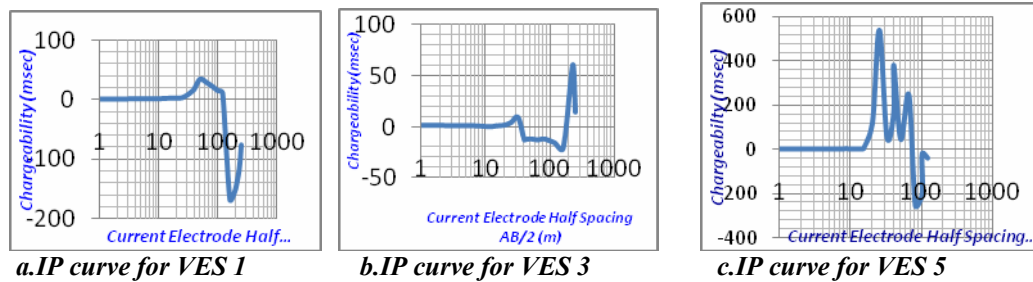


Figure 1: Geological map of Nigeria showing the location of the study area. Inset is the image of Lagos state showing the distribution of lagoon water up to the study area.



a. Iterated curve for VES 1 b. Iterated curve for VES 4 c. Iterated curve for VES 5.

Figure 2a-c: Representative samples of computer iterated resistivity curves



a. IP curve for VES 1 b. IP curve for VES 3 c. IP curve for VES 5

Figure 3a-c: Representative samples of induced polarization curves.

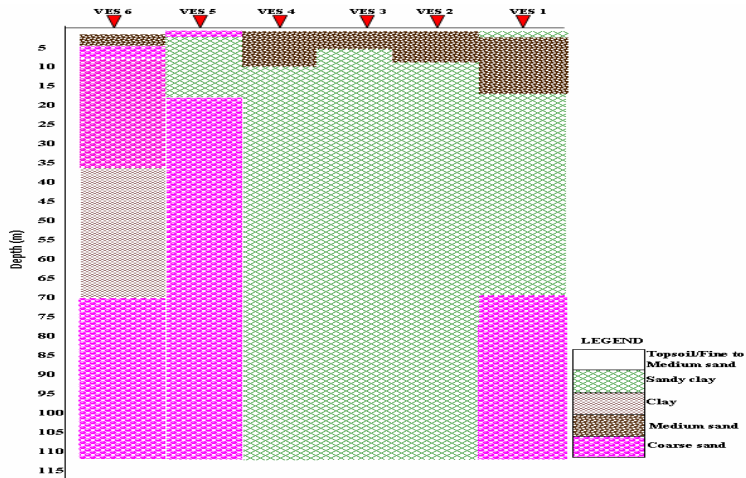
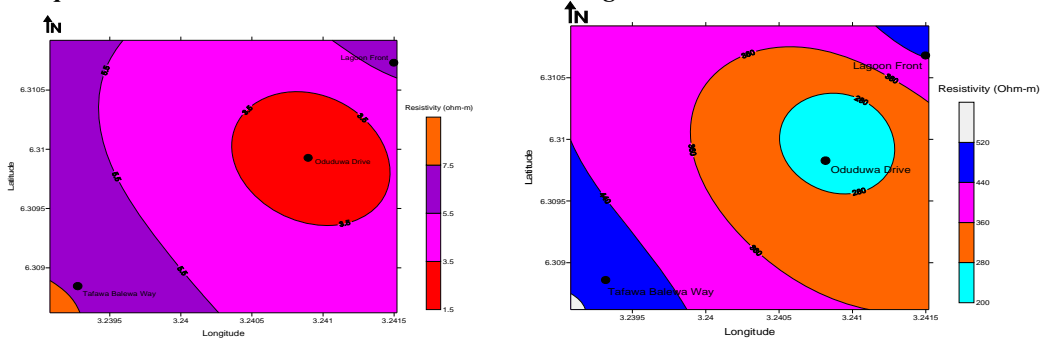
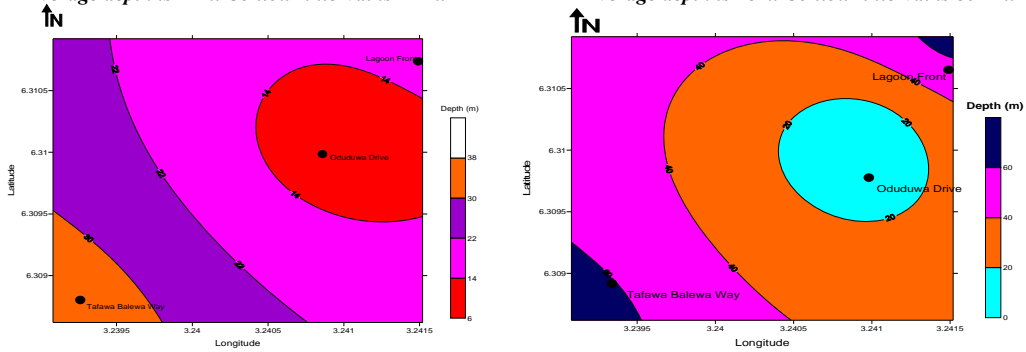


Figure 4: Subsurface conceptualisation of the study area inferred from the VES and IP interpretation correlated with the available borehole log.



a. Isoresistivity map for saline water horizon (2-46 Ω m). Average depth is 21m. Contour interval is 20 Ω m.

b. Isoresistivity map of freshwater aquifer. Average depth is 28m. Contour interval is 80 Ω m.



c. Depth to saline water isoresistivity surface. Contour interval is 8m.

d. Depth to freshwater aquifers. Contour interval is 20m.

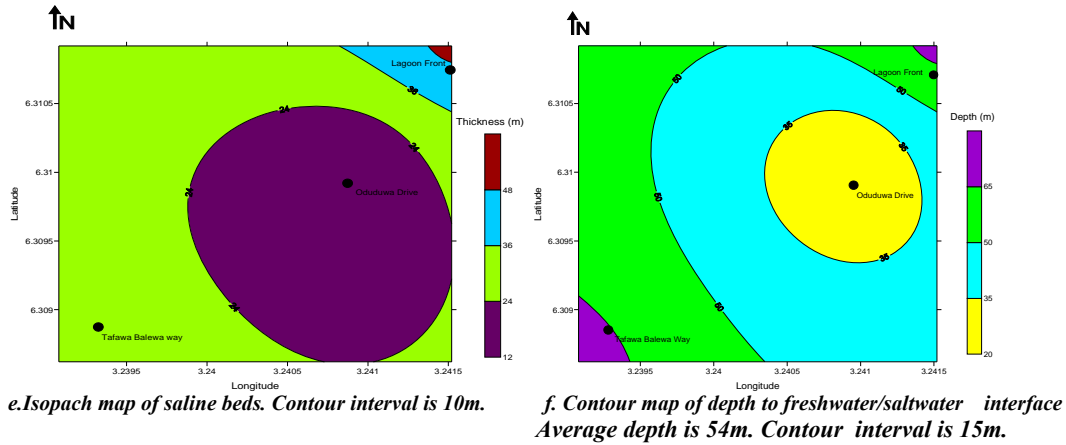


Figure 5a-f: Isoresistivity, isopach and depth maps of the study area.

5. Conclusion

In evaluating seawater intrusion into coastal aquifers of lagoonal environments, six vertical electrical sounding measurements were conducted at selected stations at the University of Lagos, Akoka; to acquire both resistivity and IP data. From the one dimensional interpretation of the acquired data, it was found that saline water intrusion which is characteristic of seawater penetrated the subsurface in contact with the lagoon. The depth of the intrusion increased as distance from the coastline increased. In addition, typical curve types which are characteristic of coastal Nigeria sedimentary basin such as the KQ, KQQ, KQH, HKQ and AKQH were observed in the study area.

The astonishing rapidity with which saline water inundates the subsurface has been elucidated and elaborated. The study shows that the area suffers from acute saline water intrusion. It also attempted to look at the origin of the salts as being due to the deposition of sediments during flow towards land areas and the influence of meteoric water which serves to push some of these sediments down the subsurface. The study however, is not a radical departure from the view that saline water found its way into the aquifers due to an upwelling of saline water, whose origin is connate. Infiltration ponds whose water are natural floodwaters can be used to recharge coastal aquifers so that the rate of withdrawal is balanced by the rate of freshwater recharge.

Seawater intrusion is a natural phenomenon in coastal aquifers. Whether we like it or not, it occurs. Ways in which this happens have been examined. However, it becomes problematic when man withdraws water close to coastal areas. So in attempting to minimize the problem, monitoring its expansion and retreat, a geophysical approach has been proposed.

References

1. **Achari, S.V., Jaison, C.A., Alex, P.M., Pradeepkumar, A., Seralathan, P. and Sreenath, G. (2005).** Tsunami: Impact on the Groundwater Quality on Allapad Coast, Kollam, Kerala. *In*, Chapter VII: Water Quality Assessment in the Tsunami Affected Coastal Areas of Kerala (No.SR/S4/Es-135-6.0/2005. Department of Science and Technology, Government of India, New Delhi, India.

2. **Adepelumi, A.A., Ako, B.D., Ajayi, T.R., Afolabi, O. and Omotoso, E. J. (2008).** Delineation of Saltwater Intrusion into the Freshwater Aquifer of Lekki Peninsula, Lagos, Nigeria. *J. Environ. Geol.*
3. **Al-Sayed, E.A. and El Qady, G. (2007).** Evaluation of Seawater Intrusion using the Electrical Resistivity sounding and the Transverse Electromagnetic Survey: case study at the Fan of Wadi Feiran, Sinai, Egypt. EGM 2007 International Workshop-Innovation in EM, Grav. and Mag. Methods: a new perspective for Exploration, Capi, Italy, April.15-18.
4. **Ayolabi, E.A. (2004).** Seismic Refraction Survey of University of Lagos, Nigerian and its Implication. *J. App. Sc.* **7(3)**: 4319-4327.
5. **Fitterman, D.V. and Deszcz-Pan, M. (2001).** Geophysical Mapping of Saltwater Intrusion in Everglades National Park. First International Conference on Saltwater Intrusion and Coastal Aquifers Monitoring, Modelling and Management, Morocco.
6. **Goldman, M., Gilad, D., Ronen, A. and Melloul, A. (1991).** Mapping of Seawater Intrusion into the Coastal Aquifer of Israel by the time Domain Electromagnetic Method. *J. Appl. Geophys.* **28(2)**: 153-174.
7. **Hwang, S., Shin, J., Park, I. and Lee, S. (2004).** Assessment of Seawater Intrusion Using Geophysical Well Logging and Electrical Soundings in a Coastal Aquifer, Youngkwang-gun, Korea. *Exp. Geophys.* **35**: 99-164.
8. **Jones, H.A., Hockey, R.D. (1964).** The Geology of Part of Southwestern Nigeria. *Geol. Surv. Nig. Bull* 31
9. **Khalil, M.H. (2006).** Geoelectric Resistivity sounding for Delineating Saltwater Intrusion in the Abu Zerima Area, West Smai, Egypt. *J. Geophys. Eng.* **3**: 243-251.
10. **Kingston, D.R., Dishroon, C.P., Williams, P.A., (1983).** Global Basin Classification System. *Am. Assoc. Pet. Geol.* **67**:2175-2193.
11. **Kontar, E.A. and Ozorovich, Y.R. (2006).** Geo-electromagnetic survey of the Fresh/saltwater Interface in the Coastal Southeastern Sicily, *Cont Shelf Res* **26**: 343-851.
12. **Lee, J.-Y., Song, S.H., (2007).** Groundwater Chemistry and Ionic Ratios in a Western Coastal Aquifer of Buan, Korea; Implication for Seawater Intrusion. *Geosci. Journ. Hyd.* **3**: 259-270.
13. **Longe, E.O., Malomo, S. and Olorunmiwo (1987).** Hydrogeology of the Lagos Metropolis. *J. of Afr. Earth Sc.* **6(2)**: 163-174.
14. **Onyeagocha, A.C. (1980).** Petrography and Depositional Environment of the Benin Formation. *J. Min. Geol.* **17**: 147-151.
15. **Oteri, A.U. and Atolagbe, F.P. (2003).** Saltwater Intrusion into Coastal Aquifers in Nigeria. Proceedings of the Second International Conference on Saltwater Intrusion and Coastal Aquifers –Monitoring, Modelling and management. Merida, Yucatan, Mexico, March 30 – April 2. pp 1-6.
16. **Oyedele, K.F. (2001).** Hydrogeophysical and Hydrogeochemical Investigation of Groundwater Quality in some parts of Lagos, Nigeria. *Afr. Journ. Env. Studies.* **2(1)**: 31-37.
17. **Oyedele, K.F. (2006).** Geoelectric Mapping of Saline water Intrusion into the Coastal Aquifers of Lagos, Nigeria. PhD. Thesis, Department of Physics (Geophysics Option), University of Lagos, Lagos, Nigeria.
18. **Oyedele, K.F. (2008).** Effectiveness of the Electrical Resistivity Methods in Coastal Hydrogeophysical studies. *J. Env. Hydr.* Vol 16, paper 16.

Model for Predicting the Initial Solution pH at Assumed Final pH and Leaching Time during Leaching of Iron Oxide Ore in Hydrogen Peroxide Solution

Chukwuka Ikechukwu Nwoye^{1*}, Paulinus Chukwudi Agu¹, Okechukwu Daniel Onukwuli²,
Joshua Oke Borode³, Christian Nwosu Mbah⁴

¹Department of Materials and Metallurgical Engineering, Federal University of Technology, Owerri, Nigeria.

²Department of Chemical Engineering, Nnamdi Azikiwe University, Awka, Nigeria.

³Department of Materials and Metallurgical Engineering, Federal University of Technology, Akure, Nigeria.

⁴Department of Materials and Metallurgical Engineering, Enugu State University of Science & Technology, Enugu, Nigeria.

chikeyn@yahoo.com

Abstract

Model for predicting the final solution pH at determined initial pH and leaching time during leaching of iron oxide ore in hydrogen peroxide solution has been derived. It was observed that the validity of the model is rooted in the mathematical expression; $(\ln t)^{1/2} = N(\beta^C/\alpha^C)$ where both sides of the relationship are approximately equal to 2. The model; $\beta = \text{Antilog}[0.2439\text{Log}(\alpha^{4.1}(\ln t)^{1/2}/3.6)]$ shows that the initial solution pH is dependent on the values of the final solution pH and leaching time. The respective positive or negative deviation of the model-predicted final pH from its corresponding experimental value was found to be less than 8%, which is quite within the acceptable deviation limit of experimental results depicting the validity of the model. [New York Science Journal.2009;2(3):43-48].(ISSN:1554-0200).

Keywords: Model, Initial Solution pH, Final pH, Hydrogen Peroxide, Iron Oxide Ore, Leaching.

1. Introduction

Nwoye [1] derived a model for the computational analysis of the solution temperature during leaching of iron oxide ore in hydrochloric acid solution. The model is expressed as

$$T = e^{(8.9055/\gamma)} \quad (1)$$

where

T= Solution temperature during leaching of iron oxide ore using hydrochloric acid.(⁰C)

N= 8.9055(pH coefficient for hydrochloric acid solution during leaching of iron oxide ore) determined in the experiment [1].

γ = Final pH of the leaching solution at the time t when the solution temperature is evaluated.

The model is dependent on the value of the final pH of the leaching solution which was found to also depend on the concentration of iron dissolved in the acid. The prevailed process conditions on which the validity of the model depended on include: initial pH 2.5, leaching time; 30 minutes, leaching temperature; 25⁰C, average ore grain size; 150 μ m and hydrochloric acid concentration at 0.1 mol/litre.

It has been reported [2] that phosphorus could be removed from Itakpe iron oxide ore through a leaching process using sulphuric acid solution. Chemical analysis carried out on the iron ore indicates that the percentage of phosphorus in the ore is about 1.18%, which from all indication is quite high and could cause embrittlement and other adverse effects on the service life of engineering materials made from such iron ore. This was the basis for the dephosphorization process carried out [2]. Phosphorus was removed (at a temperature of 25⁰C, average ore grain size; 150 μ m and initial leaching solution pH range 0.47-0.53) and then dissolved in the acid solution in the form of phosphorus oxide.

Nwoye et al [3] derived a model for predicting the concentration of dissolved iron during leaching of iron oxide ore in sulphuric acid solution. The model is stated as;

$$\%Fe = 0.35(\alpha/T)^3 \quad (2)$$

Where

T = Solution temperature at the time t, when the concentration of dissolved iron is evaluated.(⁰C)

0.35= (pH coefficient for iron dissolution in sulphuric acid solution during the leaching process) determined in the experiment [3].

α = Final pH of the leaching solution at the time t, when the concentration of dissolved iron is evaluated.

The model (formulated at conditions; leaching temperature of 25⁰C, initial solution pH 5.0 and average grain size; 150 μ m) is dependent of the final pH and temperature of the leaching solution. The model shows that the concentration of iron dissolved during the leaching process is directly proportional to the third power of the ratio of final leaching and temperature.

Lee et al. [4] reported that the leaching of 3g/L pure haematite (98.2% purity, 105-140 μ m size range) using 0.048-0.48M oxalic acid at 80-100⁰C passed through a maximum peak at pH 2.5. Dissolution of haematite was found [4] to be

slower than magnetite ($\text{FeO}\cdot\text{Fe}_2\text{O}_3$) and other hydrated iron oxide such as goethite ($\alpha\text{-FeOOH}$), lapidochrosite (γFeOOH) and iron hydroxide ($\text{Fe}(\text{OH})_3$).

The dissolution of iron oxide is believed to take place via a photo-electro chemical reduction process, involving a complicated mechanism of charge transfer between the predominant oxalate species, namely ferric oxalate $\text{Fe}(\text{C}_2\text{O}_4)_3^{3-}$, ferrous oxalate $\text{Fe}(\text{C}_2\text{O}_4)_2^{2-}$ acting also as an auto catalyst, and the oxalate ligand on the iron oxide surface [5].

The dissolution of iron oxides in oxalic acid was found to be very slow at temperatures within the range 25-60°C, but its rate increases rapidly above 90°C [6]. The dissolution rate also increases with increasing oxalate concentration at the constant pH values set within the optimum range of pH 2.5-3.0. At this optimum pH, the dissolution of fine pure haematite (Fe_2O_3) (105-140 μm) follows a diffusion-controlled shrinking core model [6].

Taxiarchour et al [7] reported that it took close to 40h to dissolve 80% of pure haematite slurry (97% purity, 0.022% w/v or 0.21% g/L Fe_2O_3) at pH 1. He stated that even at 90°C, it required close to 10h to achieve 95% dissolution of iron of the slurry at pH 1. They also dissolved iron using 0.1-0.5M oxalic acid (pH1-5) to dissolve iron from a 20% w/v slurry (83% of particle size in the range 0.18-0.35mm, containing 0.029% Fe_2O_3). The iron oxide concentration in the leach is equivalent to 0.058g/L Fe_2O_3 .

The speciation of Fe(III) oxalate and Fe(II) oxalate has been found [8] to be governed by pH and total oxalate concentration. For a having pH > 2.5 and an oxalate concentration higher than 0.1M, the most predominant Fe(III) complex ion existing is $\text{Fe}(\text{C}_2\text{O}_4)_3^{3-}$. At these conditions, (pH > 2.5 and an oxalate concentration higher than 0.1M) the predominant Fe(II) complex species is $\text{Fe}(\text{C}_2\text{O}_4)_2^{2-}$.

Nwoye [9] derived a model for quantitative analysis of dissolved iron in oxalic acid solution in relation to the final pH of the solution during leaching of iron oxide ore;

$$\gamma = 0.5 \left(\frac{K_1[\% \text{Fe}_2\text{O}_3] + K_2[\% \text{Fe}]}{[\% \text{Fe}][\% \text{Fe}_2\text{O}_3]} \right) \quad (3)$$

where

K_1 and K_2 = Dissolution constants of Fe and Fe_2O_3 respectively.

γ = pH of leaching solution after time t (mins.).

The values of the dissolution constants compared with those of % Fe and % Fe_2O_3 from the experiment [9] indicate clearly that the constants K_1 and K_2 are numerical equivalence of the chemical resistance to the dissolution of Fe and Fe_2O_3 (respectively) in oxalic acid solution. It was found that $K_1 \approx 2K_2$ indicating twice chemical resistance to the dissolution Fe compare to that of Fe_2O_3 . This expression agreed with the higher percentage of Fe_2O_3 dissolved compared to that of the corresponding Fe. The model also predicted the final pH of the leaching solution when the concentrations of Fe and Fe_2O_3 dissolved (at a temperature of 30°C and average ore grain size; 150 μm) are known.

Model has been derived [10] for predicting the concentration of phosphorus removed during leaching of iron oxide ore in oxalic acid solution. The model is expressed as;

$$P = \left(\frac{150.5}{\mu\alpha} \right) \quad (4)$$

Where

P = Concentration of phosphorus removed during the leaching process (mg/Kg)

(μ) = Weight input of iron oxide ore (g)

(α) = Final pH of the leaching solution at the time t when P is evaluated

150.5 = (pH coefficient for phosphorus dissolution in oxalic acid solution during the process) determined in the experiment [10].

The model [10] predicted the concentration of phosphorus removed, with high degree of precision being dependent on the final pH of the leaching solution and weight input of the iron oxide ore. It also shows that the concentration of phosphorus removed (at a temperature of 25°C, average ore grain size; 150 μm and initial leaching solution pH 5.5) is inversely proportional to the product of the final pH of the leaching solution and the weight input of the iron oxide ore.

Model for computational analysis of heat absorbed by hydrogen peroxide solution (relative to the weight of iron oxide ore added) has been derived [11]. The values of the heat absorbed Q as predicted by the model were found to agree with those obtained from the experiment that the leaching process is endothermic in nature hence the positive values of Q and the absorbed heat. The deviations of the predicted Q values from the experimental values were found to be within the acceptable range. The model was found to be dependent on the weight of iron oxide ore added to solution in the course of leaching.

The model is stated as:

$$Q = e^{1.04(\sqrt{W})} \quad (5)$$

where Q = Quantity of heat energy absorbed by hydrogen peroxide solution during the leaching process (J)

$N = 1.04$ (Weight-input coefficient) determined in the experiment[11].

W = Weight of iron oxide ore used (g)

It has been found [12, 13] that the final pH of the leaching solution depend on the leaching time, initial pH for the leaching solution and the leaching temperature.

The aim of this work is to derive a model for predicting the initial solution pH at assumed final pH and leaching time during hydrogen peroxide leaching of Itakpe (Nigeria) iron oxide ore. This derivation is embarked on in furtherance of the previous work [14].

2. Model

The ore is assumed to be stationary in the reaction vessel during the leaching process and contains the unleached iron as part of reaction remnants. The ore is attacked by hydrogen ions from hydrogen peroxide within the liquid phase, and in the presence of oxygen.

2.1 Model Formulation

Results from experimental work [14] carried out at SynchroWell Research Laboratory, Enugu were used for the model derivation. These results are as presented in Table 1.

Computational analysis of these experimental results [14] shown in Table 1, resulted to Table 2 which indicate that;

$$(\text{Int})^{1/2} = N \left(\frac{\beta^C}{\alpha^C} \right) \quad (\text{approximately}) \quad (6)$$

$$(\text{Int})^{1/2} = N \left(\frac{\beta}{\alpha} \right)^C \quad (7)$$

Introducing the values of N and C into equation (6):

$$(\text{Int})^{1/2} = 3.6 \left(\frac{\beta}{\alpha} \right)^{4.1} \quad (8)$$

However in evaluating the initial solution pH β , equation (8) becomes

$$\beta^{4.1} = \left(\frac{\alpha^{4.1} (\text{Int})^{1/2}}{3.6} \right) \quad (9)$$

Taking logarithm of both sides of equation (9)

$$\text{Log} \beta^{4.1} = \text{Log} \left(\frac{\alpha^{4.1} (\text{Int})^{1/2}}{3.6} \right) \quad (10)$$

$$4.1 \text{Log} \beta = \text{Log} \left(\frac{\alpha^{4.1} (\text{Int})^{1/2}}{3.6} \right) \quad (11)$$

$$\text{Log} \beta = 0.2439 \text{Log} \left(\frac{\alpha^{4.1} (\text{Int})^{1/2}}{3.6} \right) \quad (12)$$

$$\beta = \text{Antilog} \left(0.2439 \text{Log} \left(\frac{\alpha^{4.1} (\text{Int})^{1/2}}{3.6} \right) \right) \quad (13)$$

Where

$C = 4.1$ (pH index for oxalic acid solution within the leaching time) determined in the experiment [14].

t = Leaching time (minutes)

β = Initial pH of the hydrogen peroxide leaching solution just before the leaching process started.

α = Final pH of the hydrogen peroxide leaching solution at time t.
 N = 3.6 (Dissolution coefficient of iron in hydrogen peroxide solution at time, t) determined in the experiment [14].
 Equation (13) is the derived model.

Table1: Variation of initial pH with final pH of the leaching solution at constant leaching time.[14]

(β)	(α)	t
7.57	8.67	180.00
7.83	8.80	180.00
7.40	8.87	180.00
7.86	8.99	180.00
8.10	8.95	180.00
9.25	10.19	180.00
9.26	10.20	180.00

Table 2: Variation of β^c and α^c with N (β^c/α^c)

β^c	α^c	($\ln t$) ^{1/2}	N (β^c/α^c)
4020.62	7012.59	2.2788	2.0640
4617.67	7453.82	2.2788	2.2302
3663.11	7699.93	2.2788	1.7126
4690.64	8136.07	2.2788	2.0755
5306.26	7988.67	2.2788	2.3912
9144.95	13599.22	2.2788	2.4209
9185.55	13654.03	2.2788	2.4218

3. Boundary and Initial Condition

Iron oxide ore was placed in cylindrical flask 30cm high containing leaching solution of hydrogen peroxide. The leaching solution is non flowing (stationary). Before the start of the leaching process, the flask was assumed to be initially free of attached bacteria and other micro organism. Initially, the effect of oxygen on the process was assumed to be atmospheric. In all cases, weight of iron oxide ore used was 10g. The initial pH range of leaching solutions used; 7.40-9.26 and leaching time of 3 hrs (180 minutes) were used for all samples. A constant leaching temperature of 25°C was used. Hydrogen peroxide concentration at 0.28mol/litre and average ore grain size; 150µm were also used. Details of the experimental technique are as presented in the report [14].

The leaching process boundary conditions include: atmospheric levels of oxygen (considering that the cylinder was open at the top) at both the top and bottom of the ore particles in the gas and liquid phases respectively. A zero gradient was assumed for the liquid scalar at the bottom of the particles and for the gas phase at the top of the particles. The sides of the particles were assumed to be symmetries.

4. Model Validation

The formulated model was validated by calculating the deviation of the model-predicted initial pH from the corresponding experimental pH values.

The deviation recorded is believed to be due to the fact that the surface properties of the ore and the physiochemical interactions between the ore and leaching solution which were found to play vital roles during the leaching process [14] were not considered during the model formulation. It is expected that introduction of correction factor to the predicted initial pH, gives exactly the experimental initial pH values.

Deviation (Dv) (%) of model-predicted initial pH values from those of the experiment is given by

$$Dv = \frac{Pp - Ep}{Ep} \times 100 \quad (14)$$

$$\left(\frac{Pp - Ep}{Ep} \right)$$

Where Pp = Predicted initial pH values

Ep = Experimental initial pH values

Since correction factor (Cr) is the negative of the deviation,

$$Cr = - Dv \quad (15)$$

Substituting equation (14) into equation (15) for Dv,

$$Cr = -100 \left(\frac{Pp - Ep}{Ep} \right) \quad (16)$$

It was observed that addition of the corresponding values of Cr from equation (16) to the model-predicted initial pH gave exactly the corresponding experimental initial pH values [14].

5. Results and Discussion

The derived model is equation (13). Insignificant positive and negative deviations were found to have resulted on comparing values of the initial pH from the experimental data and those from the model, hence depicting the reliability and validity of the model. This can be deduced from Table 3. The positive and negative deviations of the model-predicted initial pH values from those of the experiment were found to be less than 8% which is quite within the acceptable deviation limit of experimental results. The validity of the model is believed to be rooted on equation (6) where both sides of the equation are approximately equal to 2. Table 2 also agrees with equation (6) following the values of $(\ln t)^{1/2}$ and $N(\beta^C/\alpha^C)$ evaluated after statistical and computational analysis carried out on experimental results in Table 1.

Table 3: Comparison between initial pH as predicted by model and as obtained from experiment [14].

β_{exp}	α_M	Dv (%)	Cr (%)
7.57	7.75	+2.44	-2.44
7.83	7.87	+0.51	-0.51
7.40	7.93	+7.16	-7.16
7.86	8.04	+2.30	-2.30
8.10	8.01	-1.11	+1.11
9.25	9.11	-1.51	+1.51
9.26	9.12	-1.51	+1.51

Where β_{exp} = Initial pH from experiment [14]
 β_M = Initial pH predicted by model.

6. Conclusion

The model predicts the initial solution pH of the leaching solution of hydrogen peroxide during the leaching of Itakpe (Nigeria) iron oxide ore. This prediction could be done during the leaching process providing the expectant final pH of the solution and leaching time are known. The validity of the model is believed to be rooted on equation (6) where both sides of the equation are approximately equal to 2. The respective deviation of the model-predicted initial solution pH value from that of the corresponding experimental value is less than 8% which is quite within the acceptable deviation limit of experimental results.

Acknowledgement

The authors thank Dr. Ekeme Udoh and Pearl Bassey, modelling experts at Linkwell Modelling Centre Calabar for his technical inputs. The management of SynchroWell Nig. Ltd. Enugu is also appreciated for permitting and providing the experimental data used in this work.

References

- [1] Nwoye, C. I., (2006) SynchroWell Research Work Report, DFM Unit, No. 2021196, 28-43.
- [2] Nwoye, C. I. (2008) SynchroWell Research Work Report, DFM Unit, No 2000116, 36-50.
- [3] Nwoye, C. I., Amara, G. N., and Onyemaobi, O. O. (2008) Model for Evaluating Dissolved Iron during Leaching of Iron Oxide Ore in Sulphuric Acid Solution, Inter. J. Nat. Appl. Sc., 4(2): 209-211.
- [4] Lee, S. O., Oh, J. K., Shin, B. S. (1999) Dissolution of Iron Rust Materials using Oxalic Acid. J. Min. Metall. Inst. Jpn. 115, 815-819.
- [5] Taxiarchour, M., Pnias, D., Doumi, I., Paspaliaris, I., Kontopoulos, A., (1997a) Removal of Iron from Silica Sand by Leaching with Oxalic Acid, Hydrometallurgy, 46, 215-227.
- [6] Lee, S.O, Tran, T., Park Y.Y., Kim S.J., and Kim, M. J. (2006) Study on the Kinetics of Iron Leaching by Oxalic Acid. Int. J. Miner Process, 80, 144-152.
- [7] Taxiarchou, M., Pnias, D., Doumi, I., Paspaliaris, I., and Kontopoulos, A. (1997b) Dissolution of Haematite in Acidic Oxalate Solutions. Hydrometallurgy, 44, 287-299.
- [8] Pnias, D., Taxiarchou, M., Paspaliaris, I., Kontopoulos, A. (1996) Mechanism of Dissolution of Iron Oxides in Aqueous Oxalic Acid. Hydrometallurgy, 42, 257-265.
- [9] Nwoye, C. I. (2008) Model for Quantitative Analysis of Dissolved Iron in Oxalic Acid Solution during

- Leaching of Iron Oxide Ore, *Inter. Res. J. Eng. Sc. Tech.*, 5(1): 37-41.
- [10] Nwoye, C. I., Agu, P.C., Mark, U., Ikele, U.S., Mbuka, I. E., and Anyakwo, C. N. (2008) Model for Predicting Phosphorus Removal in Relation to Weight of Iron Oxide Ore and pH during Leaching with Oxalic Acid *Inter. J. Nat. Appl. Sc.*, 4(3): 106-112.
- [11] Nwoye, C. I. (2009) Model for Computational Analysis of Quantity of Heat Absorbed by Hydrogen Peroxide Solution relative to Weight-Input of Iron Oxide Ore during Leaching. *J. Eng. & App. Sc.*, 15(2), 40-52.
- [12] Pinches, A. (1975) Bacterial Leaching of an Arsenic Bearing Sulphide Concentrate. The Institute of Mining and Metallurgy, England, 34.
- [13] Nwoye, C. I. (2008) Ph.D Thesis, Metallurgical and Materials Engineering Department, Federal University of Technology, Owerri, 178.
- [14] Nwoye, C. I. (2007) SynchroWell Research Work Report, DFM Unit, No 2668115, 18-30.

Model for Calculating the Concentration of Leached Iron Relative to the Final Solution Temperature during Sulphuric Acid Leaching of Iron Oxide Ore

Chukwuka Ikechukwu Nwoye¹, Gideon Chima Obasi², Udochukwu Mark¹, Stanley Inyama³, Chinedu Chris Nwakwuo⁴

^{*1}Department of Materials and Metallurgical Engineering Federal University of Technology, Owerri, Nigeria.

²Department of Material Science Aveiro, University, Portugal

³Department of Industrial Mathematics, Federal University of Technology, Owerri, Nigeria

⁴Department of Material Science Oxford University, United Kingdom
chikeyn@yahoo.com

Abstract: Model for calculating the concentration of leached iron during leaching of iron oxide ore in sulphuric acid solution has been derived. The model $\%Fe = e^{-2.0421(\ln T)}$ was found to predict %Fe (leached) very close to the values obtained from the experiment, being dependent on the values of the final leaching solution temperature measured during the leaching process. It was observed that the validity of the model is rooted in the expression $\ln(\%Fe) = N(\ln T)$ where both sides of the expression are correspondingly approximately equal. The positive or negative deviation of each of the model-predicted values of %Fe (leached) from those of the experimental values was found to be less than 37% which is quite within the range of acceptable deviation limit for experimental results, hence indicating the usefulness of the model as a predictive tool. [New York Science Journal. 2009;2(3):49-54]. (ISSN: 1554-0200).

Keywords: Model, Calculation, Leached Iron, Sulphuric Acid, Iron Oxide Ore, Solution Temperature

1. Introduction

The dissolution of iron oxide is believed to take place via a photo-electro chemical reduction process, involving a complicated mechanism of charge transfer between the predominant oxalate species, namely ferric oxalate $Fe(C_2O_4)_3^{3-}$, ferrous oxalate $Fe(C_2O_4)_2^{2-}$ acting also as an auto catalyst, and the oxalate ligand on the iron oxide surface [1]. The dissolution of iron oxides in oxalic acid was found to be very slow at temperatures within the range 25-60°C, but its rate increases rapidly above 90°C [2]. The dissolution rate also increases with increasing oxalate concentration at the constant pH values set within the optimum range of pH 2.5-3.0. At this optimum pH, the dissolution of fine pure haematite (Fe_2O_3) (105-140µm) follows a diffusion-controlled shrinking core model [2]. Taxiarchour et al [3] reported that it took close to 40h to dissolve 80% of pure haematite slurry (97% purity, 0.022% w/v or 0.21% g/L Fe_2O_3) at pH 1. He stated that even at 90°C, it required close to 10h to achieve 95% dissolution of iron of the slurry at pH 1. They also dissolved iron using 0.1-0.5M oxalic acid (pH1-5) to dissolve iron from a 20% w/v slurry (83% of particle size in the range 0.18-0.35mm, containing 0.029% Fe_2O_3). The iron oxide concentration in the leach is equivalent to 0.058g/L Fe_2O_3 .

The speciation of Fe(III) oxalate and Fe(II) oxalate has been found [4] to be governed by pH and total oxalate concentration. For a having $pH > 2.5$ and an oxalate concentration higher than 0.1M, the most predominant Fe(III) complex ion existing is $Fe(C_2O_4)_3^{3-}$. At these conditions, ($pH > 2.5$ and an oxalate concentration higher than 0.1M) the predominant Fe(II) complex species is $Fe(C_2O_4)_2^{2-}$.

Lee et al. [5] reported that the leaching of 3g/L pure haematite (98.2% purity, 105-140µm size range) using 0.048-0.48M oxalic acid at 80-100°C passed through a maximum peak at pH 2.5. Dissolution of haematite was found [5] to be slower than magnetite ($FeO \cdot Fe_2O_3$) and other hydrated iron oxide such as goethite (α - $FeOOH$), lapidochrosite (γ - $FeOOH$) and iron hydroxide ($Fe(OH)_3$).

The presence of Fe^{2+} was found to significantly enhance the leaching of iron extraction from silica sand at a temperature even as low as 25°C [3]. Ferrous oxalate however is oxidized quickly by air during the dissolution and in general an induction period of a few hours was observed to exist unless a strong acidic environment ($pH < 1$) or an inert atmosphere is maintained. Maintaining the high level of ferrous oxalate in the leach liquor using an inert gas, was found [3] to enhance the reaction kinetics.

Ambikadevi and Lalithambika [6] evaluated the effectiveness of several organic acids (such as acetic, formic, citric, ascorbic acids etc.) used for dissolving iron from iron compounds. Oxalic acid was found to be the most promising because of its acid strength, good complexing characteristics and high reducing power, compared to other organic acids. Using oxalic acid, the dissolved iron can be precipitated from the

leach solution as ferrous oxalate, which can be re-processed to form pure haematite by calcinations [7]. Many researchers have studied the use of oxalic acid to dissolve iron oxide on a laboratory scale [8-14]. Lee et al [15] used 0.19-0.48M oxalic acid to dissolve hydrated iron oxide. Iron dissolution was found [15] to reach 90% for a 20% slurry within 60mins. using 0.19M oxalic for the finer fraction (< 150µm) containing 0.56% Fe₂O₃. The coarser fraction (>150µm) containing 1.06% Fe₂O₃ achieved a lower iron removal, reaching a steady state of only 78% after 1 h of leaching. Although the pH was not measured or controlled, it was expected that the liquor pH is < pH1 at the oxalic acid concentration range studied (0.19-0.48M). Taxiarchou et al.[7] found that the maximum iron dissolution of only 40% is within 3h at temperatures in the range 90-100°C. At 0.5M oxalate and all temperatures (25, 60 and 80°C) the dissolution of iron was faster at a lower pH in the range pH 1-5 studied. Biological processes for iron dissolution have been evaluated by several researchers based on the use of several micro organisms that were easily sourced and isolated. Mandal and Banerjee [16] recently presented their findings on the study of the use of *Aspergillus niger* and their cultural filtrates for dissolving iron present in iron compounds.

Nwoye [17] derived a model for quantitative analysis of dissolved iron in oxalic acid solution in relation to the final pH of the solution during leaching of iron oxide ore;

$$\gamma = 0.5 \left(\frac{K_1[\%Fe_2O_3] + K_2[\%Fe]}{[\%Fe][\%Fe_2O_3]} \right) \quad (1)$$

where

K_1 and K_2 = Dissolution constants of Fe and Fe₂O₃ respectively.

γ = pH of leaching solution after time t (mins.).

The values of the dissolution constants compared with those of % Fe and % Fe₂O₃ from the experiment [17] indicate clearly that the constants K_1 and K_2 are numerical equivalence of the chemical resistance to the dissolution of Fe and Fe₂O₃ (respectively) in oxalic acid solution. It was found that $K_1 \approx 2K_2$ indicating twice chemical resistance to the dissolution Fe compare to that of Fe₂O₃. This expression agreed with the higher percentage of Fe₂O₃ dissolved compared to that of the corresponding Fe. The model also predicted the final pH of the leaching solution when the concentrations of Fe and Fe₂O₃ dissolved (at a temperature of 30°C and average ore grain size; 150µm) are known.

Model has been derived [18] for predicting the concentration of phosphorus removed during leaching of iron oxide ore in oxalic acid solution. The model is expressed as;

$$P = \left(\frac{150.5}{\mu\alpha} \right) \quad (2)$$

Where

P = Concentration of phosphorus removed during the leaching process (mg/Kg)

(μ) = Weight input of iron oxide ore (g)

(α) = Final pH of the leaching solution at the time t when P is evaluated

150.5 = (pH coefficient for phosphorus dissolution in oxalic acid solution during the process) determined in the experiment [18].

The model [18] predicted the concentration of phosphorus removed, with high degree of precision being dependent on the final pH of the leaching solution and weight input of the iron oxide ore. It also shows that the concentration of phosphorus removed (at a temperature of 25°C, average ore grain size; 150µm and initial leaching solution pH 5.5) is inversely proportional to the product of the final pH of the leaching solution and the weight input of the iron oxide ore.

It has been found [19, 20] that the final pH of the leaching solution depend on the leaching time, initial pH for the leaching solution and the leaching temperature.

It has been reported [21] that phosphorus could be removed from Itakpe iron oxide ore through a leaching process using sulphuric acid solution. Chemical analysis carried out on the iron ore indicates that the percentage of phosphorus in the ore is about 1.18%, which from all indication is quite high and could cause embrittlement and other adverse effects on the service life of engineering materials made from such iron ore. This was the basis for the dephosphorization process carried out [21]. Phosphorus was removed (at a temperature of 25°C, average ore grain size; 150µm and initial leaching solution pH range 0.47-0.53) and then dissolved in the acid solution in the form of phosphorus oxide.

Nwoye et al [22] derived a model for predicting the concentration of dissolved iron during leaching of iron oxide ore in sulphuric acid solution. The model is stated as;

$$\%Fe = 0.35(\alpha/T)^3 \quad (3)$$

Where

T = Solution temperature at the time t, when the concentration of dissolved iron is evaluated. ($^{\circ}C$)

0.35= (pH coefficient for iron dissolution in sulphuric acid solution during the leaching process) determined in the experiment [22].

α = Final pH of the leaching solution at the time t, when the concentration of dissolved iron is evaluated.

The model (formulated at conditions; leaching temperature of $25^{\circ}C$, initial solution pH 5.0 and average grain size; $150\mu m$) is dependent of the final pH and temperature of the leaching solution. The model shows that the concentration of iron dissolved during the leaching process is directly proportional to the third power of the ratio of final leaching and temperature.

The aim of this work is to derive a model for calculating the concentration of leached iron relative to the final solution temperature during leaching of Agbaja (Nigeria) iron oxide ore in sulphuric acid solution.

2. Model

The solid phase (ore) is assumed to be stationary, contains the un-leached iron remaining in the ore. Hydrogen ions from the sulphuric acid attack the ore within the liquid phase in the presence of oxygen.

2.1 Model Formulation

Experimental data obtained from research work [23] carried out at SynchroWell Research Laboratory, Enugu were used for this work.

Results of the experiment as presented in report [23] and used for the model formulation are as shown in Table 1.

Computational analysis of the experimental data [23] shown in Table 1, gave rise to Table 2 which indicate that;

$$\ln(\%Fe) = N(\ln T) \quad (\text{approximately}) \quad (4)$$

$$\%Fe = e^{N(\ln T)} \quad (5)$$

Introducing the value of N into equation (5)

$$\%Fe = e^{-2.0421(\ln T)} \quad (6)$$

where

$\%Fe$ = Concentration of leached iron during the leaching process.

T= Leaching solution temperature at the time t when the concentration of leached iron is evaluated. ($^{\circ}C$)

N= -2.0421(Temperature coefficient for iron dissolution in sulphuric acid solution during leaching of iron oxide ore) determined in the experiment [23].

Equation (6) is the derived model.

Table1: Variation of weight input of iron oxide ore with final leaching solution temperature and leached iron. [23]

M	T ($^{\circ}C$)	$\%Fe (10^{-3})$
8	26.01	1.7820
12	26.00	1.4000
14	25.90	1.6000
16	25.80	1.3000
18	25.76	1.0000
20	26.20	2.0000

Table 2: Variation of In(%Fe) with N(InT)

In(%Fe)	N(InT)
-6.3300	-6.6541
-6.5713	-6.6534
-6.4378	-6.6455
-6.6454	-6.6376
-6.9078	-6.6344
-6.2146	-6.6690

3. Boundary and Initial Condition

Consider iron ore in cylindrical flask 30cm high containing leaching solution of sulphuric acid. The leaching solution is stationary i.e (non-flowing). The flask is assumed to be initially free of attached bacteria. Initially, atmospheric levels of oxygen are assumed. Weight of iron oxide ore used; (8-20g), initial pH of leaching solution; 5.0 and leaching time; 30 minutes were used. Leaching temperature used; 25°C. Ore grain size; 150µm, volume of leaching solution; 0.1 litre and sulphuric acid concentration; 0.1mol/litre was used. These and other process conditions are as stated in the experimental technique [23]. The boundary conditions are: atmospheric levels of oxygen (since the cylinder was open at the top) at the top and bottom of the ore particles in the liquid and gas phases respectively. At the bottom of the particles, a zero gradient for the liquid scalar are assumed and also for the gas phase at the top of the particles. The leaching solution is stationary. The sides of the particles are taken to be symmetries.

4. Model Validation

The formulated model was validated by direct analysis and comparison of %Fe values from model data and those from the experimental data for equality or near equality.

Analysis and comparison between these data reveal deviations of model data from experimental data. This is believed to be due to the fact that the surface properties of the ore and the physiochemical interactions between the ore and leaching solution which were found to have played vital roles during the leaching process [23] were not considered during the model formulation. This necessitated the introduction of correction factor, to bring the model data to that of the experimental values. (See Table 3)

Deviation (Dv) (%) of model %Fe values from experimental %Fe values is given by

$$Dv = \left(\frac{Dp - DE}{DE} \right) \times 100 \quad (7)$$

Where Dp = Predicted %Fe values from model

DE = Experimental %Fe values

Correction factor (Cf) is the negative of the deviation i.e

$$Cf = -Dv \quad (8)$$

Therefore

$$Cf = \left(\frac{Dp - DE}{DE} \right) \times 100 \quad (9)$$

Introduction of the corresponding values of Cf from equation (9) into the model gives exactly the corresponding experimental %Fe values [23].

Table 3: Comparison between %Fe dissolved as predicted by model and as obtained from experiment [23].

%Fe _{exp} (10 ⁻³)	%Fe _M (10 ⁻³)	Dv (%)	Cf (%)
1.7820	1.2887	-27.68	+27.68
1.4000	1.2897	-7.88	+7.88
1.6000	1.3000	-18.75	+18.75
1.3000	1.3102	+0.78	-0.78
1.0000	1.3143	+31.43	-31.43
2.0000	1.2697	-36.52	+36.52

Where

%Fe_{exp} = %Fe values from experiment [23]

%Fe_M = %Fe values predicted by model

5. Results and Discussion

The derived model is equation (6). A comparison of the values of %Fe from the experimental data and those from the model shows positive and negative deviations less than 37% which is quite within the range of acceptable deviation limit of experimental results, hence depicting the reliability and validity of the model. This is shown in Table 3. The validity of the model is believed to be rooted on equation (4) where both sides of the equation are correspondingly approximately equal. Table 2 also agrees with equation (4) following the values of $\ln[\%Fe]$ and $N(\ln T)$ evaluated from Table 1 as a result of corresponding computational analysis.

6. Conclusion

The model calculates the concentration of leached iron relative to the final leaching solution temperature during leaching of Agbaja iron oxide ore in sulphuric acid solution. The validity of the model is believed to be rooted on equation (4) where both sides of the equation are correspondingly approximately equal. The deviation of the model-predicted %Fe values from those of the experiment is less than 37% which is quite within the range of acceptable deviation limit of experimental results. The model is therefore useful as a predictive tool.

Further works should incorporate more process parameters into the model with the aim of reducing the deviations of the model-predicted %Fe values from those of the experiment.

Acknowledgement

The authors thank Dr. Ekeme Udoh, a modelling expert at Linkwell Modelling Centre Calabar for his technical inputs. The management of SynchroWell Nig. Ltd. Enugu is also appreciated for permitting and providing the experimental data used in this work.

References

- [1] Taxiarchour, M., Panias, D., Doumi, I., Paspaliaris, I., Kontopoulos, A., (1997a) Removal of Iron from Silica Sand by Leaching with Oxalic Acid, *Hydrometallurgy*, 46, 215-227.
- [2] Lee, S.O, Tran, T., Park Y.Y., Kim S.J., and Kim, M. J. (2006) Study on the Kinetics of Iron Leaching by Oxalic Acid. *Int. J. Miner Process*, 80, 144-152.
- [3] Taxiarchou, M., Panias, D., Doumi, I., Paspaliaris, I., and Kontopoulos, A. (1997a) Dissolution of Haematite in Acidic Oxalate Solutions. *Hydrometallurgy*, 44, 287-299.
- [4] Panias, D., Taxiarchou, M., Paspaliaris, I., Kontopoulos, A. (1996) Mechanism of Dissolution of Iron Oxides in Aqueous Oxalic Acid. *Hydrometallurgy*, 42, 257-265.
- [5] Lee, S. O., Oh, J. K., Shin, B. S. (1999) Dissolution of Iron Rust Materials using Oxalic Acid. *J. Min. Metall. Inst. Jpn.* 115, 815-819.
- [6] Ambikadevi, V. R., Lalithambika, M., (2000) Effects of Organic Acids on Ferric Iron Removal from Iron-Stained Kaolinite. *Appl. Clay Sci.* 16, 133-145.
- [7] Taxiarchour, M., Panias, D., Doumi, I., Paspaliaris, I., Kontopoulos, A. (1997b) Removal of iron from Silica Sand by Leaching with Oxalic Acid, *Hydrometallurgy*, 46, 215-227.
- [8] Vaglio, F., Passariello, B., Barbaro, M., Plescia, P., Marbini, A. M. (1998)
- [9] Segal, M. G., Sellers, R. M., (1984) In: Sykes, A.G. (Ed.), *Advances in Inorganic and Bioinorganic Mechanisms*, 1(3). Academic Press, London, 1984, p.97.
- [10] Frenier, W. W., Growcock, F.B., (1984) Mechanism of Iron Oxide Dissolution, a Review of Recent Literature. *Corrosion NACE*, 40, pp. 663-668.
- [11] Jepson, W.B., (1988) Structural Iron in Kaolinite and in Associated Ancillary Materials. In: Stucki, J. W., Goodman, B. A., Schwertmann, U. (Ed.), *Iron in Soils and Clay Minerals*. NATO ASI Ser, 217. D. Reidel Publ. Co., Dordrecht, Holland, pp. 467-536.
- [12] Panias, D., Taxiarchou, M., Paspaliaris, I., Kontopoulos, A. (1996) Mechanism of Dissolution of Iron Oxides in Aqueous Oxalic Acid. *Hydrometallurgy* 42, 257-265.
- [13] Blesa, M. A., Morando, P. J., Regazzoni, A. E., (1994) *Chemical Dissolution of Metal Oxides*. CRC Press, Inc., pp. 269-308.
- [14] Cornell, R. M., Schindler, P. W., (1987) Photochemical Dissolution of Goethite in Acid/Oxalate Solution. *Miner.* 35(5), 347-352.
- [15] Lee, S.O., Tran, T., Park Y.Y., Kim S.J., and Kim, M.J; Study on the Kinetics of Iron Leaching by Oxalic acid. *Int. J. Miner process*, 80, 2006, 144-152.
- [16] Mandal, S. K., Banerjee, P. C., (2004) Iron Leaching with Oxalic Acid: Effects of Different Physico-Chemical Parameters. *Int. J. Miner. Process.* 74, 263-270.
- [17] Nwoye, C. I. (2008) Model for Quantitative Analysis of Dissolved Iron in Oxalic Acid Solution during Leaching of Iron Oxide Ore, *Inter. Res. J. Eng. Sc. Tech.*, 5(1): 37-41.
- [18] Nwoye, C. I., Agu, P.C., Mark, U., Ikele, U.S., Mbuka, I. E., and Anyakwo, C. N. (2008) Model for Predicting Phosphorus Removal in Relation to Weight of Iron Oxide Ore and pH during Leaching with Oxalic Acid *Inter. J. Nat. Appl. Sc.*, 4(3): 106-112.
- [19] Pinches, A. (1975) *Bacterial Leaching of an Arsenic Bearing Sulphide Concentrate*. The Institute of Mining and Metallurgy, England, 34.
- [20] Nwoye, C. I. (2008) Ph.D Thesis, Metallurgical and Materials Engineering Department, Federal University of Technology, Owerri, 178.
- [21] Nwoye, C. I. (2008) SynchroWell Research Work Report, DFM Unit, No 2000116, 36-50.
- [22] Nwoye, C. I., Amara, G. N., and Onyemaobi, O. O. (2008) Model for Evaluating Dissolved Iron during Leaching of Iron Oxide Ore in Sulphuric Acid Solution, *Inter. J. Nat. Appl. Sc.*, 4(2): 209-211.
- [23] Nwoye, C. I. (2004) SynchroWell Research Work Report, DFM Unit, No 2588115, 8-15.

Model for Quantifying the Extent and Magnitude of Water Evaporated during Time Dependent Drying of Clay

Chukwuka Ikechukwu Nwoye*¹, Chinedu Chris Nwakwuo², Martins Chidi Obi³,
Gideon Chima Obasi⁴, Okechukwu Onyebuchi Onyemaobi¹

¹Department of Materials and Metallurgical, Engineering Federal University of Technology, Owerri, Nigeria.

²Department of Materials Science, Oxford University, United Kingdom.

³Department of Industrial Mathematics, Federal University of Technology, Owerri, Nigeria.

⁴Department of Materials Science, Aveiro University, Portugal
chikeyn@yahoo.com

Abstract

Model for quantifying the extent and magnitude of water evaporated during time-dependent drying of clay has been derived. The model; $\gamma = \exp((\text{Int}/2.9206)^{1.4})$ shows that the quantity of evaporated water during the drying process is dependent on the drying time, the evaporating surface being constant. It was found that the validity of the model is rooted in equation (1) where both sides of the equation are correspondingly almost equal. The respective deviation of the model-predicted quantity of evaporated water from the corresponding experimental value is less than 19% which is quite within the acceptable deviation range of experimental results, hence depicting the usefulness of the model. [New York Science Journal. 2009;2(3):55-58]. (ISSN: 1554-0200).

Keywords: Model, Water, Evaporation, Drying, Clay

1. Introduction

According to Barsoum (1997a), the contents of the basic clay materials are divided into three groups. The first group involves clays containing mainly the mineral kaolinite. The second groups are clays containing mineral montmorillonite, while the third group are clays which are intermediate product of disintegration of mica into kaolin. The structure of sinters and pellets may be divided into two parts viz, the mineral and the pores. It is widely accepted that the properties of pellets and sinters are closely related to the mineral constituents (Unal, 1986).

Voids volume in packed dispersed powder according to Furnass (1928), depends on the ratio of smallest size (Ss) to largest size (Ls) particle as well as the percentage of constituent monosized particles. He maintained that the smaller the (Ss/Ls) ratio, the more continuous the distribution and the lower the void volume of the system. It has been discovered (Singer and Singer, 1963), that on heating dried clays, water is given off. With time, a hard but porous piece forms. A swollen appearance might occur during the release of some gases, but overall shrinkage must occur when verifications set in leading to a strong dense piece.

Chemical composition of the pellet, pelletisation parameters and firing conditions has been found to affect the shrinkage of clay pellets (Nwoye, 2003a). He posited that the rate of chemical reaction is very much dependent on the gas-solid contact area, which is mostly governed by the porosity of the pellet. He also stated that the shrinkage of clay is probably due to volume change resulting from evacuation of water from the voids, reduction of the size of the pores as well as decrease in the interparticle separation.

Recent analysis (Viewey and Larrly, 1978a) shows that fine particles shrink more, are denser and exhibit excellent mechanical properties. These ceramists also came out with some startling findings following investigations carried out on the relationship between particle size and size distribution with linear drying shrinkage, firing shrinkage and apparent porosity. They concluded that no visible relationship exists between particle size and linear drying shrinkage. Finer particles tend to shrink more. They also stated that the finer the particle size, the lesser the apparent porosity and greater the bulk density.

Arisa, (1997) stressed that the behaviour of ceramic product are very dependent on their composition, grain size, grain distribution, structure of grain and pores. Nwoye (2003b) also posited that the grain size and grain distribution of the clays have significant effect on their physical and technological properties (binding ability, shrinkage and plasticity).

Pores are usually deleterious to the strength of ceramics not only because they reduce cross-sectioned area over which the load is applied but more importantly act as stress concentrators (Barsoum, 1997b). Viewey

and Larrly, (1978b) in an intensive study of the relationship between particle size and linear drying shrinkage revealed that there is no visible relationship existing between them. They also stated that the finer the particle size, the lesser the apparent porosity and the greater the bulk density.

Reed, (1988a) described firing as having three stages through which it proceeds; preliminary reactions which include binder burnout, elimination of gaseous product of decomposition and oxidation, sintering as well as cooling which may include thermal and chemical annealing.

Several works (Singer and Singer, (1963); Reed, (1988); Keey, (1978); Barsoum, (1997)) have been done on shrinkage of clay but none of them investigated the effect of porosity on the swelling and shrinkage behaviour of clay. Porosity is known to influence the swelling and shrinkage behaviour of clay sinters and pellets.

Drying according to Reed (1988b) occurs in three stages; increasing rate, constant and decreasing rate. He pointed out that during the increasing rate; evaporation rate is higher than evaporating surface hence more water is lost. At constant rate, the evaporation rate and evaporation surface are constant. He posited that shrinkage occurs at this stage. Keey (1978) suggested that at this stage, free water is removed between the particles and the interparticle separation decreases, resulting in shrinkage. During the decreasing rate, particles make contacts as water is removed, which causes shrinkage to cease.

The present work is to derive a model for quantifying the extent and magnitude of water evaporated during time-dependent drying of Nsu (Nigeria) clay.

2. Model formulation

Experimental data obtained from research work (Nwoye,2007) carried out at SynchroWell Research Laboratory, Enugu were used for this work. Results of the experiment used for the model formulation are as shown in Table 1.

Computational analysis of the experimental data (Nwoye,2007) shown in Table 1, gave rise to Table 2 which indicate that;

$$\ln\gamma = (\ln t / \ln \beta)^N \quad (\text{approximately}) \quad (1)$$

$$\gamma = \exp((\ln t / \ln \beta)^N) \quad (2)$$

Introducing the values of β and N into equation (2)

$$\gamma = \exp((\ln t / 2.9206)^{1.4}) \quad (3)$$

Where

(γ) = Weight of water lost by evaporation during the drying process (g)

(β) = Area of evaporating surface (mm^2)

$N = 1.4$; (Collapsibility coefficient of binder-clay particle boundary at the drying temperature of 90°C) determined in the experiment (Nwoye, 2007).

t = Drying time (mins.).

Table 1: Variation of quantity of evaporated water with drying time (Nwoye,2007)

(t)	(β)	(γ)
30	833	2.90
50	833	3.90
70	833	5.90
90	833	6.60
110	833	7.60
130	833	8.01

Table 2: Variation of $\ln\gamma$ with $(\ln t/\ln \beta)^N$

Int	Log β	$\ln\gamma$	$(\ln t/\ln \beta)^N$
3.4012	2.9206	1.0647	1.2378
3.9120	2.9206	1.3610	1.5056
4.2485	2.9206	1.7750	1.6900
4.4998	2.9206	1.8871	1.8315
4.7005	2.9206	2.0281	1.9468
4.8675	2.9206	2.0807	2.0446

3. Boundary and Initial Conditions

Consider a rectangular shaped clay product of length 49mm, width 17mm, and breadth 9mm exposed to drying in the furnace while it was in wet condition. Initially, atmospheric levels of oxygen are assumed. Atmospheric pressure was assumed to be acting on the clay samples during the drying process (since the furnace is not air-tight). The grain size of clay particles used is 425 μ m, weight of clay and binder (bentonite) used (for each rectangular product); 100g and 10g respectively, quantity of water used for mixing; 2% (of total weight), drying temperature used; 90 $^{\circ}$ C, area of evaporating surface; 833mm 2 and range of drying time used; (30-130 mins.).

The boundary conditions are: Atmospheric levels of oxygen at the top and bottom of the clay samples since they are dried under the atmospheric condition. No external force due to compression or tension was applied to the drying clays. The sides of the particles and the rectangular shaped clay products are taken to be symmetries.

4. Model Validation

The formulated model was validated by direct analysis and comparison of the model-predicted γ values and those from the experiment for equality or near equality.

Analysis and comparison between these γ values reveal deviations of model-predicted γ from those of the experimental values. This is believed to be due to the fact that the surface properties of the clay and the physiochemical interactions between the clay and binder, which were found to have played vital role during the evaporation process (Nwoye, 2007) were not considered during the model formulation. This necessitated the introduction of correction factor, to bring the model-predicted γ value to that of the corresponding experimental value (Table 3).

Deviation (D_v) (%) of model-predicted γ values from the experimental γ values is given by

$$D_v = \frac{DP - DE}{DE} \times 100 \quad (4)$$

Where DP = γ values predicted by model

DE = γ values obtained from experiment

Correction factor (Cf) is the negative of the deviation i.e

$$C_f = -D_v \quad (5)$$

Therefore

$$C_f = -100 \left(\frac{DP - DE}{DE} \right) \quad (6)$$

Introduction of the value of Cf from equation (6) into the model gives exactly the corresponding experimental value of γ (Nwoye, 2007).

5. Results and Discussion

The derived model is equation (3). A comparison of the values of γ obtained from the experiment and those from the model shows little deviations hence depicting the reliability and validity of the model (Table 3). The respective deviation of the model-predicted quantity of evaporated water from the corresponding experimental value is less than 19% which is quite within the acceptable deviation range of experimental results, hence depicting the usefulness of the model. It was found that the validity of the model is rooted in equation (1) where both sides of the equation are correspondingly almost equal. Table 2 also agrees with

equation (1) following the values of $\ln\gamma$ and $(\ln/\text{Log}\beta)^N$ evaluated from Table 1 as a result of corresponding computational analysis.

Table 3: Comparison between quantities of evaporated water as predicted by model and as obtained from experiment. (Nwoye, 2007)

γ_{exp}	γ_M	Dv (%)	Cf (%)
2.90	3.4480	+18.90	-18.90
3.90	4.5069	+15.56	-15.56
5.90	5.4195	-8.14	+8.14
6.60	6.2432	-5.41	+5.41
7.60	7.0062	-7.81	+7.81
8.01	7.7261	-3.54	+3.54

where $\gamma_{\text{exp}} = \gamma$ values obtained from experiment (Nwoye, 2007)
 $\gamma_M = \gamma$ values predicted by model.

6. Conclusion

The model evaluates the quantity of water lost by evaporation during drying of Nsu (Nigeria) clay at 90°C. It was found that the validity of the model is rooted in equation (1) where both sides of the equation are correspondingly almost equal. The respective deviation of the model-predicted quantity of evaporated water from the corresponding experimental value is less than 19% which is quite within the acceptable deviation range of experimental results, hence depicting the usefulness of the model.

Further works should incorporate more process parameters into the model with the aim of reducing the deviations of the model-predicted γ values from those of the experimental.

Acknowledgement

The authors thank Dr. Ekeme Udoh, a modelling expert at Linkwell Modelling Centre Calabar for his technical inputs. The management of SynchroWell Nig. Ltd. Enugu is also appreciated for permitting and providing the experimental data used in this work.

References

- Arisa, U. S., (1997) Effect of Initial Particle Size and Size Distribution on Physical and Mechanical Properties of Some Nigeria Clays Sintered at 1200°C. A Thesis Report, p3,15-18.
- Barsoum, M., (1997a) Fundamentals of Ceramics. McGraw Hill Incorporated, Singapore p410-420.
- Barsoum, M., (1997b) Fundamentals of Ceramics McGraw Hill Incorporated Singapore, p420-430.
- Furnass, C.C., (1928) The Relationship Between Specific Voids and Size of Compression In System of Broken Solid of Mixed Size US Bureau Report Investigation Vol. 2894 p 321-340.
- Keey, R.B., (1978) Introduction to Industrial Drying Operations, Pergamon Press, Elmsford, New York. p132-157.
- Nwoye, C. I. (2003a) Investigating the Influence of Particle Size and Size Distribution on the Physical and Mechanical Properties of Ceramic Materials. A Project Report p5-8, 16-22.
- Nwoye, C. I. (2003b) Investigating the Influence of Particle Size and Size Distribution on the Physical and Mechanical Properties of Ceramic Materials. A Project Report p28.
- Nwoye, C. I., (2007). SynchroWell Research Work Report, DFM Unit, No 2007156, p16-26.
- Reed, J., (1988a) Principles of Ceramic Processing, Wiley Interscience Publication, Canada p470.
- Reed, J., (1988b) Principles of Ceramic Processing, Wiley interscience publication, Canada p270.
- Singer, F. and Singer, S.S., (1963). Industrial Ceramics, University Press Cambridge p44.
- Viewey, F. and Larrly, P., (1978). Ceramic Processing Before Firing, John-Wiley and Sons, New York, p3-8.
- Viewey, F. and Larrly, P., (1978). Ceramic Processing Before Firing, John-Wiley and Sons, New York, p10.
- Unal, A., (1986) Trans Institute of Metallurgy Section C. 95, p179.

Scale Analysis of Fluid Flow and Forced Convective Heat Transfer in the Entrance Region of Elliptic Conduits

I. K. Adegun and O. A. Oladosu
Mechanical Engineering Department, Faculty of Engineering and Technology
University of Ilorin, P.M.B. 1515, Ilorin, Nigeria

kadegun2000@yahoo.com; oladosu_olalekan@yahoo.com

Abstract: The paper presents heuristic scale technique to study fluid flow and heat transfer in the entrance region of elliptic ducts starting with conservation laws of mass, momentum and energy transport. The method provides a powerful scheme to approximate heat transfer parameters required for the design of heat exchangers as in the case of solar collector, automotive radiator, transformer and other heat transfer equipment. A generalized boundary condition in which no mode of heating is specified is imposed on the fluid flow. Generalized equations of thermal entrance length L_t' , hydrodynamic entrance length L_h' , friction coefficient f' , axial pressure drop dp' , and Nusselt number Nu' are developed. The results obtained from the analysis show that the generalized Nusselt number, thermal entrance length and hydrodynamic entrance length are independent of fluid properties and therefore depends solely on the eccentricity of the ellipse. The results also indicated that the Nusselt number at the end of minor axis is greater than that of the major axis. Also obtained is hydrodynamic characteristic $fRe=16$ for $e=0$ which compares well with the value compiled by Necati Ozsiki for a circular geometry ($e=0$). [New York Science Journal. 2009;2(3):59-71]. (ISSN: 1554-0200).

Keywords: Analytical, Fluid, Scale, Entrance, Ellipse

INTRODUCTION

The present investigation, using a generalized boundary condition, is to establish the validity of scheme of scale analysis for the solution of engineering problems and to predict parameters required for design of heat exchanger as in the case of solar collector, nuclear reactor, power plant radiator and some other heat transfer equipment. However, the scheme has proved its worth as a hypothesis in engineering and technology by giving an appropriate theoretical analysis to generate a generalized condition to predict both hydrodynamic and thermal entrance lengths in any elliptic configuration. Among previous researchers who had worked in closely related areas are Horneck[1], Shah[2] and Wiginton[3]. They studied laminar flow in entrance region of pipe, rectangular duct and parallel plates respectively. Abdel-Wahed et al.[4] also carried out extensive practical investigation in study of laminar developing and fully developed flows and heat transfer in horizontal elliptic duct. Numerical study of entrance region heat transfer was considered by Webb[5]. Kutcher et al.[6] analyzed some aspect of unglazed transpired solar collector using scale approach. Kutcher[7] also introduced scale analysis in solving some parts of his problem. Analysis of laminar flow and heat transfer in the entrance region of an internally finned circular duct has been investigated by Parakash[8]. Bello-Ochende and Adegun[9] studied heat transfer in polygonal ducts using scale technique. Adegun[10] also investigated heat transfer in the entrance of concentric elliptic annulus using scaling method. Bello-Ochende and Adegun[11] also studied heat transfer in elliptic duct using perturbation technique. Osizik[12] compiled results for generalized thermal and hydrodynamic entrance lengths for various geometries.

Focus of the Work

The present study is an investigation of forced convection and fluid flow in elliptic ducts. The authors adopted an approximate method called scale analysis. A physical model of the problem is shown in Fig.1. The duct is divided into two distinct regions: entrance and fully developed region. Only the entrance region is analyzed, a generalized condition in which no mode of heating is specified is assumed at the entrance region. For each of the problem to be solved, the scale most representative of the appropriate equation was analyzed heuristically. The scale analysis was carried out manually while computer algorithm was developed to generate the result.

2. FORMULATION OF THE GOVERNING EQUATIONS

The physical model and cylindrical-polar coordinate (r,z,φ) system are shown in Fig. 1.

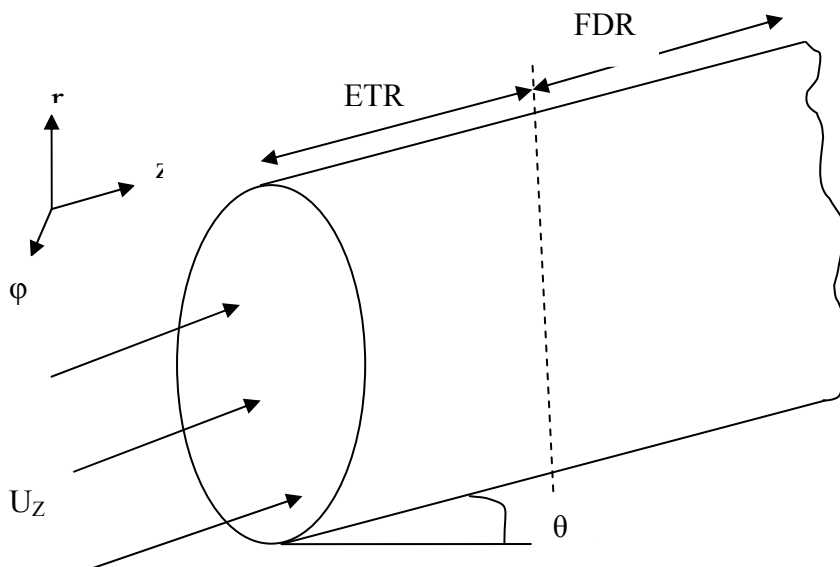


Fig. 1: The Physical Model and the Coordinate Axis

U_r , U_z and U_φ are the velocity components in r , z and φ - coordinates respectively. The working fluid is assumed Newtonian, incompressible with constant property. It is assumed that the velocity profile at the entrance is uniform and the working fluid is air. Effect of inclination is assumed to be negligible because of the potentiality of the flow which is likely to be very high at the entrance of the duct. However, the following specifications are made for the validity of the entrance formulae.

- (i) The boundary layer thickness, δ is far less than the characteristic length, L of the duct
 $\delta \ll L$
- (ii) The following scale of changes and order of proportionality are identified in axial and radial directions:
 $z \sim L$, $r \sim \delta$ and $U_z \sim U_\infty$
- (iii) For a conduit at the transition point,
 $\delta_h \sim \delta_t$ for $Pr \sim 1$,

(iv) At the point where the flow is hydrodynamically fully developed,

$$L \sim L_h,$$

(v) At the point of thermally developed fluid flow,

$$L \sim L_t.$$

The following equations govern the fluid flow and heat transfer in the elliptic pipe.

2.1 Continuity Equation:

For a steady state incompressible fluid flow,

$$\frac{\partial U_r}{\partial r} + \frac{U_r}{r} + \frac{\partial U_\phi}{r \partial \phi} + \frac{\partial U_z}{\partial z} = 0 \quad (1)$$

2.2. Momentum Transport Equations.

For constant velocity and density, the momentum equations for a steady flow in polar coordinate system are

Radial direction:

$$M_r = -\frac{\partial P'}{\rho \partial r} + \nu \left(\nabla^2 U_r - \frac{U_r}{r^2} - \frac{2 \partial U_\phi}{r^2 \partial \phi} \right) \quad (2)$$

Azimuthal direction:

$$M_\phi = -\frac{\partial P'}{\rho \partial \phi} + \nu \left(\nabla^2 U_\phi - \frac{U_\phi}{r^2} + \frac{2 \partial U_r}{r^2 \partial \phi} \right) \quad (3)$$

Axial direction:

$$M_z = -\frac{\partial P'}{\rho \partial z} + \nu \nabla^2 U_z \quad (4)$$

Where,

$$M_r = U_r \frac{\partial U_r}{\partial r} + \frac{U_\phi \partial U_r}{r \partial \phi} - \frac{U_\phi^2}{r}$$

$$M_\phi = U_r \frac{\partial U_\phi}{\partial r} + \frac{U_\phi \partial U_\phi}{r \partial \phi} - \frac{U_r U_\phi}{r}$$

$$M_z = U_r \frac{\partial U_z}{\partial r} + \frac{U_\phi \partial U_z}{r \partial \phi} + U_z \frac{\partial U_z}{\partial z}$$

$$\nabla^2 = \frac{\partial}{\partial r^2} + \frac{\partial}{r \partial r} + \frac{\partial^2}{r^2 \partial \phi^2} + \frac{\partial^2}{\partial z^2}$$

2.3 Energy Transport Equation

In the absence of energy source and viscous dissipation; if radiation is neglected, the energy transport equation for a steady flow is

$$U_r \frac{\partial T}{\partial r} + U_\phi \frac{\partial T}{r \partial \phi} - U_z \frac{\partial T}{\partial z} = \alpha \nabla^2 T \quad (5)$$

3 CONCEPT OF HYDRODYNAMIC AND THERMAL BOUNDARY LAYER

This analysis is of practical interest, particularly to the engineers. It establishes the hydrodynamic and thermal characteristics of fluid flow at the entry of conduits. Attention is focused on hydrodynamic and heat transfer results. The governing equations are intuitively scale to yield a generalized form of results under a generalized boundary constraint.

3.1. Hydrodynamic Analysis

The analysis will help to determine the hydrodynamic entrance length, L_h for flow inside conduits. This length is defined as the length required from the duct inlet to achieve a maximum velocity of 0.99 of the corresponding fully developed value. The scale analysis of the continuity equation (1) is:

Thus,

$$\frac{U_r}{\delta_h}, \frac{U_\phi}{\delta_h}, \frac{U_\infty}{L} = 0 \quad (6)$$

$$\frac{U_r}{\delta_h} \square \frac{U_\phi}{\delta_h} \square \frac{U_\infty}{L} \quad (7)$$

$\delta_h \sim r_h$ the hydraulic radius defined as

$$r_h = \frac{A^*}{P^*} \quad (8)$$

To complement the above scaling, the momentum equation (4) in the axial direction is also scaled to become,

$$\frac{U_r U_\infty}{\delta_h} \sim \frac{U_\phi U_\infty}{\delta_h} \sim \frac{U_\infty^2}{L} = \frac{P}{\rho L}, \nu \frac{U_\infty}{\delta_h^2}, \nu \frac{U_\infty}{L^2} \quad (9)$$

Where from equation (9),

$$\frac{U_\infty^2}{L} \sim \nu \frac{U_\infty}{\delta_h^2}, \text{ and } \frac{U_r U_\infty}{\delta_h} \sim \nu \frac{U_\infty}{L^2} \text{ and } P \sim P_\infty$$

Hence, the following relations can be deduced

$$\delta_h = L \text{Re}_L^{-1/2} \text{ and } U_r \sim U_\infty \text{Re}_L^{-3/2} \quad (10)$$

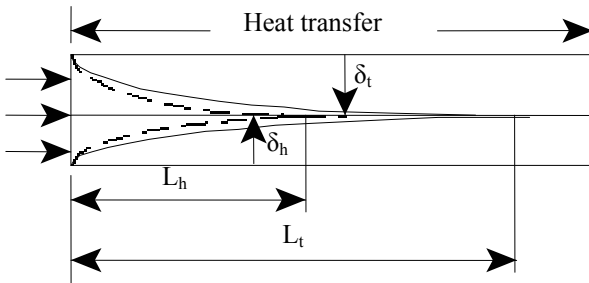


Fig.2: A typical sketch showing hydrodynamic and thermal entrance lengths

3.1.1 Estimation of Generalized Hydrodynamic Length

It is obtained from equation (10) that

$$\delta_h \sim L \text{Re}_L^{1/2} \quad (11)$$

Introducing the specified parameters and scale of changes into equation (11) yields

$$L_h' = \frac{1 - e^2}{4(1 + \sqrt{1 - e^2})} \sim \frac{L_h}{\text{Re}_D D_h} \quad (12)$$

Where,

$$a^2 - b^2 = a^2 e^2$$

$$\delta_h = \frac{a \sqrt{1 - e^2}}{1 + \sqrt{1 - e^2}}, \quad V_r = \frac{U_r}{U_\infty}$$

The generalized hydrodynamic boundary layer is

$$\delta_h' = \frac{\delta_h}{a} = \frac{\sqrt{1 - e^2}}{1 + \sqrt{1 - e^2}} \quad (13)$$

L_h' , δ_h' , and V_r are the generalized non-dimensional hydrodynamic entrance length, hydrodynamic boundary layer thickness and radial velocity respectively.

3.1.2 Generalized Friction Coefficient

The scale most representative of shear stress equation,

$$\tau = \mu \frac{\partial u}{\partial r}, \text{ is}$$

$$\tau \sim \frac{\rho U_\infty V}{\delta_h} \quad (14)$$

Introducing the appropriate scale of changes gives a generalized form of hydrodynamic characteristic of the duct flow as

$$f' \operatorname{Re} = \frac{8(1 + \sqrt{1 - e^2})}{\sqrt{1 - e^2}} \quad (15)$$

Where,

$$f' \sim \frac{\tau}{\frac{1}{2} \rho U_{\infty}}$$

3.1.3 Generalized Static Pressure Distribution

The axial pressure drop in the entrance region of a horizontal elliptic pipe is obtained from momentum equation in the axial direction. The scaling of the equation yields

$$\frac{U_{\infty}^2}{L} \sim -\frac{1}{\rho} \frac{dP}{L} \quad (16)$$

The generalized pressure drop is obtained as

$$\frac{dP}{L} \sim \frac{1/2 \rho U_{\infty}^2}{\operatorname{Re}_D D_h} \quad (17)$$

where, $dP = P_{\infty} - P_{Lh}$

Equation (17) indicates that the pressure gradient is maximum at the entrance of the pipe and decreases monotonically with downstream distance until it reaches a constant value. The equation also shows that the pressure drop dP increases with axial distance and inversely proportional to Reynolds number, Re_D .

3.2 Concept of Thermal Boundary Layer

The analysis presents a well defined equation for generalized thermal entrance length, L_t' and Nusselt number, Nu' at the end of major and minor axes of the ellipse. The scheme employs the energy transport equation for the derivation of the equations.

3.2.1 Evaluation of Thermal Entrance Length

For the energy transport equation (5), the scale analysis is,

$$\frac{U_r \Delta T}{\delta_t}, \frac{U_{\phi} \Delta T}{\delta_t}, \frac{U_{\infty} \Delta T}{L} \sim K_{\alpha} \quad (18)$$

Where,

$$K_{\alpha} = \alpha \left[\frac{\Delta T}{\delta_t^2}, \frac{\Delta T}{\delta_t^2}, \frac{\Delta T}{L^2} \right]$$

Thus, the scale most representative of equation (18) is

$$\frac{U_{\infty} \Delta T}{L} \sim \alpha \frac{\Delta T}{\delta_t^2} \quad (19)$$

From equation (19), it is derived that the generalized entrance length is

$$L_t' \sim \frac{L_t}{D \operatorname{Re} \operatorname{Pr}} \sim \frac{1 - e^2}{(1 + \sqrt{1 - e^2})^2} \quad (20)$$

L_t is local thermal entrance length.

3.2.2 Evaluation of generalized Mean Nusselt number

Nusselt number is a non dimensional parameter indicative of the ratio of energy convection to conduction.

Nusselt number at the end of Major Axis

The fundamental equation for Nusselt number is

$$NuD = \frac{hD}{K} \quad (21)$$

where h is convective heat transfer coefficient. It is given as

$$h = \frac{K}{\delta_t} \quad (22)$$

The generalized Nusselt number at the end of major axis is obtained as,

$$NuD \sim \frac{2(1 + \sqrt{1 - e^2})}{\sqrt{1 - e^2}} \quad (23)$$

Nusselt number at the end of Minor Axis

Recall equation (21), and express as

$$NuB \sim \frac{D}{\delta_m} \quad (24)$$

In this case, δ_m is the thermal boundary layer thickness along the minor axis. Fig. 3 is considered for continuity of the boundary layer thickness.

$$\delta_{mj} = \delta_{mn} + \delta_{tz} \quad (25)$$

For continuity of the boundary layer thickness, the following expression is employed:

$$\frac{\delta_{mn}}{\delta_{mj}} \delta_{mj} \sim \delta_{tB} \quad (26)$$

Where δ_{tB} is the minor thermal boundary layer thickness at the transition point.

The Nusselt number at the end of minor axis is

$$NuB = \frac{2(1 + \sqrt{1 - e^2})}{1 - e^2} \quad (27)$$

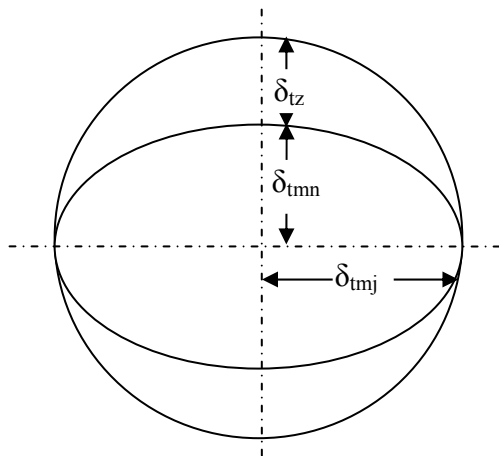


Fig.3: Enlarged Section of the Duct

4. RESULTS AND DISCUSSION

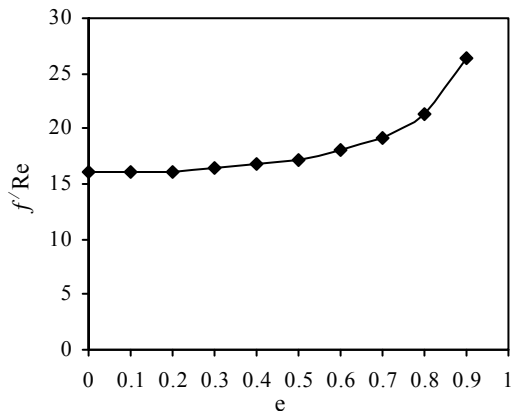


Fig. 4 Effects of eccentricity of the ellipse on f/Re

Fig. 4 shows the variation of hydrodynamic characteristic of the duct flow, f/Re with eccentricity. It is observed that f/Re increases with eccentricity, and $f/Re = 16$ for $e = 0$, which corresponds to a circular geometry, compares well with those published in literatures.

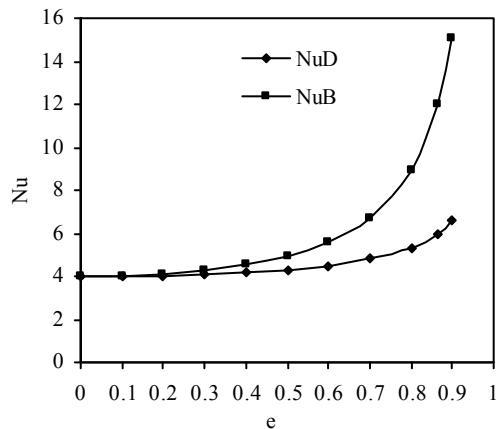


Fig. 5 Nusselt number at the end of major and minor axes

Fig.5 shows the relationship between Nusselt number and eccentricity of the ellipse at the end the minor and major axes. It is noticed in the plots that for $0 \leq e \leq 0.2$, the difference between the heat transfer rate at the end of major and minor axes is insignificant. Above $e = 0.2$, more heat is transferred from the end of minor axis. It is also noticed that the higher the value of eccentricity, e , the higher the difference between NuB and NuD for a given eccentricity. A critical eccentricity, $e=0.866$, is obtained for optimum heat transfer by the use of mathematical analysis in combination with the results obtained from the plots.

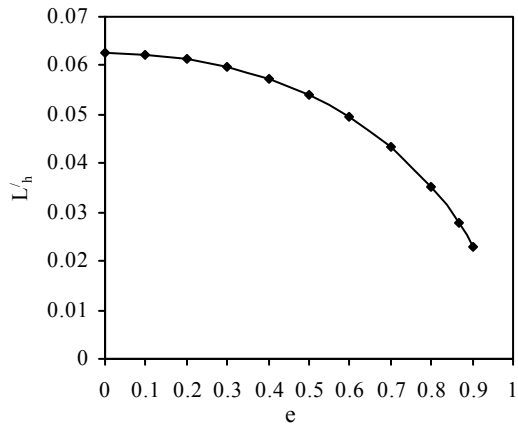


Fig. 6 Hydrodynamic entrance lengths for various eccentricities

Effect of eccentricity on hydrodynamic entrance length is given in Fig.6. The figure shows that the entrance length reduces with increasing value of eccentricity. The present generalized hydrodynamic entrance length 0.0277 lies within the values obtained by McComas (0.02447) and Abdel-Waheed (0.0345) for the same elliptic geometry of $e=0.866$.

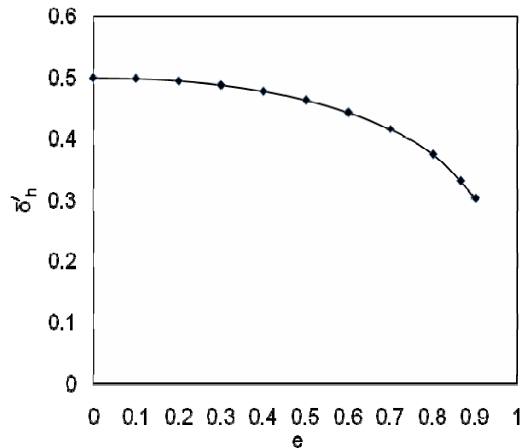


Fig. 7 Effect of eccentricity on hydrodynamic boundary layer thickness

Variation of hydrodynamic boundary layer thickness, δ'_h with eccentricity, e is shown in Fig.7. It shows that at the points of transition to fully developed flow, δ'_h reduces with increase in e .

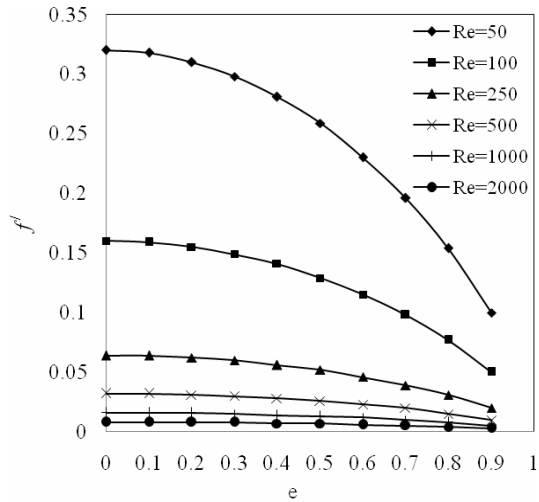


Fig. 8 Influence of eccentricity on friction for various Reynold's numbers

Fig.8 shows that the generalized friction values f' reduces with increase in e and Re . Also, towards $Re = 2000$ the plots becomes flattened which is an indication that as Re tends towards transition from laminar to turbulent flow, f' becomes almost a constant.

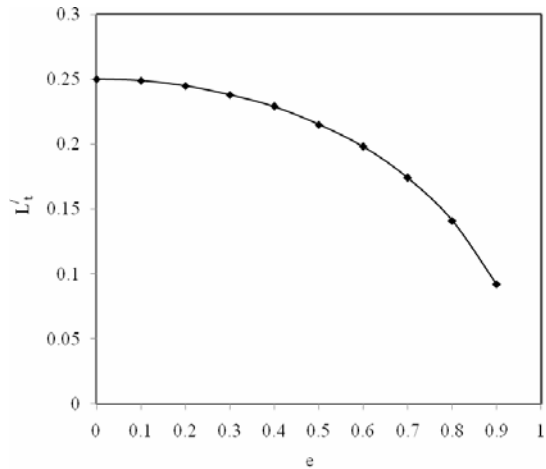


Fig. 9 Variation of thermal entrance length with eccentricity

Fig.9 depict that thermal entrance length and eccentricity are inversely related, with L'_t reduces with e .

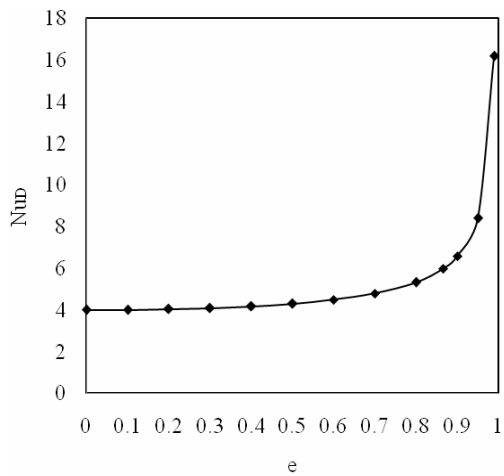


Fig. 10 Nusselt number at the end of major axes

Fig.10 shows a gradual increase in Nusselt number with increasing eccentricity. Above 0.866, that is, towards the collapse of the duct, heat transfer is not by convection alone, conduction plays its own part, and that is why there is sudden rise in the Nusselt number. Therefore 0.866 is the critical value for optimum heat transfer by convection.

CONCLUDING REMARKS

- Scale analysis has been found suitable method for solution of entrance problems.
- Generalized Nusselt numbers are independent of fluid properties. They depend solely on eccentricity of the duct.
- A critical eccentricity, $e = 0.866$, is attained for optimum heat transfer by convection.
- Mathematical expression to relate hydrodynamic characteristic of the duct flow and Nusselt number had been developed.

$$NuD = 0.25 f' Re$$

$$NuB = \frac{1}{\sqrt{1-e^2}} f' Re$$

- The relationship between NuD and NuB has also been established:

$$NuD = 0.25 \sqrt{1-e^2} NuB$$

Nomenclatures

- a Semi major axis of the ellipse
- A* Cross sectional area
- B Semi minor axis of the ellipse
- B Minor diameter
- C_p Specific Heat Capacity at constant pressure (J / kgK)

D_h	Hydraulic Diameter
D	Major Diameter
e	Eccentricity of ellipse
ETR	Entrance region
$F(r)$	Body force component in radial direction
$F(\phi)$	Body force in θ direction
$F(z)$	Body force component in the axial direction
FDR	Fully developed region
g	Acceleration due to gravity (m/s^2)
h	Convective heat transfer coefficient
K	Thermal conductivity of the working fluid
L	Characteristic Length
L_h	Local hydrodynamic entrance length
LHS	Left hand side
L_t	Local thermal entrance length
NuB	Nusselt number at the end of minor axis
NuD	Nusselt number at the end of major axis
\bar{p}	Average pressure over the duct cross section
p'	The small pressure variation governing the flow distribution in the cross stream plane
Pr	Prandtl number, ν/a
P^*	Wetted perimeter
Re	Reynolds number
RHS	Right hand side
T	Dimensional fluid temperature
U_r	Dimensional velocity in radial direction
U_ϕ	Dimensional velocity in azimuthal direction
U_z	Dimensional velocity in z direction
V_r	Normalized cross flow velocity
Z	Coordinate in the direction of flow (axial direction)

Greek Symbol

α	Thermal diffusivity (m^2/s)
β	Coefficient of thermal expansion
δ_h	Local hydrodynamic boundary layer thickness
δ_t	Local thermal boundary layer thickness
λ	Angle of inclination

ν Kinematic viscosity of the fluid m^2 / s
 ρ Density, kg / m^3

Subscripts:

h Hydrodynamic
t Thermal

REFERENCES

1. Horneck, R.W., (1964), Laminar Flow in the Entrance Region of a Pipe, Appl. Sci. Res., Vol. 13, pp.224-232.
2. Shah, R.K., (1975), Thermal Entry Length Solutions for a Circular Tube and Parallel Plate Proc. Nat. Heat Mass Transfer Conf., 3rd Indian Ins. Technol. Bombay, Vol. 1 HMT-11-75
3. Wiginton, C.L. and Dolton, C., (1970), Incompressible Laminar Flow in the Entrance Region of a Rectangular Duct, J., Appl. Mech., Vol. 37, pp. 854-856.
4. Abdel-Wahed, R.M., Attia, A.E. and Hifni, M.A., (1984), Experiments on Laminar Flow and Heat Transfer in an Elliptic Duct, International Journal of Heat and Mass Transfer, Vol.27, pp.2394-2411.
5. Webb. A.K, (1982), Entrance Region Heat Transfer, International Journal of Mechanical Engineering Education, Vol. 10, pp. 15-25.
6. Kutcher, C.F. Christensen, C.B. and Baker, C.M, (1993), Unglazed Transpire Solar Collectors, Heat Loss Theory, ASME Journal of Solar Energy Engineering, Vol. 115, pp182-188
7. Kutcher, C.F., (1994). Heat Exchange Effectiveness and Pressure Drop for Air Through Perforated Plates With or Without Cross Wind, ASME Journal of Heat Transfer, Vol. 116, pp.391-399
8. Parakash, C. and Ye-Deiliu, (1985), Analysis of Laminar Flow and Heat Transfer in Entrance Region of an Internally Finned Circular Duct, Journal of Heat Transfer, Vol. 104, pp.670-677.
9. Bello-Ochende, F.L., Adegun, I.K., (2004), Scale Analysis of Laminar Forced Convection within the Entrance of Heated Regular Polygonal Tubes, Journal of Mathematical Association of Nigeria(ABACUS), Vol.31, No. 2A, pp. 28-41.
10. Adegun, I.K, (2007), Analytical Study of Fluid Flow and Heat Transfer in the Entrance Region of Heated Concentric Elliptic Annuli, Journal of Research Information in Civil Engineering, Vol.4, No.1, pp.68-85
11. Bello-Ochende, F.L. and Adegun, I.K., (1993), A Perturbation Analysis of Combined Free and Forced Laminar Convection in Tilted Elliptic Cylinders, 6th International Symposium on Transport Phenomena in Thermal Engineering, Seoul, Korea, Vol. iii, pp. 121-125.
12. Necati Ozisiki, M, (1985), Heat Transfer, A Basic Approach, New York: Mc Graw Hill, Publishing Company.

2/12/2009

Enhancement Of Thermal Capabilities Of A Solar Concentrator

I. O. Ohijeagbon¹, A. S. Adekunle², and O.D. Awolaran

^{1&2}Department of Mechanical Engineering, University of Ilorin, P. M B 1515, Ilorin, Nigeria

¹idehaiohi@yahoo.com

ABSTRACT

In order to continue to explore the enormous potential of solar energy as a veritable source of energy, physical constraints inherent in science and technological must steadily be converted to advantageous concepts and processes. This study investigates methods for enhancing thermal capabilities of a parabolic dish solar collector or concentrator. Optical lenses of different focal lengths and diameters were utilised to determine various output characteristics of thermal radiation. Convergent temperature (T_c), rate of energy emitted (q), and intensity of radiation (i_n) were found to increase with steady increase in ambient temperature (T_a). Larger diameter lenses and shorter focal length lenses were more advantageous than smaller diameter lenses and longer focal length lenses in producing higher thermal outputs respectively. It was further observed that actual drop in thermal outputs are obtained with lenses of 15 and 30 cm focal lengths compared with no-lens condition at upward of 31 °C of ambient temperature. Also, the farther away the temperatures measured, the lower the thermal output temperature. This was as a result of radiation effects from the collector which influenced the output temperatures around the lenses. The study therefore concluded that enhanced thermal capabilities of solar energy devices operating on thermal radiations could be achieved by this method. [New York Science Journal. 2009;2(3):72-78]. (ISSN: 1554-0200).

Keywords: thermal capabilities, concentrator, optical lenses, converged temperature, rate of energy emitted, and intensity of radiation

1. INTRODUCTION

In view of increasing interest of finding enhanced and effective temperature output and thermal capabilities of solar energy radiations, which is described by Adegoke and Bolaji (2000) as the most attractive energy source for the future; this work is intended to further corroborate various existing methods and applications of solar energy devices operating on principles of thermal radiations. Many areas of applications of solar energy devices such as, solar cooker, solar furnaces, cooling of building, solar water and air heating, solar drying, among others, show that obviously, the availability of solar energy that have lend to very useful researches, which have continued to show that it is a safe and environmentally friendly source of energy in enhancing and transforming hitherto traditional techniques to modern scientific methods on energy utilisation and applications (Mc Veigh, 1977, Adegoke, 1998, Pelemo et al., 2002). Solar radiation does not contaminate environment or endanger ecological balance. It avoids major problems like exploration, extraction and transportation (Rajput, 2006). More so that mankind and especially engineering is today facing one of the most severe challenges ever. Present energy engineering leads to resource depletion and environmental destruction. Thus we need to develop energy engineering in harmony with nature (Wall, 2002).

Being a free gift of nature, solar energy is in most abundant supply compared with other naturally existing forms of energy such as fossil fuel, coal, oil and natural gas which are fast depleting due to increased global dependence on energy (Richard, 1984); hence more effective methods of exploring its use should be encouraged. Solar energy is not only inexhaustible, it is non-polluting and therefore can be utilised to provide all our energy needs (Richard, 1977). The finiteness of the fossil-fuel-based sources of energy has brought home to mankind the stark reality of the need to develop other sources of energy. Hence, an upsurge of small and large scale renewable energy programmes all over the world (Bamiro, 1983).

The enormous potential of solar energy as a veritable source of energy is in no doubt, however, its effective exploration and utilisation is determined by the extent and limitations that science and technological advances may allow. Although the total amount of energy is enormous, the collection and conversion of solar energy into useful forms must be carried out over a large area which entails a large capital investment (Rajput, 2006). In the past, the exploitation of solar energy reaching the earth's surface as a viable alternative energy source has been pursued vigorously through the development of different solar powered systems with varying degrees of efficiencies (Pelemo et al., 2002).

This study therefore is aimed at investigating methods of enhancement of thermal capabilities of a parabolic dish solar collector or concentrator. The process involves the use of optical lenses of different focal lengths and diameters to determine the output characteristics of temperature, rate of energy emitted, and intensity of radiation respectively. Improvements in thermal capabilities as a result of implementation of the optical lenses will lead to very useful information and optimised processes of solar energy devices operating on thermal radiations.

2. THEORETICAL FRAMEWORK

According to Rogers and Mayhew (1992), the framework for establishing the total energy emission per unit time by unit area of a surface and also for the intensity of radiation of a surface is hereby given.

The total energy emitted per unit time by unit area of a black surface is proportional to the 4th power of the absolute temperature T. This relation is expressed by the Stefan-Boltzmann law:

$$q_b = \sigma T^4 \quad (1)$$

where, σ = Stefan-Boltzmann constant = 56.7×10^{-12} KW/m²K⁴

The spatial distribution of energy emission from an element can be represented as follows:

$$dQ_{bn} = i_n dw_n dA \quad (2)$$

$$dQ_{b\phi} = i_\phi dw_\phi dA \quad (3)$$

where, dQ_{bn} is the rate of flow of energy through dA_1 and $dQ_{b\phi}$ is the rate of flow of energy through dA_2 .

i_n is the intensity of radiation in the normal direction and i_ϕ is the intensity of radiation in the ϕ direction.

The spatial distribution of i_ϕ is expressed by Lambert's cosine law:

$$i_\phi = i_n \cos \phi \quad (4)$$

Combination of equations (3) and (4) gives:

$$dQ_{b\phi} = i_n \cos \phi dw_\phi dA \quad (5)$$

The solution of equation (5) gives:

$$Q_b = i_n \pi dA \quad (6)$$

Equation (1) can be re-written as:

$$Q_b = \sigma T^4 dA \quad (7)$$

Combination of equations (6) and (7) gives:

$$i_n = \frac{\sigma T^4}{\pi} \quad (8)$$

This equation, giving the intensity of normal black radiation, is a consequence of the Stefan-Boltzmann law and Lambert's law.

Therefore for a grey body the following laws are valid:

$$q = \epsilon q_b = \epsilon \sigma T^4 \quad (9)$$

$$i_n = \frac{\varepsilon \sigma T^4}{\pi} \quad (10)$$

where ε = total hemispherical emissivity or simply emissivity, and is defined as the ratio of the total energy q emitted by a surface to the total energy q_b emitted by a black surface at the same temperature.

Thus,
$$\varepsilon = \left(\frac{q}{q_b} \right)_T \quad (11)$$

The ratio of the total hemispherical emissivity to the normal emissivity $\frac{\varepsilon}{\varepsilon_n}$ is equal to unity for a grey body. Assuming a glass as a silver polished surface, its normal emissivity ε_n is given as 0.02 (Rogers and Mayhew, 1992). Hence, $\varepsilon = \varepsilon_n$ for a grey body. Equations (9) and (10) are respectively used to analyse the experimental data collected.

3. MATERIALS AND METHODS

3.1 Conditions and Materials

The major equipment used to carry out this research study is a focusing type solar collector or concentrator. This collector was previously constructed by Gbodiyan and modified for better performance by Abiola (Gbodiyan, 2003, Abiola, 2003), and then used by Awolaran for research studies (Awolaran, 2005). The surface area of the collector surface is 1.1314 m² with an estimated focal length of 69 cm, obtained as a cumulative value from the pieces of mirrors attached to the collector surface.

The geographical location of Ilorin, Nigeria where the study was conducted is estimated as Latitude: 8.43 °N, Longitude: 4.5 °E and Altitude: 366m, percentage annual average of actual to theoretical hours of sunshine in a day: $\frac{n}{N} = 53$, where, n = actual hours of sunshine in a day, N = theoretical maximum possible sunshine hours in a day, solar irradiance: 640 (Fagbenle, 1990, NMA, 2005).

Three thermometers were used (0-45)⁰C, (0-100)⁰C and (0-350)⁰C respectively. Four converging lenses with the following specifications were used; 10 cm focal length lens (5 cm in diameter), 15 cm focal length lens (5 cm in diameter), 30 cm focal length lens (5cm in diameter) and 15 cm focal length lens (10 cm in diameter) respectively. The lenses were used to investigate the effects of the lens' focal length and diameter respectively on the thermal output of the concentrator. A stop watch was used to time and monitor temperature changes within specific time-intervals during the experimental investigation.

3.2 Methods

The concentrator solar device without the use of lenses was positioned to ensure no shading effect and to guarantee a maximum radiation from the sun, between the hours of 12.00 noon and 2.00 pm when the experiment was conducted. During this period it was assumed that the sun radiation is at its peak. The concentrator laced was also placed so that the angle between the rays of the sun and the collector axis is minimised in order to obtain the maximum solar irradiance, that is, the total radiation incident on unit area of surface per unit time (Rogers and Mayhew, 1992). This was accomplished by making sure the shadow of the concentrator on the ground forms approximately a perfect circle and radiation rays approximately at a normal angle to the concentrator surface.

The (0-350)⁰C thermometer was placed at the region of convergence of the concentrator to measure the air temperature (T_c) at converging point. The (0-45)⁰C thermometer was placed at a distance of about 3 meters away from the concentrator system in order to measure the ambient air temperature (T_a) without undue interference or influences. The setting up of the apparatus was done 30 minutes before the commencement of taking the readings, so that the apparatus will adapt to the ambient state. The readings of T_a and T_c were taken and recorded at 10 minutes interval between the hours of 12.00 noon and 2.00 pm for Day 1, without the use of any lens. The entire procedure was repeated for Days 2, 3 and 4 respectively,

fixing the converging lenses of different focal lengths at the region of convergence of the solar concentrator in order to investigate the effects of focal lengths of lenses on convergent temperatures. Therefore the (0-350)^oC thermometer was now placed at the new region of convergence of the lenses, to measure the temperature (T_c) at the new focal point.

All the above procedure was repeated for 3 more weeks to get a better view of the variations of the parameters over time. Lenses of different surface areas/diameters was then used on the forth week respectively for another 3 days each to study the effects of lenses dimensions on convergent temperatures accordingly.

4. DISCUSSION OF RESULTS

4.1 Effects of Lenses Focal Length on Radiation Output Characteristics

Table 1: average ambient and convergent temperatures of concentrator-using lenses with different focal lengths below shows the data collected for the ambient and convergent temperatures of the concentrator (Awolaran, 2005). These being the average values over a 3 weeks period, that is 29th August 2005 to 1st September 2005, 5th September 2005 to 8th September 2005, and 12th September 2005 to 15th September 2005 respectively. The data is for no lens condition and with lenses of 10 cm, 15cm and 30 cm focal lengths respectively with each of the lens been 5 cm in diameter.

The output characteristics of solar radiation indicates a consistent increasing temperature (T_c) of converged radiations with time with respect to increasing ambient temperatures (T_a) as shown in table 1, and figure 1: variation of energy emitted with time for different focal lengths of lenses respectively. Consequently, the rate of energy emitted (q), and intensity of radiation (i_n) given by equations (9) and (10) would also increase correspondingly with the exception of the ambient values which appears constant.

Figure 1 further reveals that higher thermal output characteristics are achievable with lens of shorter focal length of 10 cm compared with 15 and 30 cm lenses. It should however be noted that actual drop in thermal outputs are obtained with lenses of 15 and 30 cm focal lengths compared with no-lens condition at upward of 31 ^oC of ambient temperature; this situation further reveals that the farther away the temperatures observed and measured from the primary solar collector at some significant point in the ambient temperature, the lower would be the thermal outputs with further increasing ambient temperatures. Hence, it can be deduced that thermal and radiation measurements through the lenses is also partly influenced by radiation effects from the collector.

4.2 Effects of Lenses Diameter on Radiation Output Characteristics

Table 2: average ambient and convergent temperatures of concentrator-using lenses with different diameters and Focal Lengths = 15 cm as shown below, the data collected is for the ambient and convergent temperatures of the concentrator for lenses of 5 and 10 cm diameter respectively (Awolaran, 2005); with each of the lens been 15 cm focal length. These being the average value of 3 days readings each for each lens. That is 31st August 2005, 7th September 2005 and 14th September 2005 for the 5 cm diameter lens, and 30th September 2005, 1st October 2005 and 3rd October 2005 for the 10 cm diameter lens respectively.

In addition to increasing convergent temperatures with respect time and increasing ambient temperatures as shown in table 2, figure 2: variation of energy emitted with time for different lenses diameters also reveals that appreciable gain can be achieved in the rate of energy emitted (q), and intensity of radiation (i_n) if an increased diameter lens is utilised in solar collector devices. Figure 2 also indicates equivalent values of the rate of energy emitted (q) for ambient measurement of both lenses, as their curves overlap one another.

5. CONCLUSION

From the results, the study shows that enhancement of thermal capabilities of a solar concentrator is achievable through the use of converging lenses. Larger diameter lenses should be preferred over smaller diameter ones as this will permit more radiation to be captured. And shorter focal lengths are more advantageous than longer focal lengths, as a result, allowing the converged radiation closer to the collector surface which is also influenced by thermal radiations from the solar collector itself. Hence, improved and

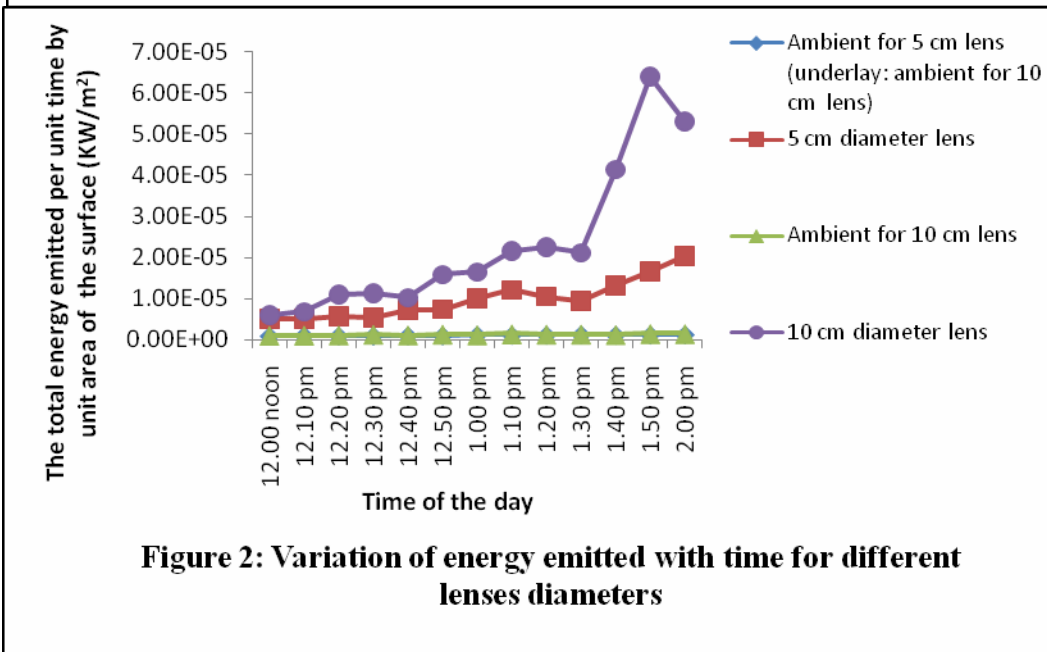
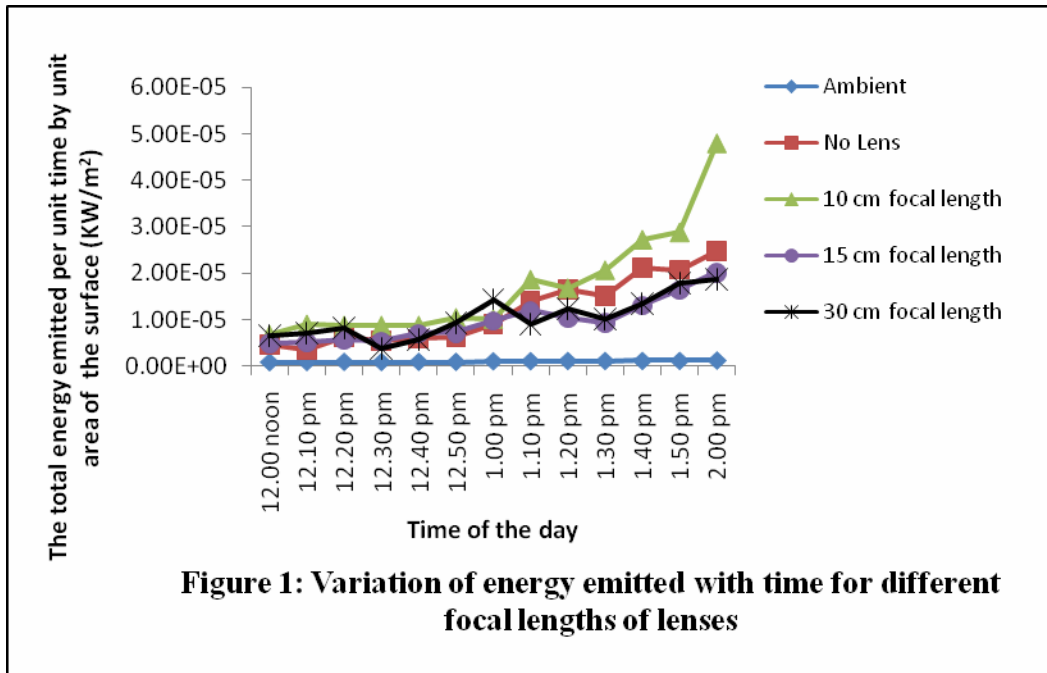
optimised output characteristics of temperature, rate of energy emitted, and intensity of radiation respectively could be achieved and employed for better performances of solar energy devices operating on thermal radiations.

Table 1: Average Ambient and Convergent Temperatures of Concentrator-Using Lenses with Different Focal Lengths

Time	Average Ambient Temperature, T_a ($^{\circ}\text{C}$)	Average Convergent Temperature, T_c ($^{\circ}\text{C}$)			
		With No Lens	With Lenses Diameters = 5 cm		
			10 cm Focal Length	15 cm Focal Length	30 cm Focal Length
12.00 noon	29.50	45.00	49.33	45.67	49.33
12.10 pm	30.00	41.67	53.00	46.00	50.33
12.20 pm	30.17	48.33	52.67	47.33	52.00
12.30 pm	29.92	46.67	52.67	46.67	43.00
12.40 pm	30.17	47.67	52.67	50.00	47.67
12.50 pm	30.25	48.33	55.00	50.33	53.67
1.00 pm	31.17	53.00	54.67	54.33	59.67
1.10 pm	31.33	59.33	63.67	57.00	53.33
1.20 pm	31.67	61.67	62.00	55.00	57.33
1.30 pm	31.67	60.33	65.33	53.67	54.67
1.40 pm	31.75	65.67	70.00	58.33	58.67
1.50 pm	31.83	65.33	71.00	61.67	63.00
2.00 pm	32.33	68.33	80.67	65.00	63.67

Table 2: Average Ambient and Convergent Temperatures of Concentrator-Using Lenses with Different Diameters and Focal Lengths = 15 cm

Time	Average Values of Temperature			
	5 cm Diameter Lens		10 cm Diameter Lens	
	Ambient Temperature, T_a ($^{\circ}\text{C}$)	Convergent Temperature, T_c ($^{\circ}\text{C}$)	Ambient Temperature, T_a ($^{\circ}\text{C}$)	Convergent Temperature, T_c ($^{\circ}\text{C}$)
12.00 noon	29.33	45.67	31.00	47.67
12.10 pm	30.33	46.00	31.33	49.33
12.20 pm	29.67	47.33	31.67	55.67
12.30 pm	29.67	46.67	32.67	56.00
12.40 pm	30.00	50.00	31.67	54.67
12.50 pm	30.00	50.33	33.00	61.00
1.00 pm	31.33	54.33	32.00	61.67
1.10 pm	31.00	57.00	33.33	66.00
1.20 pm	31.33	55.00	33.00	66.67
1.30 pm	32.00	53.67	33.00	65.67
1.40 pm	31.33	58.33	32.33	77.67
1.50 pm	31.67	61.67	33.67	86.67
2.00 pm	32.00	65.00	33.67	82.67



6. REFERENCES

Abiola, A. O. (2003), Temperature Magnification and Applications of a Parabolic Solar Energy Collector, B. Eng. Thesis, Department of Mechanical Engineering, University of Ilorin, Ilorin, Nigeria.
 Adegoke, C. O. (1998), Alternative Energy Option for Nigeria as a Reaction to Impending Global Climate Change, Journal of Science, Engineering and Technology, Vol. 5(3), pp1341-1348.

- Adegoke, C. O. and Bolaji, B. O. (2000)**, Performance Evaluation of Solar-Operated Thermosyphon Hot Water System in Akure, International Journal of Engineering and Engineering Technology, School of Engineering and Engineering Technology, Akure, Nigeria, Vol. 5(1), pp35-40.
- Awolaran, O. D. (2005)**, Investigation of Methods of Increasing Temperature of a Parabolic Solar Energy Collector, B. Eng. Thesis, Department of Mechanical Engineering, University of Ilorin, Ilorin, Nigeria.
- Bamiro, O. A. (1983)**, Empirical Relations for the Determination of Solar Radiation in Ibadan, Nigeria, Solar Energy, Pergamon Press Ltd., UK., Vol. 31(1), pp85-94.
- Fagbenle, R. L. (1990)**, Estimation of Total Solar Radiation in Nigeria Using Meteorological Data, Nigerian Journal of Renewable Energy, Vol. 1, pp1-10.
- Gbodiyan, M. F. (2003)**, Design and Construction of a Solar Steam Producer, B. Eng. Thesis, Department of Mechanical Engineering, University of Ilorin, Ilorin, Nigeria.
- Mc Veigh, J. C. (1977)**, Sun Power, An Introduction to Application of Solar Energy, Pergamon Press, London.
- Nigerian Meteorological Agency (NMA, @ 2005)**, Record of Climatic Conditions in Ilorin (September 2002-August 2005), Federal Airport Authority, Ilorin, Nigeria.
- Pelemo, D. A., Fasasi, M. K., Owolabi, S. A., and Shaniyi, J. A. (2002)**, Effective Utilisation of Solar Energy for Cooking, NJEM, Vol. 3(1), pp13-18.
- Rajput, R. K. (2006)**, Thermal Engineering, Laxmi Publications (P) Ltd., New Delhi.
- Richard, C. D. (1984)**, Energy Resources and policies, Academic Press, New York.
- Richard, J. W. (1977)**, Solar Energy Technology and Application, Ann Arbor Science, New York.
- Rogers, G. F. C. and Mayhew, Y. R. (1992)**, Engineering Thermodynamics-Work and Heat Transfer, Longman Group, UK. Ltd.
- Wall Goran (2002)**, Conditions and Tools In the Design of Energy Conversion and Management Systems of a Sustainable Society, Energy Conversion and Management Vol. 43, pp1235-1248, www.elsevier.com/locate/enconman

2/13/2009

对宇宙起源的新观念和新的完整论证:宇宙不可能诞生于奇点 (下篇) ***

== 我们宇宙诞生于大量原初最小黑洞($M_{\text{bm}} \approx 10^{-5}\text{g}$)的合并, 而不是“奇点”或“奇点的大爆炸” ==

张洞生

Dongsheng Zhang

1/10/2009

1957年毕业于北京航空学院,即现在的北京航空航天大学
永久住址: 17 Pontiac Road, West Hartford, CT 06117-2129, U.S.A.
E-mail: ZhangDS12@hotmail.com

====Part II: Our Universe Was Originated From The Big Bang Caused By The Amalgamations of
a Great Amount of the Original Minimum Schwarzcuild Black Holes (MSBH,its mass $M_{\text{bm}} \approx 10^{-5}\text{g}$),
But Not From Singularity or Not From The Big Bang of Singularity =====

Abstract: In this article, According to the principle of the time mirror reversion or the time symmetry, based on some general laws of astronomy, physics and many classical theories, the calculated results could prove that our Pre-universe in its last great collapse had a Big Crunch and then started to turn into the Big Bing which was caused by the amalgamations of a great amount of the original minimum Schwarzcuild black holes (MSBH, $M_{\text{bm}} \approx 10^{-5}\text{g}$). Therefore, Our present expanding Universe was impossible to be born from Singularity or from the Big Bang of Singularity but from the Big Crunch of Pre-universe. [New York Science Journal. 2009;2(3):79-100]. (ISSN: 1554-0200).

Keywords: Universe; Big Bang; Black Holes; Singularity

In this article, formula (3c) is the most important one newly derived by author. Once Pre-universe collapsed to $t \leq [k_1 (2G\kappa)/C^5]^{2/3}(3c)$, i.e. $t = -0.5563 \times 10^{-43}\text{s}$, and $T = 0.734 \times 10^{32}\text{k}$, every particle m in the Pre-universe simultaneously entered into three states: every energy-particle m would simultaneously break off its gravitational linkage between the closest neighbors, every particle m would exactly become a minimum Schwarzcuild black hole(MSBH, its mass $M_{\text{bm}} \approx 10^{-5}\text{g}$), and every particle m entered to Plank's Era to became equal to Plank particle m_p ; so, at that time, $m = M_{\text{bm}} = m_p = 1.058 \times 10^{-5}\text{g}$ (5j). The explosion, disintegration and disappearance of every m with Pre-universe together in the Plank's Era led by above 3 states could directly and jointly obstructed the further collapse of Pre-universe into Singularity. After that, owing to a little reduction and difference of temperature and density in the Universe Package, the energy-particles of little higher density would grow up to become the little bigger new-born MSBHs out of Plank Era. The collisions and combinations of all new-born MSBHs everywhere in the Universe Package would cause and form the "Big Bang" and "Original Inflation". It was the genesis of our present Universe. The whole process changed from the disappearance of Pre-universe into Plank's Era and the genesis of new Universe out from Plank's Era (Time) was a irreversible process of phase transition from the collapse to the expansion.

The heart of the matter in this article is to confirm that our Universe would be a real universal black hole (UBH), it was born from a great amount of MSBHs, now it is a real giant BH, and its final destiny will contract to become two MSBHs and vanish in Planck Era.^{<10>} Thus, all knotty problems in the universal origin and evolution could be simplified into the problems of the expansion or contraction of BHs. As we know, every BH would be the simplest material object

in the Universe,^{<10>} and have the simplest laws between the parameters on its Event Horizon. Therefore, the most complicated equations of General Theory of Relativity and its solutions can be disregarded in this article. Other important conclusions can be proved too in this article, such as, the Universe is a real giant BH, the new demonstrations of the Original Inflation, the expansion or contraction of the Universe will not be decided by the real universal density ρ_r but decided by the total amount of the final universal energy-matters, etc.

笛卡儿：“我们不能依赖他人的权威而接受真理，必须自己寻求。”

内容摘要：根据近代宇宙天文学和物理学的一些基本规律和公式,通过计算所得的数据,证明了我们现在膨胀的宇宙不可能诞生于“奇点”或“奇点的大爆炸”,而是从前辈宇宙的“大塌缩”而来。(3c)式是本文中重新推导出来的最重要的公式,一旦前辈宇宙大塌缩到(3c), $t \leq [k_1 (2Gk)/C^5]^{2/3}$, 即 $t = -0.5563 \times 10^{-43}$ s 秒和宇宙最高温度 $T=0.734 \times 10^{32}$ k 时, 前辈宇宙中的每个能量-物质粒子 m 同时进入 3 种状态: 每个粒子 m 都与其相邻的粒子因无足够时间传递引力而失去了引力联系,每个 m 都变成 $M_{bm} \approx 10^{-5}$ g 史瓦西最小黑洞,同时进入普朗克领域而成为普朗克粒子 m_p , 于是, $m = M_{bm} = m_p = 1.058 \times 10^{-5}$ g (5j). 正是“宇宙包”内每个粒子 m 的这 3 种状态的共同作用导致所有的 m 在封闭的“宇宙包”内停止收缩而爆炸解体, 并与整个前辈宇宙同步消失在普朗克领域, 从而共同阻止了前辈宇宙在普朗克领域继续塌缩成为“奇点”。同时, 无数最小黑洞 M_{bm} 的爆炸解体的结果又造成了宇宙包的少许膨胀和温度的少许下降.此后, 由于膨胀的宇宙包内的微小的温度和密度的差异会使稍高密度处的能量粒子吸收其周围的能量而生长为稍大一点点的新的最小黑洞 M_{bm} , 那时全宇宙中各处相邻的新最小的黑洞 M_{bm} 的合并和碰撞所同时产生的“小爆炸”合成了当时整个宇宙包的“大爆炸”和“原初暴涨”而导致新宇宙的诞生。由于新产生的最小黑洞质量的少许增加导致其寿命的相当大的增长, 从而使它们来不及爆炸就相互合并而变成稍大的黑洞。这个趋势如此继续下去, 就造成宇宙长大的黑洞不可逆转地继续与相邻的黑洞合并而继续长大膨胀下去, 直到使我们宇宙变成现今的巨无霸黑洞。宇宙最后的命运也会与所有黑洞的命运一样由于发射霍金辐射而收缩成为两个 $M_{bm} \approx 10^{-5}$ g 的最小黑洞而爆炸解体消失在普朗克领域。

本文的关键在于证实现宇宙是一个真实的宇宙大黑洞(UBH): 来源于最小黑洞, 按照黑洞的规律膨胀和消亡。^{<10>}这样, 宇宙诞生和演化中的各种难题就简化成为黑洞的问题。而黑洞是宇宙中最简单的物体(实体).因此, 最复杂难解的广义相对论方程和其解就可以置之高阁了。在结论中,本文还论述了从大塌缩到大膨胀发生的过程,并提出和论证了宇宙的“原初暴涨”来源于最小黑洞的碰撞和合并.宇宙现今的膨胀也是这类小黑洞碰撞后“暴涨”的持续效应,并以多种方法论证而得出了“现在的宇宙是一个真正的宇宙大黑洞”的确凿结论, 以及宇宙今后消亡的途径等等许多新观点。

本文中所有的结论都是根据现有的经典理论的基本公式和标准统一的数据计算而来。计算出的结果也完全而准确地符合现在所知的能量质量守恒和转换以及热力学等物理定律。唯一的最简单的假设就是按照时间反演和对称规律, 推断我们宇宙的诞生来源于前辈宇宙的最后大塌缩, 从这种大塌缩到新宇宙诞生的整个“相变”的转变过程完全符合因果律: 凡是有开端的事实都有原因。这种假设也是最简单而符合奥康姆剃刀(Ockham's razor)原则的。不像“奇点”那样不可理解,无法计算出与现今宇宙参数之间的任何有规律关系。

([<]参考文献编号)

关键词: 宇宙中没有奇点, 宇宙不是产生于“奇点”或者“奇点的大爆炸”。宇宙诞生于($M_{bm} \approx 10^{-5}$ g)史瓦西最小黑洞, 宇宙的“大爆炸”是大量最小黑洞合并产生的爆炸, 宇

宙的“原初暴涨”(Original Inflation)产生于大量最小黑洞的合并,宇宙与黑洞的同一性,我们宇宙本身就是宇宙大黑洞,哈勃定律就是宇宙黑洞的膨胀规律,

***本文分为上下两篇,上篇为《对“黑洞内没有奇点”的新观念全新完整论证》。这两篇是相互连接而不可分割的姊妹篇。为了更好地了解本文的论证,请最好先看或者同时看本文的上篇即参考文献<10>.

I.我们宇宙的演化规律与公式:(图一)

宇宙的演化规律可用两种不同的简单方式较精确地描述.这是根据广义相对论;粒子物理学和近代天文观测的成就而得出的结果.通称之为宇宙”大爆炸”标准模型。

首先,附录 A 图一详细地标列出了宇宙在各个不同时期的演化过程中时间 t 与温度 T 的相互对应的关系,其各种数据简明,但不精确,而是近似的.<3><4><2>

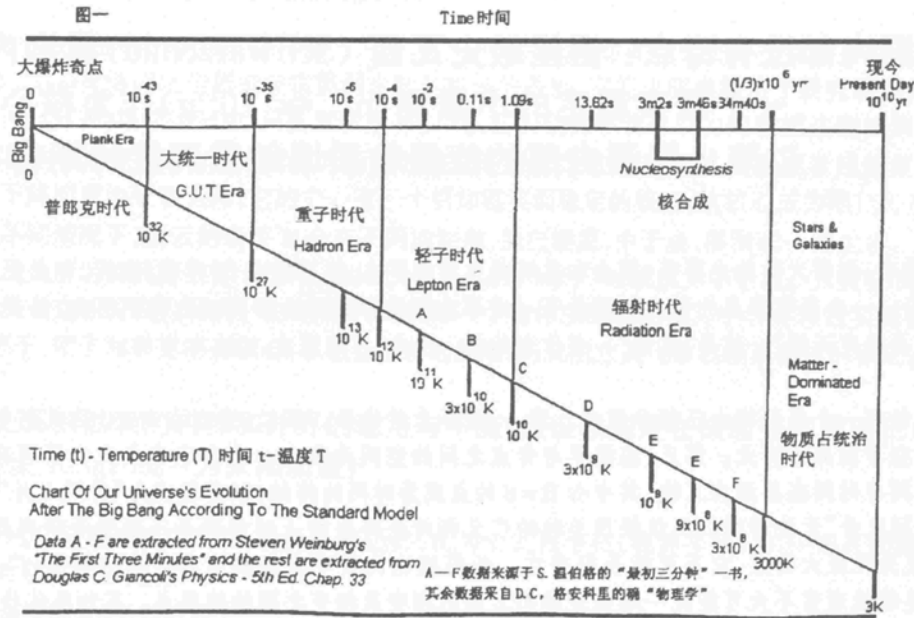
其次,下面的公式(1a)从量上定出了宇宙从辐射时代末期到大爆炸的过程中各个物理状态参数间的变化规律: (t=±10⁻⁴³ 秒到 t=1/3×10⁶ 年)

$$Tt^{1/2} = k_1, R = k_2t^{1/2}, RT = k_3, R = k_4\lambda, \quad (1a)$$

t—宇宙的特征膨胀时间, R—宇宙的特征尺度或大小, λ—辐射的波长,T—宇宙辐射温度, k₁,k₂,k₃,k₄—常数.

图一, 宇宙演变的标准模型中温度 T 与时间 t 的关系;<2>

9. 附录 A: 图一,宇宙演变的标准模型中温度 T 与时间 t 的关系;



附录 A 宇宙演变的标准模型中温度 T 与时间 t 的关系

下面的(1b) 式定出了宇宙在物质占统治地位时代各物理状态参数之间的变化规律和相互关系(t=1/3×10⁶ 年到现今)

$$Tt^{2/3} = k_6, R = k_7t^{2/3}, RT = k_8, R=k_9\lambda, \quad (1b)$$

T, t, R, λ—同上, k₆,k₇,k₈,k₉,—常数。(1a)和(1b)也很难十分准确地定出其各常数。

上式 Tt^{1/2}= k₁和 Tt^{2/3}= k₆.可参考 S. Weinberg 的“最初三分钟”之附录.如果将附录 A 图一中的数值与按照(1a)(1b)式中计算出来的数据相比较,其结果是相当一致的,图一中的数值不可能准确到小数点后 1 位数,所以是近似的。宇宙演化的这两组数据的一致性表明

用(1a)(1b)规律来表述宇宙的演化是正确的,与建立在广义相对论和近代粒子物理基础上的标准宇宙模型相符合.而且这些数据也与近代的天文观测数据 MBR (微波背景辐射)相吻合.我们如果给出一组宇宙演化的初始值或特定值,就可以取代(1a)(1b)中的各个常数 $k_1 \cdots k_9$,从而可以算出对应于宇宙演化各个时间 t 相对应的其它各参数如 T, R, \dots .作为例子,我们用(1b)计算宇宙在物质占统治时代的各个物理参数的变化,按照公式(1b),

$$R_1/R_2 = (t_1/t_2)^{2/3}, R_1 T_1 = R_2 T_2, R_1/R_2 = \lambda_1/\lambda_2, T_1/T_2 = (t_2/t_1)^{2/3},$$

如取 $t_1 = 13 \times 10^9$ yrs, $t_2 = 4 \times 10^5$ yrs, 则 $t_1/t_2 \approx 32,500$, $(t_1/t_2)^{2/3} \approx 1,000$.

取 $R_1 = 12 \times 10^{27}$ cm, 则 $R_2 = R_1/1,000 = 12 \times 10^{24}$ cm, 取 $T_1 = 3$ K, 则 $T_2 = 3,000$ K, 取 $\lambda_1 = 0.1$ cm, 则 $\lambda_2 = 10^{-4}$ cm.

以上各参数的初始值可见于附录 A 的图一,算出结果亦与图 1 中的数值近似地相吻合.以上数值表明宇宙从物质占统治时代的最初时刻膨胀至今,时间膨胀了约 32,500 倍,尺寸扩大了约 1,000 倍,温度则降低约 1,000 倍,辐射波长增长约 1,000 倍,符合 MBR(微波背景辐射)的观测数据.

由于我们宇宙在创生期的密度异常大,那时的宇宙好似“黄豆”般的大小.关键问题在于这颗“黄豆”从何而来?来源不外乎两个:(一),按照广义相对论,宇宙是从所谓的“奇点大爆炸”爆炸膨胀而来,从无到有,此路不通.因为它无法解释一个各种物理定律失效的“奇点”与一个如此有序的宇宙有任何物理量之间的联系.(二),是认为这颗“黄豆”由前辈宇宙收缩的大塌陷经过“相变”转变而来.本文的论证与计算就在于确证宇宙如何从前辈宇宙的“塌陷相”转变为现今宇宙“膨胀相”,这种相变发生的条件机理和途径.

II. 在宇宙诞生的早期,超高温和高能量密度状态下辐射和粒子的能量及其性质:

量子力学指出所有物质和辐射都具有粒子和波的二重性.在宇宙创生的早期,都在辐射为主的时期,超高温与高密度状态下的辐射与粒子在能量的表现形式上虽然不同,但是没有本质的差异而且有确定的质能相互对应和转变关系,以下的三种能量公式可看成单个粒子或辐射在同一瞬间的不同侧面像而同时存在并普遍适用,但在低能量与低温状态下,由于辐射和粒子的能量级别相差悬殊,而不能互相转换,二者之间才表现出明显的差异.在宇宙早期的超高温与高能量密度状态下,一个粒子可表现和转变的能量的三种形式如下:

$$E = mC^2, \quad E = \kappa T, \quad E = Ch/\lambda \quad (2a)$$

E —辐射粒子的能量, m —粒子的质量, C —光的速度, κ —波尔兹曼常数, h —普郎克常数, λ —辐射波长, T —辐射和粒子相互转变是温度(阈温),

从(2a), (1a)式得,

$$m = \kappa T/C^2, \quad R \propto \lambda, \quad R \propto 1/T \quad (2b)$$

在我们宇宙的早期,从“黄豆”宇宙膨胀到辐射时代结束,宇宙都由辐射与粒子二者组合而成的。(2a)(2b)在这种膨胀演化过程中,应该都是有效的,因为在宇宙早期当温度高于粒子的阈温值时,粒子与辐射的相互转化在任一瞬间都处于热动平衡状态,彼此能量相当而不停地互相转化.所以粒子与辐射之间并无差异.

从(2b)可见,当粒子的温度 T 增加时,其所转变成的粒子质量 m 也相应正比例地增加.但由于 κ/C^2 的值很小,所以巨大的温度差才能给质量 m 少许改变.温度 T 就是辐射和粒子相互转变的阈值温度.

III. 从前辈宇宙的“大塌陷”到现今宇宙的诞生的“大爆炸”的转变条件:

如果将前辈宇宙的最后“大塌缩”简单地假设成为我们宇宙诞生前的镜像反演，即假设将用于描述我们宇宙诞生后的演化公式(1a)也可以反向地用于描述前辈宇宙最后的塌缩演化规律，而塌缩后演化的结果根据计算如果符合现在宇宙各种规律和演变实况的数据的话，那么，这种假设就是合乎逻辑和规律的，就应当是合理可靠而予以承认的。从公式(1a) $R=k_2t^{1/2}$ 和(2a), (2b)可知，当前辈宇宙走向大塌缩收缩其尺寸 R 时，相应地其粒子温度 T 与质量 m 亦相应增加。在大塌缩收缩过程中(反向参看上面图一 A 中 Plank Era),当 t 缩小 1,000 倍时，R 只缩小 30 倍，所以 t 比 R 收缩得更快，这样收缩的结果，总会出现一种极限情况，当 t 收缩到某种极限时间时，两个相邻的粒子传递其引力所需的时间小于各个粒子湮灭解体时间，使它们中心间的真实距离 d_m 会变得等于当时两相邻粒子的史瓦西半径之和 $2r$ 。这时，连接两个相邻粒子所需的引力传递时间为 $2t$ ，而每个粒子解体的 Compton Time $t_c < t$ ，t 为各个粒子的半径 r 除以光速 C, $t = r/C$ 。当前辈宇宙收缩到此瞬间，每个单独的能量粒子与其相邻粒子间因无足够时间传递彼此的引力而造成其间引力的断链，于是变成在宇宙最高温度 $T \approx 10^{32}K$ 下爆炸成许多更碎小的高能微粒子并造成宇宙的少许膨胀，从而造成前辈宇宙的消亡，膨胀的结果，一方面使“宇宙包内的温度和密度随着少许的下降，另一方面造成宇宙包内的温度和密度产生少许差异。从而使得密度稍高处的能量粒子生长成为新的稍大一点黑洞，正是在宇宙包内各处的这些新产生的最小黑洞的合并和碰撞形成了新宇宙诞生的“大爆炸”和“原初暴胀”。这种在宇宙诞生前后由“塌缩相”向“膨胀相”的转变(相变)过程是不同于过去人们对“奇点大爆炸”所认同的概念的。自然，这种状态改变的过程是极其复杂而迅速的。现今尚无一种理论可以清晰的描述这个过程，也可能永远无法被观测到。本文后面作了较细致的想象性的描述。随着温度下降，时间的膨胀与引力的恢复，宇宙又开始了一个新的膨胀过程而延续到今天。

前辈宇宙从最后的“大塌缩”转变到现今宇宙最初的“大膨胀”发生的条件，按照相对论和上述的原理由以下公式(3)来表述，

d_m —两相邻粒子间的实际距离，m—前辈宇宙塌缩最后的粒子质量，r—粒子 m 的半径，t—宇宙粒子的光从中心传递到其视界半径的特征时间，C—光速， ρ —粒子 m 的能量-物质密度，H—哈勃常数，

$$d_m \geq C \times [2t], \text{ 即 } d_m/2C \geq t, -t \leq -d_m/2C, t = r/C \quad (3)$$

$$\text{由 } 4\pi\rho r^3/3 = m, \quad m = \kappa T/C^2, \quad (3a)$$

$$\therefore t^3 \leq 3\kappa T/4\pi\rho C^5 \quad (3a)$$

$$\text{由 } \rho = 3H^2/8\pi G = 3/(8\pi Gt^2), \quad (3b)$$

$$\therefore t \leq T(2G\kappa)/(C^5), \quad (3b)$$

$$\text{从(1a), } Tt^{1/2} = k_1 \quad (3ca)$$

$$\therefore t^{3/2} \leq k_1 (2G\kappa)/C^5 \text{ 或者 } t \leq [k_1 (2G\kappa)/C^5]^{2/3} \quad (3c)$$

公式(3a),(3b),(3c)都是从公式(3)推导出来的，所以三式中的 t 是等值的。

现求 t 值如下：先从上面的图一中选取一对 t, T 值代入(1a)求 k_1 。当取 $t = 10^{-43} s$ ，图中下面对应的温度 $T = 10^{32}K$ ，

$$k_1 = Tt^{1/2} = 10^{32} \times 10^{-43} s = 3^{1/2} \times 10^{10} \approx 1.732 \times 10^{10}, \text{ 从公式(3c),}$$

$$t^{3/2} \leq [(2G\kappa)/(C^5)] \times k_1 = 1.732 \times 10^{10} [(2G\kappa)/(C^5), \quad (3cb)$$

$$G = 6.67 \times 10^{-8} \text{ cm}^3/\text{g s}^2, C = 3 \times 10^{10} \text{ cm/s}, \kappa = 1.38 \times 10^{-16} \text{ g cm}^3/\text{s}^2 \text{ K},$$

$$t^{3/2} \leq [(2 \times 6.67 \times 10^{-8} \times 1.38 \times 10^{-16}) / (3 \times 10^{10})^5] \times 1.732 \times 10^{10} = 0.075758 \times 10^{-74} \times 1.732 \times 10^{10} \approx$$

$$0.1312 \times 10^{-64},$$

$$t^3 = 0.017217 \times 10^{-128} = 0.17217 \times 10^{-129}, t = 0.5563 \times 10^{-43} \text{s},$$

$$\therefore \underline{t \leq 0.5563 \times 10^{-43} \text{s}}, \text{ 与 } \underline{t \geq 0.5563 \times (-10^{-43}) \text{s}}, \quad (3d)$$

相对应地:

$$\underline{T = k_1/t^{1/2} = 1.732 \times 10^{10} / (0.5563 \times 10^{-43})^{1/2} = 1.732 \times 10^{32} \text{K} / 2.3586 = 0.734 \times 10^{32} \text{K}}, \quad (3e)$$

而对应于 $0.622 \times 10^{32} \text{K}$ 的粒子的质量 m :

$$m = \kappa T/C^2 = 1.38 \times 10^{-16} \times 0.734 \times 10^{32} / (9 \times 10^{20}) = 1.125 \times 10^{-5} \text{g}, \quad (3f)$$

$$\rho = 3/(8\pi G t^2) = 0.5786 \times 10^{93} \text{g/cm}^3, \quad (3g)$$

$$\text{由 (3aa) 式, 粒子 } m \text{ 的半径 } r = (3m/4\pi\rho)^{1/3} = 1.67 \times 10^{-33} \text{cm}, \quad (3h)$$

$$d_m = C \times [2t] = 3.34 \times 10^{-33} \text{cm}, \quad d_m \geq 2r (= 3.34 \times 10^{-33} \text{cm}) \quad (3i)$$

$$\therefore \underline{d_m \geq 2r} \text{ 表示粒子间的引力链在此时确实是断开了.} \quad (3j)$$

由无数粒子 m 所组成的宇宙包的密度 ρ_u ,

$$\rho_u = m/d_m^3 = 0.302 \times 10^{93} \text{g/cm}^3 \quad (3k)$$

$\rho_u < \rho$ 表明粒子之间空间的能量-物质被吸入粒子而密度大大地降低。

$$mC^2 = 1.125 \times 10^{-5} \times 9 \times 10^{20} = 1.013 \times 10^{16}$$

$$\kappa T = 1.38 \times 10^{-16} \times 0.734 \times 10^{32} = 1.013 \times 10^{16}$$

$$\text{而粒子数 } n_t = mC^2/\kappa T = 1 \quad (3kl)$$

(3kl)式表明, 整个宇宙都塌缩成为“宇宙包”内的一个个单独的的最高能量粒子, 而且每个粒子 m 因为与相邻粒子间的引力断链而在宇宙最高温度下爆炸解体变成了许多高热能的微粒子。

结论: 计算值 $t \leq 0.5563 \times 10^{-43} \text{s}$, $T = 0.734 \times 10^{32} \text{K}$ 几乎精确地符合附录 A 图一中 (Plank's Era) 普朗克时期末端值。对于时间反转的前辈宇宙来说, 就是塌缩到进入普朗克时期的开始端。上述计算值表示前辈宇宙一旦收缩到大塌陷的 $t = -0.5563 \times 10^{-43} \text{s}$, $T = 0.734 \times 10^{32} \text{K}$ 时, 整个宇宙包内的粒子都塌缩成为一个个单独的宇宙的最高能量粒子, 再由 (3d) 和 (3i) 式可见, 而两相邻的粒子间的引力将会无足够时间通过其距离而失去引力联系后爆炸, 因为两相邻粒子之间的引力联系需要 $2t = d_m/C = 2r/C$ 的时间, 而粒子解体和湮灭的时间为康普顿时间 t_c , $t_c < t (= 0.5563 \times 10^{-43} \text{s})$, 参见下面第 V 节。宇宙包内所有粒子在康普顿时间 t_c 内的解体和湮灭也就是前辈宇宙的消失。从而使宇宙变成为从“大塌陷”到“大膨胀”的反向转变(相变), 结果宇宙不会继续收缩并深入普朗克时代的终端而达到“奇点”。在这个设想中, 宇宙从前辈宇宙收缩塌陷到膨胀的转变过程中, 也会出现 $t = 0$ 的点, 但这并非人们所认知的“奇点”, 而只是宇宙从收缩塌陷点 $(-10^{-43} \text{s}, R)$ 到膨胀爆炸点 $(+10^{43} \text{s}, R)$ 之间的过渡桥梁, 因为, 在 $t = 0$ 点, 宇宙尺寸 $R \neq 0$, 温度 $T \approx 10^{32} \text{K}$, 而不是无限大, 宇宙密度 ρ_u 不是无限大而是 $= 3.02 \times 10^{92} \text{g/cm}^3$ 。这种观点使宇宙演化合乎能量守恒, 合乎因果律(热力学第二定律), 不违反现存的各种天体物理定律与经典理论而是它们之间的无缝结合。

由于无数粒子聚集所形成的宇宙包, 并非自由空间, 前辈宇宙无数粒子最小黑洞 m 的爆炸解体湮灭是在密闭的宇宙包内完成。因此, 爆炸一方面造成了闭合的宇宙包的少许膨胀(指其内部各处的膨胀速度小到任何时刻在各地都能保持热平衡状态)和温度密度的少许降低, 另一方面使爆炸解体后的微粒子在密闭的宇宙包内发生碰撞而有可能生成无数新的稍大的最小黑洞, 它们的合并和膨胀造成了新宇宙的诞生。

IV, 史瓦西最小黑洞 M_{bm} :

从第 3 节公式 (3) (3c) 可知, 一旦前辈宇宙塌陷到 $t = -0.5563 \times 10^{-43}$ 秒 $T = 0.734 \times 10^{32}k$ 的状态时, 两个相邻粒子间的引力失去联系而断开了, 此时任何一个粒子的质量 M_{bm} : 从公式 (2b),

$$M_{bm} \approx m = 1.125 \times 10^{-5}g \quad (4a)$$

$$m \text{ 的半径 } r, \text{ 如上述, } 4\pi\rho r^3/3 = m, \quad r = 1.67 \times 10^{-33}cm, \quad (4b)$$

如果每个粒子 $1.125 \times 10^{-5}g$ 是一个最小黑洞, 按照上篇^{<10>}中黑洞的严格的论证, 可取 $M_{bm} = 1.125 \times 10^{-5}g$, 则它的史瓦西半径 r_b 为:

$$r_b = 2GM_{bm}/C^2 \text{ ⁶ ³} = 2 \times 6.67 \times 10^{-8} \times 1.125 \times 10^{-5} / (3 \times 10^{10})^2 = 1.667 \times 10^{-33}cm, \quad (4c)$$

由于 (4b) = (4c) 可见, $r = r_b$, 证明 $m = M_{bm} = 1.125 \times 10^{-5}$ 克的确是一个真实的宇宙最小的史瓦西黑洞。其密度 ρ_b , 温度 T_b , 史瓦西 (Schwarzschild) 时间 t_b ,

$$\rho_b = 3M_{bm}/(4\pi r_b^3) = 5.8 \times 10^{92}g/cm^3, \quad (4d)$$

$$T_b = M_{bm}C^2/k = 1.125 \times 10^{-5} \times 9 \times 10^{20} / 1.38 \times 10^{-16} = 0.734 \times 10^{32}k, \quad (4e)$$

$$t_b = r_b/C = 1.667 \times 10^{-33} / 3 \times 10^{10} = 0.5557 \times 10^{-43}s, \quad (4f)$$

由于黑洞粒子有极其强大的引力, 因此在黑洞粒子之间的空间不太可能存在能量-物质, 可以看成为真空, 所有整个宇宙包空间的平均密度为 ρ_u 如上所述,

$$\rho_u = m/d_m^3 = 3.02 \times 10^{92}g/cm^3 \quad (3k)$$

最小史瓦西黑洞内的粒子数,

$$n_m = M_{bm}C^2/kT = 1.125 \times 10^{-5} \times 9 \times 10^{20} / (1.38 \times 10^{-16} \times 0.734 \times 10^{32}) = 0.9996 = 1 \quad (4g)$$

结论: (4g) 表明, 当前辈宇宙塌缩到形成无数的 $M_{bm} = m = 1.125 \times 10^{-5}$ 克最小黑洞时, 每个 M_{bm} 就是一个宇宙最高温的最小黑洞, 内部的引力因不可能再发出霍金辐射而收缩, ^{<10>} 只能在外引力断链的宇宙最高温状态下爆炸消亡。因此, 所有最小黑洞 m 从 $t = -0.5563 \times 10^{43}$ 秒到 $t = 0$ 在普朗克量子领域中的消失就等同于前辈宇宙到达 $t = 0$ 时的消失, 而后, 才形成了全宇宙内从 $t = 0$ 到 $t = +0.5563 \times 10^{43}$ 秒后产生较大的新的最小黑洞, 它们的出现合并造成了我们现在新宇宙的诞生和宇宙的“原初暴胀”。

V. 量子力学中测不准原理应用于引力量子论: 普朗克量子领域。 ⁶

$$\Delta E \times \Delta t \geq h / 2\pi, \quad (5a)$$

h --普朗克常数 = $6.63 \times 10^{-27}gcm^2/s$, C --光速 = $3 \times 10^{10}cm$, 产生或湮灭两个基本粒子所需的能量 ΔE 为:

$$\Delta E = 2mC^2, \quad (5b)$$

所以具有能量 ΔE 的两个基本粒子 m 的产生或湮灭时间 Δt 为: 由 (5a)(5b) 式:

$$\Delta t = t_c = h/4\pi m C^2 \quad (5c)$$

t_c ---康普顿 (Compton) 时间, 令 t_s ---史瓦西 (Schwarzschild) 时间, 即光通粒子 m 的史瓦西半径 r_b 所需的时间:

$$t_s = 2Gm / C^3 = 0.5 \times 10^{-43} \text{ 秒} \quad (5d)$$

在一般情况下, $t_c < t_s$ 而在 $t_c = t_s$ 时, $m = m_p$, m_p ---普朗克 (Plank) 质量,

$$m_p = m = (hC / 8\pi G)^{1/2} = 10^{-5} \text{ 克} \quad (5e)$$

对应于普朗克质量 m_p 的普朗克 (Plank) 时间 t_p 为:

$$t_p = (Gh / 2\pi C^5)^{1/2} = 0.539 \times 10^{-43} \text{ 秒} \quad (5f)$$

而相应的普朗克长度 (Plank's length) l_p 为:

$$l_p = t_p \times C = (Gh / 2\pi C^3)^{1/2} = 1.61 \times 10^{-33} \text{cm} \quad (5g)$$

普朗克温度 T:

$$T = mC^2/k = 0.65 \times 10^{32} \text{K} = 10^{19} \text{GeV} \quad (5h)$$

$$m_p / l_p = [(hc / 8\pi G)^{1/2}] / [C (Gh / 2\pi C^5)^{1/2}] = C^2 / 2G \quad (5i)$$

表一：以上三种状态的计算比较结果:完全一致如下表.

引力断链时的状态	最小黑洞状态	Plank 量子状态
$m=1.125 \times 10^{-5} \text{g}$	$M_{bm} = 1.125 \times 10^{-5} \text{g}$	$m_p = 1.058 \times 10^{-5} \text{g}$,
$t = \pm 0.5563 \times 10^{-43} \text{s}$	$t_b = 0.5557 \times 10^{-43} \text{s}$	$t_p = 0.539 \times 10^{-43} \text{s}$,
$T = 0.734 \times 10^{32} \text{k}$	$T_b = 0.734 \times 10^{32} \text{k}$	$T = 0.65 \times 10^{32} \text{k}$,
$d_m / 2 = 1.67 \times 10^{-33} \text{cm}$	$r_b = 1.667 \times 10^{-33} \text{cm}$	$l_p = 1.61 \times 10^{-33} \text{cm}$,

VI. 从前面的论证和表一的各种数值的比较分析可以得出一个令人信服的结论：前辈宇宙最后大塌缩的结果是成为 M_{bm} 最小黑洞在普朗克量子领域消亡，继而转变为膨胀造成新宇宙的诞生，而不是塌缩成为“奇点”。

1. 以上表一列明了前辈宇宙最后大塌缩所形成的 3 种状态的各个参数值，各种物理量计算所得出的数值几乎是完全一致的，这 3 种状态（引力断链，形成最小黑洞和进入普朗克量子领域）是在前辈宇宙大塌缩到 $t = -0.5563 \times 10^{-43} \text{s}$ 时几乎是连续而同时发生的，从而阻止了前辈宇宙继续向普朗克领域一直深入下去塌缩成为“奇点”。如果 2 种状态的各种参数数值的一致性可以看成为巧合的话，那么，这 3 种状态的各种参数数值的一致性就绝对不可能成为巧合了，而是反映出了前辈宇宙塌缩时不可能出现“奇点”的真实状态，从而发生了前辈宇宙从“塌缩相”在普朗克量子领域转向“膨胀相”的“相变”。这也证明作者的前面的假设不是一种毫无根据的猜想，而可以按照多种可靠的理论公式计算出来的准确的数据所得出的正确的推断和结论。

$$= 1.058 \times 10^{-5} \text{g} \quad \text{Plank 量子状态的} \quad M_{bm}$$

$$\underline{1.058 \times 10^{-5} \text{g}}$$

上面
 \gg^{10} 的

= $m_p = 1.058 \times 10^{-5}$ 克的两个最小黑洞爆炸解体在普朗克量子领域
 最小黑洞状态和 Plank 量子状态

引力断链时的状态

$m = 1.125 \times 10^{-5} \text{g}$ 与 1.058×10^{-5} 克稍有误差，误差来源于宇宙演变公式(1a) 和图一中 $Tt^{1/2} = k_1$ 的 3 个参数 T, t, 和 k_1 都是大约的数值，这就造成了 m 的误差。比如，如果取图一中的 t T $m = 0.954 \times 10^{-5} \text{g}$ 。如果用图一中的 t T $m = 0.8 \times 10^{-5} \text{g}$ ，这个误差则更大一些。

因此，准确严格的数值应该是： $m = M_{bm} = m_p = \underline{1.058 \times 10^{-5} \text{g}}$ (5j)

t_p , $t_p \approx -0.539 \times 10^{-43}$ s 时, 3 种状态 (引力断链状态, 最小黑洞状态, Plank 量子状态) 是完全等同而同时出现的。因此, $t = \pm 0.5563 \times 10^{-43}$ s 是由图一中原始数据误差计算误差所产生的近似值。

时间的误差 $\Delta t = (0.5563 - 0.539) / 0.539 = 0.032 = 3.2\%$

质量的误差 $\Delta m = (1.125 - 1.058) / 1.058 = 0.063 = 6.3\%$

3. 按照本文上篇^{<10>}中的论证和计算, 所有的黑洞的最后命运都是塌缩成为 $M_{bm} = 1.058 \times 10^{-5}$ g 的最小黑洞而达到与普朗克量子质量 m_p 相等, 即 $M_{bm} = m_p$, 而随着在宇宙最高温度 $T = 10^{32}$ k 的量子领域爆炸解体消亡。可见, 上述前辈宇宙大塌缩的最后命运与所有黑洞的最后命运是完全一样的。^{<10>} $M_{bm} \approx 10^{-5}$ g 的最小

至于造成前辈宇宙塌缩的原因和机理也许将永远无法知道, 但其最终塌缩成为 $M_{bm} \approx 10^{-5}$ g 的最小黑洞后的演变却可以证实宇宙诞生前的时间反转。

4. 这就是说, 如果消除了宇宙演变公式 (3ca) $Tt^{1/2} = k_1$ 中的误差, 上面表一中三组相对应的数值应该是完全相等的, 这就证明了前辈宇宙的最后大塌缩完全遵循黑洞的一般规律, 也说明我们宇宙的来源是有根据的, 是符合因果律的, 不是“无中生有”, 不是产生于无法计量又无法理解的“奇点”或者“奇点的大爆炸”, 不是上帝派发的“免费午餐”。

5. 普朗克时间 (Plank Time) t_p , 原来只有正值才有意义, 但在上面本文关于宇宙演化的新概念中, $-t_p$ 也有物理意义, $-t_p$ 表示前辈宇宙塌陷到 -0.539×10^{-43} 秒时, 粒子开始失去引力而爆炸解体进入普朗克时代的时间, 而 $+0.539 \times 10^{-43}$ 秒则表示现今宇宙在诞生时重新恢复粒子间引力的时间。

6. 在“宇宙包”内无数最小黑洞 $M_{bm} \approx 10^{-5}$ g 的爆炸解体消亡后, 因为爆炸后所有的各种高能粒子(粉尘)是逃不出“宇宙包”的, 因此, 在相互混合与碰撞后在宇宙密度稍微降低的环境下可以重新集结长大成新的稍大的最小黑洞。而单个在自由空间的黑洞收缩到最小黑洞 $M_{bm} \approx 10^{-5}$ g 爆炸后就分解成为大量的高能量和高速度的粒子(γ 射线), 分散在自由空间的各个方向, 再也不可能重新集结。

VII. 前辈宇宙从 Plank 时代 ($t < -0.556 \times 10^{-43}$ 秒) 的大塌缩到现今宇宙的大膨胀 ($t > +0.556 \times 10^{-43}$ 秒) 的“相变”转变过程, 即从旧宇宙的消亡到新宇宙的诞生的大致过程,

1. 从前辈宇宙的大塌缩转变到现今宇宙的大膨胀产生的机理和原因; 前面所有计算表明一旦前辈宇宙塌陷到 $t = -0.556 \times 10^{-43}$ 秒, 公式 $t \leq -[k_1 (2G\kappa) / (C^5)]^{2/3} \approx -0.556 \times 10^{-43}$ s, 当时前辈宇宙中每个粒子 ($m = M_{bm} \approx 10^{-5}$ 克) 都与其相邻的粒子变失去了无引力联系, 因为两个临近粒子之间的距离 $d_m = 2r$, 而各个粒子的康普顿时间 $t_c =$ 史瓦西时间 t_s , 即 $t_c = t_s = r/C = 0.539 \times 10^{-43}$ 秒, 因此, 两个临近粒子连在一起最少需要大于 $2t_s$ 的时间传递引力, 这是两个临近粒子黑洞没有足够时间传递引力而造成引力的断链的原因。断链后的所有粒子又同时进入普朗克量子领域的和最小黑洞的状态, 正是所有粒子几乎同时发生的这三种状态共同刹住了前辈宇宙向奇点的塌缩, 使前辈宇宙从最小黑洞的爆炸消亡一起同时消亡在普朗克量子领域 (Planck Era)。爆炸后的微粒子又会从极高温而又极不稳定的普朗克量子状态重新聚集收缩成新的较大的最小黑洞而脱离普朗克领域。新宇宙就是从这无数新的较大的最小黑洞的碰撞和合并所产生的“大爆炸”中诞生。这个转变过程完全是通过进出普朗克量子领域的“相变”来完成的。而不是通过现有的物理规律所无法了解的“奇点”或“奇点的大爆炸”来完成的。这就是本文中对宇宙诞生的新观念。这三种状态的数值在同一时间是完全相等的, 是从完全不同的理论 (牛顿力学与相对论, 量子力学, 量

子引力论, 黑洞理论和宇宙的演变规律等) 分别计算出来的, 殊途同归的 3 组数值验证了本文中新观念的正确性和论证的可靠性。从而证实本文开始时的猜想或推断是完全符合现今宇宙的真实状态的。

2. 前辈宇宙的消亡: 即前辈宇宙在Plank时代 (-0.556×10^{-43} 秒) \Rightarrow ($t \approx 0$) 区间内的变化; 由于前辈宇宙塌缩到 $t \approx -0.556 \times 10^{-43}$ 秒时, 粒子 $m \approx 10^{-5}$ 克均成为量子最小黑洞. 传递相邻粒子间的引力需时 $\geq 2(0.556 \times 10^{-43})$ 秒, 而无外部引力联系的每个粒子黑洞都成为单个的基本粒子。因而只能在高温的 $T_b \approx 10^{32} \text{K}$ 所产生高辐射热压力下在小于康普顿时间 $t_c = 0.539 \times 10^{-43}$ 内爆炸解体消亡于Plank时代的量子场中. 当时前辈宇宙中每个最小黑洞 ($M_{bm} \approx 10^{-5}$ 克) 的“小爆炸”而形成整个前辈宇宙的“大爆炸”的消亡过程就是整个前辈宇宙的彻底消失过程。也正是这种“爆炸”和“膨胀”阻止了前辈宇宙向“奇点”的塌缩, 但这并不是新宇宙诞生的“大爆炸”。这类最小黑洞爆炸后的碎粒 (高能粒子) 一方面使宇宙空间充满较均匀的能量-物质粒子的混合, 另一方面也使宇宙包内稍微降低了温度和密度, 使这些碎粒在其爆炸的高速碰撞下再重新结合成新粒子, 并进而长大成新的较大的最小黑洞。从而能由“塌缩相”转变为“膨胀相”。这给新宇宙的诞生提供了物质基础和创造了必要而充分的条件, 使前辈宇宙的消亡在“宇宙包”内转变为新宇宙的诞生。由于膨胀相所造成的温度和密度的少许降低, 由粒子黑洞爆炸出来的微量子在混合碰撞后没有更高的能量温度以结合成远小于 10^{-5} 克的新的微小量子黑洞。更没有时间塌缩成远大于 10^{-5} 克的新的量子黑洞, 因为塌缩成稍大的黑洞需要稍长的时间。因而只能通过普郎克领域结合成稍为大于 10^{-5} 克的新最小量子黑洞。

3. 新宇宙的诞生: 即现今宇宙在 Plank 时代从 ($t \approx 0$ 秒) \Rightarrow ($t \geq +0.556 \times 10^{-43}$ 秒) 区间内的变化; 在这阶段内重新聚集和长大的粒子可能有较多时间成长为比 $M_{bm} \approx 10^{-5}$ 克的稍大的新粒子最小黑洞。虽然新生宇宙在此阶段是开始处于膨胀阶段, 单个新生的最小黑洞视界的膨胀速度的极限 = C(光速). 因此在单个最小黑洞的视界内, 在如此高密度下, 宇宙包内各处相邻粒子之间的相对膨胀速度不会很大, 不会打破瞬时的热平衡状态。因而是难以阻止相邻粒子的重新聚集和结合的。何况, 更由于上阶段前辈宇宙最小黑洞的爆炸和膨胀使得宇宙温度和密度的少许降低, 也由于爆炸后碎粒子之间的高速碰撞, 从而在 Plank 时代中的较小的粒子比较易于聚集在较大的粒子周围形成新的较大的新宇宙的粒子最小黑洞。现粗略地估算如下: 由于前辈宇宙最小黑洞爆炸所造成的膨胀, 此时宇宙包内的能量-物质密度 $\rho_x < \rho_u$,

$$\rho_x < \rho_u (< \rho_b) = m / d_m^3 = 0.302 \times 10^{93} \text{g/cm}^3 \quad (3k)$$

对应于 ρ_x 形成的新微小黑洞所需时间,

$$t_x^2 > 3 / (8\pi G\rho) = 0.592 \times 10^{-86}, t_x > 0.77 \times 10^{-43} \text{秒} \quad (7c)$$

对应于 t_x 所形成的新黑洞质量 m_x ,

$$m_x > C^2 r_x / 2G = C^3 t_x / 2G = 1.56 \times 10^{-5} \text{g} > (M_{bm} = 1.058 \times 10^{-5} \text{g}) \quad (7ca)$$

对应于黑洞 m_x 的寿命可用霍金公式计算,

$$\tau_x > 10^{-27} m_x^{-3} = 38 \times 10^{-43} \text{秒}^{<5>} \quad (7cb)$$

(7ca)式表明所新形成的最小黑洞 m_x 已经脱离普郎克领域而进入到大统一时代(图一)。

$t_x > 0.77 \times 10^{-43}$ 秒表示形成一个 $m_x > 1.56 \times 10^{-5} \text{g}$ 的新的稍大的黑洞至少需要大于 0.77×10^{-43} 秒的时间。由于 $\tau_x \approx 50 t_x \gg 2 t_x$, 因此, 所新形成的许多相邻的较大的 m_x 最小黑洞有足够的时间恢复彼此之间的引力链, 紧接着就发生相互的合并和碰撞, 这种当时所有新的较大的最小黑洞都参与的合并和碰撞形成了强烈的爆炸, 并且在宇宙的各处遍地开花

而组成宇宙的“大爆炸”。这就是诞生新宇宙的“大爆炸”。因此，宇宙是诞生于无数新最小黑洞 m_x 和它们相邻的黑洞所产生的合并和碰撞形成的“大爆炸”，而绝不是诞生于“奇点”或者“奇点的大爆炸”。同时，这无数新最小黑洞 m_x 和它们相邻的黑洞所产生的合并和碰撞又造成了初生宇宙的急速大膨胀。于是宇宙的“原初暴胀”(Original Inflation) 应运而生。

结论：我们宇宙诞生于大量新生成的 $M_{bm} \approx m_x \approx 10^{-5}$ 克的最小黑洞，而不是“奇点”。所以 $m_x = M_{bm} \approx 10^{-5}$ 克的新生最小黑洞就是诞生宇宙的“原生黑洞”，或者称为“原生史瓦西最小黑洞”。

VIII. 黑洞的膨胀本性：^{<10>}

按照黑洞的史瓦西公式，一个黑洞质量 $M_b = R_b C^2/2G$ (8a)

则 $dM_b = dR_b C^2/2G$ (8aa)

设有另外一个黑洞 M_{b1} 与 M_b 碰撞与合并，

$M_{b1} = R_{b1} C^2/2G$, (8ab)

(8a) + (8aa) + (8ab) 之后，得

$M_b + M_{b1} + dM_b = (R_b + R_{b1} + dR_b) C^2/2G$ (8ac)

由(8ac)式可见，当一个黑洞形成之后，无论它是吞噬外界能量-物质，或者是与其它的黑洞碰撞与合并，或者是向外发射能量-物质，即发射霍金辐射，直到它最后塌缩成为 $M_{bm} = 10^{-5}$ 克的微小黑洞而爆炸消失之前，它将永远是一个黑洞，而且按照黑洞的规律和在其视界半径 R_b 上的守恒公式运动和变化。^{<10>}只不过黑洞质量 M_b 有所增加或者减少而已。随着黑洞质量 M_b 的改变，黑洞的其它参数， R_b ， T_b ， ρ_b 等也随着黑洞质量 M_b 的改变而单值唯一地改变。^{<10>}

IX. 完全证明：我们现在的宇宙就是一个真正的宇宙大黑洞 (UBH)，^{<11>}宇宙的膨胀就是宇宙诞生时的大量 $m_x = M_{bm} \approx 10^{-5}$ 克的新原生最小黑洞合并所造成的膨胀，哈勃定律就是宇宙黑洞在吞噬外界能量-物质时黑洞内部的膨胀规律。

第一：宇宙现今的较准确的观测数据证实我们现今宇宙 M_{ub} 就是一个真实的宇宙大黑洞(UBH)

为了解释我们宇宙作为一个真实的宇宙黑洞(UBH)的特性，两个较精确地有关我们宇宙的最近的观测数据将采用如下：如果下述两个数据较可靠的话，可得出如下结果。(a). 最近观测的我们宇宙从大爆炸到现在的较准确年龄 A_u 是： $A_u = 13.7 \times 10^9 \text{ yrs.}$ ^[9] 则我们宇宙现今的可视半径为 R_u ： $R_u = C \times A_u = 1.3 \times 10^{28} \text{ cm}$ ，密度 $\rho_u = 3/(8\pi G A_u^2) = 0.958 \times 10^{-29} \text{ g/cm}^3$ 。则可得宇宙的总质量 $M_u = 8.8 \times 10^{55} \text{ g}$ 。就是说，可观测的最远的星云离我们大约 $1.3 \times 10^{28} \text{ cm}$ ，这就是光在我们宇宙年龄 A_u 内的行程，我们宇宙的可视视界为 $2R_{uv}$ 。(b). 哈伯常数的新的较准确的观测数值， $H_0 = (0.73 \pm 0.05) \times 100 \text{ kms}^{-1} \text{ Mpc}^{-1}$ ^[12]。从而可得出我们宇宙的实测密度 ρ_r 为： $\rho_r = 3H_0^2/(8\pi G) \approx 10^{-29} \text{ g/cm}^3$ 。由此得出宇宙的年龄 $A_r = 3/(8\pi G \rho_r)$ ， $A_r = 0.423 \times 10^{18} \text{ s} = 134 \pm 6.7$ 亿年。相应地宇宙质量， $M_r = 8.6 \times 10^{55} \text{ g}$ 。由此可见，这两组用不同的观测方法所得出数值是极其接近的，说明我们宇宙现在的总质量 M_u 有一个确定的数值，即 $M_u = (8.8 \sim 8.6) \times 10^{55} \text{ g}$ 。

现取宇宙的总质量 $M_{ub} = 8.8 \times 10^{55} \text{ g}$ ，按照史瓦西黑洞公式 $R = 2GM/C^2$ ，如果这 M_{ub} 是一个宇宙大黑洞(UBH)，其视界半径 $R_{ub} = 2 \times 6.67 \times 10^{-8} \times 8.8 \times 10^{55} / 9 \times 10^{20} = 1.304 \times 10^{28} \text{ cm}$ 。结果如下，

$$R_{ub} (1.304 \times 10^{28}) = R_u (1.3 \times 10^{28} \text{ cm}) \quad (9a)$$

可见, 从现今对宇宙的较准确的观测数据来计算, 我们现今宇宙 M_{ub} 是一个真实的宇宙大黑洞(UBH)。

第二: 如果我们宇宙 $M_{ub} = 8.8 \times 10^{55} \text{ g}$ 是一个真实的宇宙大黑洞 (UBH), 它就必定来源于无数的宇宙诞生时的 $M_{bm} \approx 10^{-5}$ 克的原生最小黑洞的合并。^{<10>}现在按照公式(8ac)的原理证实如下:

设 M_{ub} 来源于 n_b 个原生史瓦西黑洞 $M_{bm} \approx 10^{-5}$ 克的合并, 则

$$n_b = M_{ub} / M_{bm} = 8.8 \times 10^{55} / 10^{-5} = 8.8 \times 10^{60} \quad (9b)$$

按照史瓦西公式(8a), M_{bm} 的史瓦西半径 r_b ,

$$r_b = 2Gm_b / C^2 = 1.48 \times 10^{-33} \text{ cm}, \quad (9c)$$

而 M_{ub} 的史瓦西半径 $R_{ub} = 1.304 \times 10^{28} \text{ cm}$.

$$\text{所以, } n_b = R_{ub} / r_b = 1.304 \times 10^{28} / 1.48 \times 10^{-33} = 8.8 \times 10^{60} \quad (9d)$$

由于(9b) = (9d), 可以证实宇宙大黑洞 M_{ub} 来源于 $n_b = 8.8 \times 10^{60}$ 个原生史瓦西黑洞 $M_{bm} \approx 10^{-5}$ 克的碰撞和合并后膨胀的结果。这也证明现在宇宙的膨胀完全符合一般黑洞的膨胀规律。

第三: 宇宙的平直性和 ($\Omega = \rho_r / \rho_0 \approx 1$) 是宇宙黑洞(UBH) M_{ub} 的本性, 哈勃定律所定义的我们宇宙的膨胀规律与宇宙黑洞内的膨胀规律完全一致, 就是说二者是一回事:^{<11>}

按照哈勃定律, 在我们宇宙内距离任何一点 P 为 R_p 的相对膨胀速度 V_p 为, H_0 --哈勃常数,
 $V_p = H_0 R_p \quad (9e)$

从公式(8a)和球体公式, 在黑洞视界上, 当 R_p 延伸到 R_{ub} 时, $V_p = C$, 于是,

$$H_0^2 = 8\pi G \rho_0 / 3 \quad (9f)$$

如果我们宇宙是一个真正的宇宙黑洞, 它就必然是一个封闭的球体; 因此, ρ_0 就是我们宇宙黑洞的密度, 从公式(8a)和球体公式可知, 它是单值且仅由 M_{ub} 或 R_{ub} 所决定。^[10] 然而, 宇宙的实际密度 ρ_r 也是来自同一个观测的 H_0 , i.e. $H_0^2 = 8\pi G \rho_r / 3$. 其必然结果是: ρ_r 应完全等于公式 (9f) 中的 ρ_0 , 所以, ($\Omega = \rho_r / \rho_0 = 1$) 是宇宙黑洞的本性. 反过来, $\Omega = \rho_r / \rho_0 = 1$ 也可证明我们宇宙是一个真正的宇宙黑洞. 也就是说, 对于宇宙黑洞来说, 宇宙只有一个密度, 根本没有临界密度这个回事, 而将 ρ_r 与 ρ_0 分开是广义相对论将理论与宇宙实际观测错误分离的结果。用这种理论与实际观测值分离后, 又要求实际去符合理论以判别宇宙未来的开放还是闭合, 这种思唯方法本身就是错误的, 根本就不可能得出正确的结论。

第四: 为什么我们宇宙的膨胀规律即哈勃定律与黑洞的膨胀规律完全一致?

将哈勃定律用于现在膨胀的宇宙球体 M_u , t_u 为宇宙年龄, R_u 为宇宙现在的视界半径

$$M_u = 4\pi \rho_0 R_u^3 / 3 = 4\pi (3H_0^2 / 8\pi G) C^3 t_u^3 / 3 = 4\pi (3H_0^2 / 8\pi G) C^3 t_u^3 / 3H_0^2 = C^3 t_u / 2 G \\ = C^2 R_u / 2 G \quad (9g)$$

再从史瓦西对广义相对论 (GTR) 的球对称黑洞的解可得, $C^2 / 2 = GM_b / R_b$, 这是黑洞存在的必要条件。因为 $R_b = C t_u = R_u$ 于是,

$$M_b = R_b C^2 / 2 G = C^3 t_u / 2 G = R_u C^2 / 2 G \quad (9h)$$

由黑洞推导出的 (9h) 式与由哈勃定律推导出的 (9g) 式是完全相等的。因为宇宙的年龄与黑洞宇宙的年龄是一样的。第一。这第 3 次 (前 2 次见上面的 2 段) 证明我们现在的宇宙就是一个宇宙大黑洞(UBH), 也清楚地证明由哈勃定律所定义的宇宙的膨胀规律就是宇宙黑洞 (UBH) 的膨胀规律. 第二。哈勃定律所反映的宇宙膨胀规律就是由于宇宙黑洞吞噬外界能量-物质增加质量而膨胀的规律, 即其视界的膨胀速度为 C, 而内部的相对膨胀速

率为 H_0 。因为从(9g)和(9h)式可见，宇宙质量 M_u 在随 t_u 的增加而增加。当黑洞宇宙外无能量物质可吞噬时，黑洞宇宙就不会膨胀，而哈勃定律就会失效。第三。不管一个黑洞是多么大还是多么小，是在膨胀还是在收缩，它始终是一个封闭的球体黑洞，不存在是开放还是封闭的问题，它只存在是在膨胀还是在收缩的问题。因此对任何一个黑洞来说，对应于某时一个黑洞确定的质量 M_u ，就只能有一个确定的(平均)密度 ρ_0 。广义相对论没有认识到宇宙为一个真实的黑洞，所以采用 $\Omega = \rho_r/\rho_0$ 以判别宇宙是开放还是封闭。可见由广义相对论所定义的 $\Omega = \rho_r/\rho_0$ 只是一种理论上的误导， Ω 是无法用于判断宇宙是“开放”还是“封闭”，所以几十年来对 $\Omega = \rho_r/\rho_0$ 的测定是毫无意义的。而宇宙黑洞就只能有一个(平均)密度，永远是 $\rho_r = \rho_0$ 和 $\Omega = 1$ 。而且宇宙黑洞的收缩或者膨胀的命运不是取决于其密度，而是取决于其是否吞噬外界的能量-物质而所增加的总质量。^{<10>}第四。正是由于上述广义相对论理论上的误导，导致科学家们数十年来在宇宙中寻找“丢失的能量-物质”，并提出了无法观测和确证的许多新概念，如“真空能量”，“暗能量”等，从(9d)式可知，既然我们现在的宇宙黑洞 $M_{ub}=8.8\times 10^{55}g$ 来源于宇宙诞生时的大量 $M_{bm} \approx 10^{-5}$ 克的原生最小黑洞的合并，而 M_{ub} 完全等于 $n_b = 8.8\times 10^{60}$ 个 M_{bm} 。这就是说，宇宙中现有 M_{ub} 全部都来源于宇宙诞生时原生最小黑洞 M_{bm} ，没有丢失什么能量-物质，也没有新添加什么能量-物质，而有可能发生的状况是：在宇宙这 137 亿年的演变过程中，原有的 M_{bm} 的某些能量-物质形式我们尚不知道，或者某些能量-物质在演变过程中改变了形式我们尚不认识，因此，现在的任务是找到它们和认识它们。

既然我们宇宙的膨胀就是宇宙黑洞的膨胀，那么，当我们宇宙包所有的 $M_{bm} \approx 10^{-5}$ 克的原生最小黑洞合并完成后，即完全膨胀后，如果宇宙的外界再无能量-物质可供吞噬时，宇宙就不再膨胀，而是开始发射极其微量的霍金量子辐射而极其缓慢的收缩。此时宇宙黑洞 $M_{ub} = M_b \approx$ 常数， $R_b \approx$ 常数，而只有宇宙年龄 t_u 却在增长。由于 $M_{ub} = M_b$ 非常巨大，它发射霍金量子辐射就极其微小，因损失能量使 R 的收缩就非常缓慢。因此，如果用哈勃定律来规范宇宙因发射霍金量子辐射的收缩量，会因为 H_0 的极其微小而无法测量出来。

X. 宇宙演变膨胀中的一些问题

1. 原始宇宙的尺寸大小：如上所述，假设宇宙黑洞(UBH)外面现在已经没有能量-物质可被吞噬，则宇宙总质量即是现在的 $M_{ub} = 8.8\times 10^{55}g$ 。而宇宙黑洞既然诞生于大量的 n_b 个 $M_{bm} \approx 10^{-5}$ 克的最小黑洞的合并，按照(9b)式， $n_b = M_{ub}/M_{bm} = 8.8\times 10^{60}$ 。如原始宇宙的尺寸的球半径为 R_0 ， M_{bm} 的史瓦西半径 $r_b = 1.67\times 10^{-33}cm$ ，则

$$R_0^3 = n_b r_b^3, \text{ 于是 } R_0 = 3.45\times 10^{-13}cm \quad (10a)$$

这就是说，原始宇宙包的球半径 R_0 的尺寸等于现在一个原子核的大小，即如果现在将整个宇宙 $M_{ub} = 8.8\times 10^{55}g$ 压缩成为宇宙诞生时的球粒子，该粒子的尺寸大约等于现在的一个原子核。

2. 宇宙膨胀的根源：如前(8ac)式所述，宇宙的膨胀根源是宇宙诞生时大量的 $M_{bm} \approx 10^{-5}$ 克的最小黑洞的合并。试想如果 2 个等质量的微小黑洞合并而完全膨胀后，其视界半径就会变成原来的 2 倍，体积就会变成原来的 8 倍。因此，宇宙的年龄 A_u 又可以表述如下：

$$A_u = n_b r_b / C = 8.8\times 10^{60} \times 1.48\times 10^{-33} / 3\times 10^{10} = 4.34\times 10^{17}s = 137.5 \text{ 亿年} \quad (10b)$$

因此，可以这样来理解现在的宇宙 M_{ub} ，即现今 M_{ub} 黑洞球体就是将 n_b 个 $M_{bm} \approx 10^{-5}$ 克的最小黑洞排列成直线为直径所组成的球体。

但是, 原始“宇宙包” M_{ub} 内所有最小黑洞围成一体后, 最小黑洞是一层接着一层的合并所形成的新黑洞是逐渐长大的。因此, 新生的膨胀黑洞的视界半径 R_n 并不能立刻膨胀为原来所有最小黑洞的视界半径之和 Σr_b 。当 $R_n < \Sigma r_b$ 时, 在宇宙包内, 所有因不断合并而长大的新黑洞的视界半径 R_n 只能以光速 C 的速度向外扩张, 如公式(9e), (9g)所示, 而新生黑洞内部的膨胀就只能符合哈勃定律, 即 $V = H_0 R$ 。这就是由诸多原生黑洞合并成新黑洞所造成的内部膨胀, 而新黑洞外面 M_{ub} “宇宙包”的膨胀就是“暴涨”后膨胀的余波。余波每一时刻膨胀的速率取决于其内部同一时间新生黑洞数量的多少, 宇宙初生时新生黑洞最多, 其视界半径都以光速膨胀, 宇宙包的超光速空间膨胀就最大, 后来新生黑洞由于逐渐合并变大而数量减少, 宇宙包的超光速空间膨胀就相应地减小, 直到 $R_n = \Sigma r_b$ 后, 内部新生黑洞成为一体而与宇宙包就合而为一, 如果此时外界没有能量-物质可供吞噬, 宇宙就停止膨胀。这就是宇宙包超光速减速膨胀的根源。

然而, 直到 $R_n = \Sigma r_b$ 的完全膨胀完成后, 如果外面没有能量-物质可供吞噬, 新黑洞的视界半径 R_n 就会停止膨胀, 就会转而向外发射霍金辐射, 即能量粒子, 于是 R_n 开始缩小, 黑洞质量减少, 温度增高, 如此这般一直收缩下去, 直到最后收缩成为两个 $M_{bm} \approx 10^{-5}$ 克的最小黑洞而在爆炸中消亡。^{<10>}

如果现今“宇宙包” M_{ub} 外并无能量-物质可供吞噬, 而尚且膨胀的原因: 按照黑洞原理, 一个孤立而已经完全膨胀的黑洞不会膨胀, 只会因发射霍金辐射而缩小, 所以黑洞只有在吸取外部能量物质或与其它黑洞或星体碰撞时因增加质量才会产生膨胀。因此这里必须分清两种宇宙膨胀的概念, 第一: “宇宙包” M_{ub} 的膨胀是在“原初暴涨”以后, 内部许多小黑洞因合并造成的膨胀所引起的综合空间膨胀的效应, 所以 M_{ub} 的减速膨胀还是超光速的减速膨胀。这种减速是因为内部小黑洞合并后黑洞数目愈来愈少的原因。第二: “宇宙包” M_{ub} 内所有的在某一时刻新合并成的稍大黑洞 M_{bm} 的视界半径 r_b 因临近小黑洞的不断合并但都只能以光速 C 膨胀, 这就是造成 M_{bm} 内以哈勃定律膨胀的原因。必须指出, M_{ub} 内所有的黑洞 M_{bm} 彼此是一层层连接在一起的。因此, 如果现今“宇宙包”外已无能量-物质可吞噬, 而且只有在 $R_n < \Sigma r_b$ 时, 才能造成现今宇宙仍在膨胀, 这就表示 M_{ub} 应该大于现在的 $8.8 \times 10^{55} \text{g}$, M_{ub} 内尚有未被 M_{bm} 吞噬完的剩余的能量-物质, 或者说 n_b 多于现在的 8.8×10^{60} 。

3. 现今宇宙的消亡机理: 不是宇宙的实际密度 ρ_r 而是宇宙现有的总能量物质 (M_{ub}) 决定宇宙今后是否膨胀, M_{ub} 是在宇宙诞生时的原始宇宙包的总能量-物质 M_0 和在宇宙年龄内的膨胀过程中所吞噬的总能量-物质 ΔM_0 之和。即,

$$M_{ub} = M_0 + \Delta M_0 \quad (10c)$$

在上一节里已经证明, 对于一个宇宙黑洞来说, 密度只有 1 个, $\Omega = 1$ 是必然的结果。而根据霍金量子黑洞理论, 黑洞消亡的寿命 τ_b ,

$$\tau_b \approx 10^{-27} M_b^{3<5>} \quad (10d)$$

如果宇宙现有总能量-物质是 $M_{ub} = 8.8 \times 10^{55}$ 克, 而外界再无能量-物质可供吞噬, 则宇宙就会从现在开始发射霍金量子辐射, 直到最后收缩成为一个 $M_{bm} \approx 10^{-5}$ 克的最小黑洞而在爆炸中消亡为止, 如(10d)所示, 我们宇宙寿命会长达 $\tau_{ub} \approx 10^{127}$ 年。

4. 作者对宇宙加速膨胀原因的新解释: 作者不久前论证了, 我们宇宙的加速膨胀是由于在宇宙早期所发生的两大宇宙黑洞间的碰撞所造成的。^{<11>}从上段可知, 即只要宇宙包的总能量物质 M_{ub} 一定, 也就是说, 当(10c)式中的 ΔM_0 在某一定时间成为常数而不再增加时, 或者说, 当在某一定时间而外界再无能量-物质可供吞噬时, 宇宙终究有停止膨胀

的一天. 从停止膨胀的一天起, 宇宙就会开始发射霍金量子辐射而收缩, 直到最后收缩成为两个 $M_{bm} \approx 10^{-5}$ 克的最小黑洞而在爆炸中消亡。但几年前, 即在 1998 年, 由美国加里福里亚大学的劳伦斯伯克莱国家实验室的 Saul Perlmutter 教授和澳大利亚国立大学的 Brian Schmidt 所分别领导的两个小组通过对遥远的 Ia 型超新星爆炸的观测发现了我们宇宙的加速膨胀, 他们指出那些遥远的星系正在加速地离开我们。^[11] 现在, 多数的相关的科学家们认为我们宇宙的加速膨胀是由于宇宙中存在具有排斥力和负能量的神秘的“暗能量”所造成的。特别是, 我们宇宙诞生于 137 亿年前, 那时暗能量并没有随宇宙诞生而出现, 而暗能量却是在大约 90 亿年前才蹦出来以造成我们宇宙的加速膨胀。^[11] 究竟什么是暗能量呢? 现在还无人知道。中国科技大学物理学教授李淼就幽默地说过: “有多少个暗能量的学者, 就能想像出多少种暗能量”^[11] 那么, 我们宇宙的加速膨胀就只能用具有排斥力和负能量的神秘的暗能量来解释吗? 作者在该文“对宇宙加速膨胀的最新解释: 这是由于在宇宙早期所发生的两个宇宙黑洞间的碰撞所造成的。”中论证道, 按照黑洞的原理和其本性, 任何一个黑洞的膨胀完全产生于吞噬外界的能量物质和与其它黑洞的碰撞。在该文中, 对我们宇宙的加速膨胀将用一个宇宙黑洞和另一个宇宙黑洞在其早期的大约 90 亿年前所发生的两个宇宙黑洞的碰撞来解释, 可得到令人相当满意的结果。虽然该文中^{<11>}的论证可能相对地简单, 但比现有的其它各种理论的论证更为合理。^{<11>} 因为。任何对宇宙的加速膨胀解释的理论必须符合我们宇宙的平直性要求和当今较准确的观测值($\Omega = 1.02 \pm 0.02$), 而只有本文的解释才符合此要求。有排斥力的暗能量和所有其它理论都可能成为找不到的幽灵, 因为它们都解释不了我们宇宙的平直性。^{<11>}

5. 对宇宙诞生时大爆炸的理解和宇宙的最后命运: 大量原初宇宙最小黑洞 $M_{bm} \approx 10^{-5}$ 克的合并或碰撞造成了整个宇宙的“原初暴涨”。大量宇宙最小黑洞的同时的合并或碰撞在宇宙各处所产生的冲击爆炸就是现今宇宙婴儿的第一声啼哭, 也就是新宇宙的诞生。这种宇宙各处的“小爆炸”(最小黑洞之间的碰撞)交织成新宇宙诞生的“大爆炸”是在整个原始宇宙包内各处发生的, 而不是像奇点的“大爆炸”一样在一点突发出来的。各个高温粒子最小黑洞 M_{bm} 之间的相互碰撞和融合过程在起初是整个宇宙内的巨烈的冲击爆炸, 当然首轮的爆炸由于所有的 $n_b = 8.8 \times 10^{60}$ 个 M_{bm} 都参与其中而最剧烈, 接下而来的各轮黑洞的合并由于逐轮黑洞的合并使黑洞数量的逐次减少而使爆炸渐次减弱, 直到如下所述的到大约 $t_p = 10^{-15}$ 秒后, 整个宇宙 M_{ub} 内的所有 M_{bm} 就连接而成为一个宇宙包了。而后, M_{ub} 就转变为长久的内部膨胀过程, 这个过程就变成为一个“宇宙包”长期的超光速的减速膨胀过程, 也就是大爆炸后余波的膨胀过程, 当这个过程一直持续到完全膨胀为 $R_{ub} = \Sigma r_b = n_b r_b$ 时, 如果 M_{ub} 外再无能量-物质可供吞噬, 宇宙 M_{ub} 就会开始向外发射霍金量子辐射而同时收缩其 R_{ub} , 如前所述, 这个极其缓慢的收缩过程会持续大约 10^{127} 亿年后, M_{ub} 会再收缩成为两个 $M_{bm} \approx 10^{-5}$ 克的最小黑洞而在爆炸中消亡。

但是, 我们宇宙现在仍然在继续膨胀, 这表明宇宙外面还有大量的能量-物质可供吞噬, 因此, 宇宙总质量 M_{ub} 还在增加, 其视界半径 R_{ub} 还在扩大, 直到未来有一天, 外界所有的能量-物质被吞噬完毕, 这时宇宙的总质量就达到 $M_{ubf} = M_{ub} + \Delta M_{ub}$ 。宇宙的生命将增长成为 $\tau_{ubf} \approx 10^{-27} M_{ubf}^3 \gg 10^{127}$ 亿年。

6. 多宇宙的存在有力证据: 我们宇宙 M_{ub} 的收缩过程是由于持续不断地向外发射霍金量子辐射, 这是一个极其缓慢的过程, 所以它最后只是收缩成为唯两个 $M_{bm} \approx 10^{-5}$ 克的最小黑洞而在爆炸中消亡。这个过程与前辈宇宙的大塌缩的过程是完全不同的。具有多到

无法想象的能量-物质的前辈宇宙的大塌缩绝大的可能是一次极其迅速而猛烈的塌缩。结果我们整个宇宙被塌缩成为在其中一个核子大小的高温小粒子包。如上面(A)段所述,其史瓦西半径只有 $R_0 = 3.45 \times 10^{-13} \text{cm}$ 。可以直觉地想象出前辈大宇宙的大塌缩绝对不可能只塌缩出仅仅一个核子大小的我们的宇宙,更可能同时塌缩出许多个核子宇宙。退一步说,即便只塌缩出一个我们的核子宇宙,在其外面也必定有大量的因为大塌缩爆炸被抛射出去的能量-物质,正如大恒星死亡时在中心塌缩出一个黑洞外,同时向外面抛射出更多的能量-物质一样。^{<11>}

何况,新近的对 Ia 型超新星爆炸的观测表明,我们宇宙的加速膨胀是宇宙诞生大约 50 亿年后才发生的,这表明所谓的“暗能量”或者与其它外面另一个宇宙的碰撞所造成的我们宇宙的加速膨胀并不是随我们这一个宇宙包的诞生而出现,而是在宇宙的诞生后约 50 亿年的半途才出现的;也就是说,我们原始的宇宙包的能量-物质总量 M_{u0} 比现在的 $M_{ub} = 8.8 \times 10^{55}$ 克的总量要少得多。在与另外的宇宙碰撞以前, M_{u0} 既已完全膨胀而停止了膨胀。所以在 90 亿年以前与另外的宇宙碰撞以后,由于我们宇宙从另外一个宇宙中吸收大量的能量物质而造成了现在可观测到的宇宙的加速膨胀。我们宇宙在 90 亿年内增加的总量为 ΔM_{u0} , 即 $M_{u0} + \Delta M_{u0} = M_{ub}$, 而 $M_{u0} < \Delta M_{u0}$, 而且在由于出现了大量的 ΔM_{u0} 造成了宇宙的加速膨胀. 这就清楚地表明 所谓的“暗能量”或者如作者所指出的被我们宇宙所吞噬的其它宇宙的能量-物质不是我们宇宙在诞生时所固有的,而是来自我们宇宙的外界,即外面的宇宙或者外面的宇宙包. 这就是多宇宙存在的强有力的证据。^{<11>}也说明前辈宇宙的大塌缩不只是塌缩出唯一一个我们的宇宙包,还有多个我们所不知道的其它的宇宙包。

7. 我们宇宙黑洞与所有黑洞的同一性: 我们宇宙的生长衰亡过程与每一个黑洞是完全一样的,^{<10>}绝对不是一个循环过程。虽然我们宇宙的诞生来源于前辈宇宙塌缩所产生的 $n_b = M_{ub}/m_b = 8.8 \times 10^{60}$ 个 ($M_{bm} \approx 10^{-5}$ 克) 史瓦西最小黑洞, 当前辈宇宙最后塌缩成为如此大量的 ($M_{bm} \approx 10^{-5}$ 克) 最小黑洞所组成的我们的宇宙包时, 它也许还塌缩出许多其它的由大量的 ($M_{bm} \approx 10^{-5}$ 克) 最小黑洞所组成的另外的诸多宇宙包, 因此, 其塌缩过程应当是一个极其迅速而猛烈的瞬间发生的大量能量-物质的集结和塌缩过程。因此, 各个 ($M_{bm} \approx 10^{-5}$ 克) 最小黑洞爆炸解体在普朗克量子领域后, 又能重新聚集成为稍大的大量最小黑洞而组成了许多新宇宙包, 其中的一个宇宙包就产生出我们的宇宙, 形成了一个现在巨大的宇宙黑洞 (UBH), 其最后的命运是因为极其长久地逐渐发射微量的霍金量子辐射而最后收缩成为两个最小黑洞 ($M_{bm} \approx 10^{-5}$ 克) 而爆炸消亡, 我们宇宙绝不可能最后塌缩出一个小黑洞或者另外一个小宇宙。因为我们宇宙的这个收缩过程是一个极其缓慢的在自由空间进行的过程, 它使宇宙内的所有能量-物质逐次地渐渐地转变为量子后向外发射出去单个的辐射能量量子, 这是一个无序的长期的宇宙熵增加的不可逆过程。这些发射到宇宙中的能量粒子是无法重新聚集起来的。因此, 我们宇宙的这个生长衰亡的过程与每一个黑洞是完全一样的, 都绝对不是一个循环过程。宇宙黑洞 (UBH) 的所有的黑洞本性与一般的黑洞的本性是完全一样的, 也完全遵守一般的黑洞在其视界半径 R 上的守恒公式。^{<10>}只不过我们这个宇宙黑洞 (UBH) 的质量比所有宇宙内部黑洞的质量大得多, 因而其内部更加复杂, 其寿命更加长而已。本文中否定了“宇宙循环论”。因此, 宇宙的产生膨胀演变和收缩衰亡是完全符合黑洞的本性和规律的。我们宇宙从前辈大宇宙的能量-物质聚集的最后大塌缩成为无数 ($M_{bm} \approx 10^{-5}$ 克) 的最小黑洞中诞生, 这整个过程是在封闭的宇宙包内完成的。但是宇宙将来从外界无能量-物质可吞噬而转向发射霍金辐射开始, 直到最

后收缩成为两个($M_{bm} \approx 10^{-5}$ 克) 最小黑洞在爆炸解体消亡, 变成尸骨无存的零散的辐射能量为止, $\langle^{10}\rangle$ 这个过程是在自由空间慢慢完成的一个熵增加的不逆过程。

XI.对宇宙的“原初暴涨 (Original Inflation)”的最新而简明的解释和论证:

从上面可知, 如果我们宇宙现在的总质量 $M_{ub}=8.8 \times 10^{55}$ 克可认为是由 n_b 个 ($n_b = M_{ub}/8.8 \times 10^{60}$) $\approx 10^{-5}$ 克的原生最小黑洞合并后完全膨胀而来, 那么, 宇宙原初暴涨的时间 t_0 就是我们“原始宇宙包”内所有的能量-物质 M_{ub} 为膨胀和合并的所有的

现在来看看 $\approx 10^{-5}$ 克的原生最小黑洞开始时是如何合并的。从(9c)可知 的视界半径即史瓦西半径 $r_b=1.48 \times 10^{-33}$ cm, 假设一个初生的 刚刚开始时与其最临近的 n_{m2} (或者 n_{m3}) 个 合并, 光通过 的视界半径 r_b 的时间 $t_b = r_b/C = 0.5 \times 10^{-43}$ s. 当经过 $2t_b$ 的时间与其周围临近的 n_{m2} 个粒子合并成一个半径为 $2r_b$ 的圆球黑洞时, 则应当有,

$$n_{m2} r_b^3 = (2r_b)^3, \therefore n_{m2} = 8 \quad (11a)$$

(11a)式说明, 当时间成 2 的倍数增加时, (或者视界半径 r_b 成 2 的倍数增加时, 二者的理由和结果是同样的。)所合并成的较大黑洞的原始粒子 的数目将以 8 的指数倍增长。下面将计算到什么时候 t_0 才将所有 $n_b = 8.8 \times 10^{60}$ 个初生的 连接成一个 $M_{ub}=8.8 \times 10^{55}$ 克的原始宇宙包。

$$n_b = 8.8 \times 10^{60} \approx 10^{61} = (8^{67.5}) \quad (11b)$$

(11b)式告诉我们, 当初生的 经过($2^{67.5}$)倍的时间后, 宇宙所有的($8^{67.5}$)个 就连成一个宇宙包了。而

$$(2^{67.5}) \approx (10^{20.3}), \text{ 令 } t_{02} = 10^{20.3} \quad (11c)$$

现在以同样的方式求 $n_{m3}=27$ 时,

$$\text{令 } n_{m3} r_b^3 = (3r_b)^3, \therefore n_{m3} = 27 \quad (11aa)$$

$$n_b = 8.8 \times 10^{60} \approx 10^{61} = (27^{42.6}) \quad (11ba)$$

$$(3^{42.6}) \approx (10^{20.3}), \text{ 令 } t_{03} = 10^{20.3} \quad (11ca)$$

$$\therefore \text{可见, } t_0 = t_{02} = t_{03} \approx (10^{20.3}) \quad (11cb)$$

从(11cb)可知, 无论宇宙 $\approx 10^{-5}$ 克的原生最小黑洞以哪一种方式合并, 将整个宇宙 $M_{ub} = 8.8 \times 10^{55}$ 克的所有 n_b 个 连成一个“原始宇宙包”所需的时间是同样的, 即 $t_0 = t_{02} = t_{03} \approx (10^{20.3})$ 。其实, 无论 以哪一种方式聚集和合并, $t_0 = t_{02} = t_{03} \approx (10^{20.3})$ 是一个必然的普遍规律和结果。现在可令 $n_m = n_b = 8.8 \times 10^{60} \approx 10^{61}$, 于是, $n_m r_b^3 = (n r_b)^3$, 可变成 $10^{61} r_b^3 = (10^{20.3} r_b)^3$ 。

$$\text{现在, 更进一步, 从(11a)式, 令 } n_m = n^3 \quad (11cc)$$

$$\text{则, } n_b = 8.8 \times 10^{60} \approx 10^{61} = n_m^x \quad (11cd)$$

$$x = 61/\lg n_m \quad (11ce)$$

$$\text{令 } n^x = 10^y \quad (11cf)$$

$$y = x \lg n = \lg n \times 61 / \lg n_m = \lg n \times 61 / (3 \times \lg n) = 61 / 3 = 20.3 \quad (11cg)$$

(11cg)式再次表明, 无论以哪一种方式聚合并, 在 $n_b = 10^{61}$ 时, (11cb)中 $t_o = (10^{20.3})$ 是一个普遍规律和结果。但是, 实际上由于在 $t_o = 10^{20.3}$ 秒的时间内, 每个有所膨胀, 其视界半径 r_b 的膨胀量 $= C t_o$, 就使得 t_o 再应当滞后一个 t_o 而成为 $2t_o$ 。因此,

$$2t_o = 2 \times 10^{20.3} = 10^{20.6} \quad (11ch)$$

(11ch)表明经过 $2t_p = 2t_o \times t_b = 10^{20.6} \times 0.4 \times 10^{-45} = 10^{20.6} \times 10^{-45.4}$ 的时间后, 即大约 $2t_p \approx 10^{-25}$ 秒后, 宇宙所有 n_b 个就连接成一个 M_{ub} 的“宇宙包”了, 外界不再有新增加的质量了。而此时宇宙包内每个“长大了的小”的视界半径 $r_b \approx 10^{-25} C = 3 \times 10^{-15}$ cm. 设此时宇宙包 M_{ub} 的半径为 r_p ,

$$\text{按照 } M_{ub} = 4\pi\rho r_p^3 / 3 \text{ 和 } \rho = 3 / (8\pi G t_p^2) = 1.79 \times 10^{56} \text{ g/cm}^3, \quad (11d)$$

$$r_p^3 = 2G t_p^2 M_{ub} = 0.1175 \text{ cm}^3, \quad \therefore r_p \approx 0.5 \text{ cm} \quad (11e)$$

$$r_p / r_b = 0.5 / (3 \times 10^{-15}) \approx 10^{16} \quad (11f)$$

(11f)式说明宇宙包 M_{ub} 的尺寸即半径为 r_p 在 $t_p = 10^{-25}$ 秒时, 比当时的视界半径 r_b 暴涨了 10^{16} 倍。而体积则暴涨了 10^{48} 倍。

下面说明宇宙“暴涨”之后, 即在 $t_p = 10^{-25}$ 秒后, 宇宙是如何膨胀的。由于此时小宇宙的视界半径 $r_b \approx 3 \times 10^{-15}$ cm, 相应地, 长大了小宇宙 $= r_s C^2 / 2G = 2.02 \times 10^{13}$ g. 而寿命 $\tau_m \approx 10^{-27} m_b^3 = 8.24 \times 10^{12}$ s. 这就是说, 在当时以 $r_p \approx 0.5$ cm 为半径的 M_{ub} 宇宙包内, 包含有 $n_s = M_{ub} / = 8.8 \times 10^{55} / 2.02 \times 10^{13} = 4.4 \times 10^{42}$ 个相互连着的 $= 2.02 \times 10^{13}$ g 小黑洞。而每个的寿命都已如此之长久, 同时宇宙包密度 $= 10^{56}$ g/cm³ 又如此之高, 它们都不可能再因为发射极少量的霍金辐射而收缩, 只能跟相邻的之间再合并而膨胀了。另一方面, 在当时的宇宙包内, 不可能存在着比 $= 2.02 \times 10^{13}$ g 更大的黑洞, 因为更大的黑洞需要比 $2t_p \approx 10^{-25}$ 更长的时间才能形成。但由于宇宙包内可能存在的极小极小的温度差和密度差, 因此, 可能产生比黑洞相差极小极小的黑洞。但是, 无论如何, 所有相邻的小黑洞之间都只能再合并而膨胀了。根据公式(11c)可知, 各个相邻的小黑洞之间的合并而只能造成其视界半径以光速 C 膨胀, 并且都有相同的时间 t_p 和相同密度 ρ , 因此, 它们内部的膨胀规律都合乎哈勃定律 (9f), (9g) (9h)。这就是哈勃定律所描述的宇宙膨胀规律和宇宙黑洞的膨胀规律的一致性的根源。从(9g)式, $M_b = C^3 t_u / 2G = C^2 R_u / 2G$ 可知, 当宇宙由小黑洞从 $t_p = 10^{-25}$ 秒膨胀到 $t_p \Rightarrow$ 现今的 $t_u = 137$ 亿年宇宙年龄时, $\Rightarrow M_{ub} = 8.8 \times 10^{55}$ 克而成为现今宇宙的总质量。其实, 宇宙由小黑洞与原始宇宙包 M_{ub} 的关系也可以简单地看成为在的外面有一个 M_{ub} 那样大的一个能量-物质包, 能长期而充足地供给能量-物质为所吞噬, 使宇宙包 M_{ub} 内的的视界半径 r_b 都能够长期的以光速膨胀, 直到经过宇宙年龄 t_u 之后, r_b 就扩张到与现在的 R_u 相重合, 而宇宙包 M_{ub} 就增长到 $M_{ub} = 8.8 \times 10^{55}$ 克而成为现今宇宙的总质量。

从上面的描述可以得出如下的一下结论。

1. 是 M_{ub} 的 n_m 个中的一个, 的视界半径 r_p 因与其它 的合并或者吞噬 M_{ub} 中的足够多的能量-物质, 使 的视界半径 r_p 以光速 C 的速度扩张, 而宇宙包 M_{ub} 是以超光

速C作减速的空间扩张，以保持与其内部所有的 有同等的密度，这就是宇宙暴涨后的膨胀余波。这样的膨胀一直持续到现在，最后使得 长大到 等于现在的 M_{ub} ，而使二者的视界半径现在相重合。

2. 如果现今宇宙 M_{ub} 外空空如也，再无任何一丁点能量-物质可被吞噬，我们宇宙就会停止膨胀，转而开始向外发射霍金辐射而收缩其视界半径 R_u ，宇宙的命运就如上面 X 节(E)段中所述一样。 M_{ub} 的寿命 $\approx 10^{127}$ 亿年。

3. 但实际上，正如上面(D)，(F)段所示，我们宇宙在约 90 亿年前与另外一个宇宙包发生碰撞而产生了加速膨胀，因此我们宇宙在诞生时的“原始宇宙包” M_{uo} 就不是现在的 $M_{ub} = 8.8 \times 10^{55}$ 克，而是比 M_{ub} 要小的 M_{uo} 。

$$\text{因此, } M_{uo} = M_{ub} \times (137 \text{ 亿年} - 90 \text{ 亿年}) / 137 \text{ 亿年} = 0.343 M_{ub} = 3 \times 10^{55} \text{ 克}^{<11>} \quad (11g)$$

这样，我们宇宙的膨胀模式就应当有所修改，即我们宇宙在从诞生时起到 90 亿年前为止，原始宇宙包 M_{uo} 就在“原初暴涨”后开始减速膨胀，直到从 90 亿年前为止达到完全膨胀后停止了膨胀。稍后在与“另外一个宇宙包”碰撞后，因为能够从其中吞噬足够多的能量-物质，而使宇宙包 M_{uo} 的视界半径 R_{uo} 又重新以光速 C 膨胀而直到今天，使 M_{uo} 长大而达到等于 $M_{ub} = 8.8 \times 10^{55}$ 克。这就使我们观测到 90 亿年前我们宇宙的加速膨胀，即先有 M_{uo} 的停止膨胀，而后又以光速膨胀。当然也有可能 $M_{uo} < 3 \times 10^{55}$ 克，比如说， M_{uo} 不是早在 90 亿年以前而是在 100 亿年以前已经完全膨胀，而是经过 10 亿年以后才再与另外一个更大的宇宙大黑洞发生碰撞，那么，这个更小的原始宇宙包 M_{uo2} 为，

$$M_{uo2} = M_{ub} \times (137 \text{ 亿年} - 100 \text{ 亿年}) / 137 \text{ 亿年} = 2.383 \times 10^{55} \text{ 克} \quad (11h)$$

从以上的分析可见，如果我们的“原始宇宙包”不是 M_{ub} ，而是 M_{uo} 或者是 M_{uo2} ，那么， $t_0 \approx (10^{20.3})$ 也就不对了，就会变成 $t_0 < (10^{20.3})$ 。这就是说，上面的 $t_p \approx 10^{25}$ 也不对，也会随着变小，比如说， t_p 会变成 $t_p \approx 10^{36}$ 秒等。

XII. 进一步的说明：从本文前面所得出的新观点和最新论证就可以得出如下结论：

1. “奇点”被定义成为具有某些无限大物理量(密度)的点。广义相对论导致我们现在膨胀的宇宙必然地从奇点诞生出来，也导致黑洞的中心必然有奇点存在。这是广义相对论不可避免的结果和无法解决的问题。奇点问题已困扰科学家们五十年以上，^{<7>}它也是天文学与科学中最复杂而困难的问题。至今尚无一种单独理论既能从其数学方程中消除奇点又能建立出一幅完满自洽的图象。困扰在于：数学方程的变化是连续的，而物理状态之间的转变点为突变(相变)而有临界点，因此，用一种理论及其具有连续性的方程去统一地描述相连接的多种物理结构的运动状态及其临界点的变化是非常困难的。因为自然界找不到“奇点”，所以自然界必然存在着能阻止奇点产生的机制或规律。例如，由于原子内的电子必须遵从量子力学的测不准原理，电子不会陷落到原子核内而塌陷为奇点。

2. 由于在自然界找不到奇点的存在。奇点的产生必然会违反自然界的因果律和热力学第二定律。也违反能量守恒定律，上帝决不会派发“免费午餐”。所以，从逻辑思维或物理推理上否定奇点的存在并不是新观念或新想法，也不是为怪。“奇点”只隐藏在数学方程的极端，但要从中消除它们却绝非易事。当人们问物理学家费恩曼(R.P.Feynman)为什么获诺贝尔奖

时,他诙谐地答道:“我只不过是把无穷大藏了起来。”本文的出发点就在于尝试以直接简易的新方式方法论证自然界(包括宇宙诞生时刻和黑洞内部)不存在有无穷大物理量的奇点.因为在宇宙内部,任何物体的状态在达到无穷大量之前就一定会达到某个临界点而后“相变”以改变形态从而避免奇点的出现.宇宙和黑洞本身也不例外.

3. 只要方程式中的粒子用质点,点电荷或波包等点结构来表示,收缩到最后必然会出现奇点.因为在所有理论的数学方程中,如果允许质点或电荷收缩集中到无穷小的一个点上,该点必然具有无穷大的质量或电荷密度.因此,单独的广义相对论或单独的量子力学等经典理论都不能消除奇点.量子电动力学(QED),量子色动力学(QCD)与对称理论等都只能靠重正化来消除奇点.只有弦论中的弦和膜论中的膜不是点结构,所以必然在其数学式中无奇点.但弦论并不成熟,即使将来恐也无法观测到细微的弦的踪迹.从理论上讲,不同维数的弦论有许多种,究竟那一种是正确的?因此,用弦论和其它的各种新理论去消除奇点,只是高超的数学游戏,距离现实还很遥远.它们都远非完善,如超弦理论,量子引力论,多维理论或 $N=8$ 超对称理论,或终极理论(ToE, Theory Of Everything)等等.

4. 在本文中,没有用一种单独的统一的新理论及其新的数学方程,所以无需从任何数学方程中消除奇点.作者只不过是在综合运用现有的多种(而非单独一种)经典理论的原理和相对应的许多基本公式并通过计算,从物理机制上确定宇宙和黑洞的最后收缩必然发生“相变”而达到 Planck 领域,不会从 Planck 领域继续塌缩而产生“奇点”.在论证中,通过计算求出宇宙诞生时和黑洞内部的真实的宏观物质结构和宏观物理状态及其“相变”过程,而不需要用深奥的新理论和高深复杂的数学方程去解决小于 Planck 标度(即 $d \leq 10^{-33}$ cm, 时间 $t \leq 10^{-43}$ s)时的微观物质结构的不可知问题.正如我们可以用贝努利方程去研究流体力学与气体力学而无须知道氢氧的原子是由夸克组成的一样.这种直接简易的思维或许变成了解决一些复杂艰难问题的捷径.对许多悬疑未决的重大科学问题可能作出独创性的解释或解答,从而得出了文中许多全新的可信的结论.例如, (a). 本文中的最重要的新公式(3c), $t^{3/2} \leq k_1(2G\kappa)/(C^5)$ 准确地计算出在 $t \approx -0.5563 \times 10^{-43}$ s 时, 前辈宇宙在该点失去引力而停止收缩的时间范围. (b). 宇宙诞生前后演变的大致路线图. (c). 宇宙黑洞和所有黑洞的同一性: $\langle 10 \rangle$ 宇宙诞生于最小黑洞($M_{bm} \approx 10^{-5}$ 克), 它现在却是一个巨无霸的宇宙黑洞(UBH), 最后的命运也还是收缩到最小黑洞($M_{bm} \approx 10^{-5}$ 克)而爆炸消亡, 宇宙的膨胀演变和收缩完全符合黑洞的本性和规律. $\langle 10 \rangle$ (d.) 宇宙的“原初暴涨”起因于上述最小黑洞的碰撞与合并. (e), 今后宇宙的演变和消亡过程.(f.) 宇宙今后是否膨胀不取决于宇宙的真实密度 ρ_r , 而取决于我们这个“宇宙包”的能量-物质的总量 M_{ub} . 宇宙真实密度 $\rho_r = \rho_c$ 或 $\Omega = 1$ 是宇宙作为黑洞的本性所决定的必然结果. 上述这许多新的论点和结论超乎寻常而发人深省.

5. 本文虽未创建新理论或创立新方程,但在解答现今存在的科学难题上却似乎胜过其它的任何一种单独的经典理论或新理论. 由于所运用的各种经典理论的基本公式基础坚实, 在自然界行之有效, 故文中对宇宙学提出的所有新观念新论证新解释和新结论有比较圆满的自洽性, 与现今的观测数据完全相符合. 本文也不排斥任何新理论的现有成果和结论.

6. 单独的广义相对论不适合于描述宇宙诞生时在普朗克时期(Planck Era), 即 (-10^{-43} s $\leq t \leq +10^{-43}$ s) 中所发生的“相变”转变过程, 正如牛顿力学不适合于描述物体接近于光速时的运动一样. 每种理论及其数学方程都有其应用极限, 广义相对论也不例外. 如上面所证明, 当前辈宇宙大塌缩成为 $\approx 1.125 \times 10^{-5}$ 克的最小黑洞时, 就进入到普朗克时空领域, 即进入到了 $l_p = 1.61 \times 10^{-33}$ cm 普朗克尺度上, 或者说, 在 $t_p = 0.539 \times 10^{-43}$ s 普朗克领域, 在这个领域, 时空是不连续的, 或者说时空是量子化的, 广义相对论的方

程已经达到极端而不适用于普朗克尺度的这种不连续时空结构的层次，在这个结构的层次，只适用量子力学中的测不准原理。而由广义相对论中的极端导出来的想象中的“奇点”的尺度应该比 l_p 还要小得更小得多，因此广义相对论就更不能适用了。广义相对论的方程是一种大尺度的均匀连续的变化方程，这就注定了广义相对论将宇宙诞生解释为从“奇点”或者“奇点的大爆炸”是说不通的，是违反现在宇宙中的许多根本规律的，如能量守恒定律，因果律，热力学定律等等。因此，那种坚持将广义相对论的极端出现“奇点”的观念生硬地用于真实的物理世界的学者们是非理性的，是在故意用高超的数学游戏来误导人们。

实际上，约翰·格里宾在其“大宇宙百科全书”的 Planck Era 有关的章节中也已提出：“我们宇宙可能就是从这样一个粒子 $\approx 10^{-5}g$ 起源的”。^{<8>}“（普朗克时代）实际上就是宇宙创生时所处的状态”。^{<8>}作者在本文中只不过比较确凿地用计算出来的真实数据证实了约翰·格里宾的猜想而已。

7. 如果本文排除了宇宙诞生于“奇点”或者“奇点的大爆炸”，那就没有必要在宇宙创生时给予任何特殊的边界条件，也不必乞灵于上帝或奇迹或新物理学如量子引力论，弦论或超对称理论等对我们宇宙起源或对“宇宙大爆炸”的诸多牵强附会的解释。根据现成的经典理论就能阐明和推算出我们宇宙诞生时的演变机理，条件和过程，这种演变过程完全符合现有的物质世界的规律和物理定律，如因果律，质能转变守恒定律等。

8. 困扰科学家几十年的宇宙创生时的四大疑难（奇点疑难，平直性疑难，磁单极疑难和视界疑难），在本文否定了“奇点”的存在以后，其它的三大疑难就会迎刃而解了。其实，本文上面已经基本解决了“平直性疑难”和“视界疑难”问题。

9. 当宇宙中任何物体的结构处于“相变”的临界状态时，物体将通过相变从一结构的层次转向另一结构层次，在同一结构内，较适用于用统一的简明公式去解决其运动和变化的量变问题，而想用用一个完整的单一理论及其统一的公式去解决物质所有不同结构层次的数量变和相邻结构层次之间的相变中的问题是极其复杂和困难的，因为各个结构层次中都有不同的诸多的尚不知道的边界条件而极难解出一个或者一组统一的方程。这就是本文用几个简单的经典公式与观测数据相对照而能推算出许多正确结论的根本原因。

10. 本文计算中所得出的数据与现有理论，公式和观测结果是相当一致的。这表示本文中**新观念是宇宙的实际演化规律的一幅较好的自洽图像**。或许本文中的新观念和论证方法由于缺乏深奥的新理论，复杂的数学方程和违反常规而难于为绝大多数科学家所接受和信服。但本文由于所用的理论和公式却是**可靠而有效的，所以其独特而简单的证明方式和所计算的结果是符合宇宙演变中各种现有的规律的**。这为运用几个简单而可靠的经典基本公式以解决复杂的科学难题提供了一个实例。爱因斯坦曾警告说：“万事万物应该尽量简单，而不是更简单。”本文中简单的新观念和新的论证方法也可以作为一种抛砖引玉吧。

====全文完====

参考文献:

1. Michael D. Lemonick: How The Universe Will End, TIME, June 25. 2001.
2. Giancoli, Douglas. Physics, Principles With Application, 5th Edition, Upper Saddle River, NJ. Prentice Hall, 1998,
3. 苏宜：“天文学新概论”，华中理工大学出版社，2000.
4. Wienberg, Steven: “最初三分钟”。中文版，外文翻译出版社，中国北京 1999,

5. 王永久: “黑洞物理学”, 湖南师范大学出版社, 2000.
6. 何香涛: “观测宇宙学” 科学出版社, 2002 年
7. 丹尼斯. 奥弗比: “环宇孤心” 北京中信出版社, 2002 年
8. : 约翰. 格里宾: “大宇宙百科全书”。海南出版社, (中文版), 2001. 9。
9. 王义超: 暗能量的幽灵. 中国 <财经> 杂志, 总 176 期, 2007-01-08.
<http://www.caijing.com.cn/newcn/econout/other/2007-01-06/15365.shtml>
NASA • Webmaster: Britt Griswold • NASA Official: Dr. Gary F. Hinshaw • Page Updated: Tuesday, 04-29-2008. http://map.gsfc.nasa.gov/universe/uni_age.html
10. 张洞生: <http://www.sciencepub.net/newyork/0102>
11. 张洞生: 对宇宙加速膨胀的最新解释: 这是由于在宇宙早期所发生的宇宙黑洞间的碰撞所造成的
<http://www.sciencepub.net/academia/0101> 和 <http://www.sciencepub.net/newyork/0102>.
12. 卢昌海: 宇宙常数, 超对称和膜宇宙论. <http://www.changhai.org/2003-08-17>.

Our Universe Was Originated From The Big Bang Caused By The Amalgamations of a Great Amount of the Original Minimum Schwarzschild Black Holes, But Not From Singularity or Not From The Big Bang of Singularity

Dongsheng Zhang
17 Pontiac Road, West Hartford, CT 06117-2129, U.S.A.
ZhangDS12@hotmail.com

Abstract: In this article, According to the principle of the time mirror reversion or the time symmetry, based on some general laws of astronomy, physics and many classical theories, the calculated results could prove that our Pre-universe in its last great collapse had a Big Crunch and then started to turn into the Big Bing which was caused by the amalgamations of a great amount of the original minimum Schwarzschild black holes (MSBH, $M_{\text{bm}} \approx 10^{-5}g$). Therefore, Our present expanding Universe was impossible to be born from Singularity or from the Big Bang of Singularity but from the Big Crunch of Pre-universe. [New York Science Journal. 2009;2(3):78-99]. (ISSN: 1554-0200).

Keywords: Universe; Big Bang; Black Holes; Singularity

New York Science Journal

纽约科学杂志

ISSN 1554-0200

The international academic journal, “New York Science Journal” (ISSN: 1554-0200), is registered in the New York of the United States, and invites you to publish your papers.

Any valuable papers that describe natural phenomena and existence or any reports that convey scientific research and pursuit are welcome, including both natural and social sciences. Papers submitted could be reviews, objective descriptions, research reports, opinions/debates, news, letters, and other types of writings that are nature and science related. Manuscripts submitted will be peer-reviewed and the valuable papers will be considered for the publication after the peer review. There is no charge for the manuscript submissions.

If the authors (or others) need hard copy of the journal, it will be charged for US\$80/issue to cover the printing and mailing fee.

Here is a new avenue to publish your outstanding reports and ideas. Please also help spread this to your colleagues and friends and invite them to contribute papers to the journal. Let's work together to disseminate our research results and our opinions.

Papers in all fields are welcome, including articles of natural science and social science.

Please send your manuscript to: sciencepub@gmail.com

For more information, please visit:

<http://www.sciencepub.net>

<http://www.sciencepub.org>

<http://www.sciencepub.net/newyork>

<http://www.sciencepub.org/newyork>

New York Science Journal

525 Rockaway PKWY, #B44, Brooklyn, NY 11212, The United States,

Telephone: 347-321-7172

Email: sciencepub@gmail.com

Website: <http://www.sciencepub.net/newyork>

New York Science Journal

纽约科学杂志

ISSN 1554-0200

Volume 2 - Number 3 (Cumulated No. 7), March 1, 2009

Marsland Press

Brooklyn, New York, the United States

<http://www.sciencepub.net>

<http://www.sciencepub.org>

sciencepub@gmail.com

ISSN 1554-0200



9 771554 020073